

**University of Alberta**

**Mixed-Valence First-Row Metal Clusters for Catalytic  
Hydrodesulfurization and Hydrodeoxygenation**

by

**Houston John Stinson Brown**

A thesis submitted to the Faculty of Graduate Studies and Research  
in partial fulfillment of the requirements for the degree of

**Doctor of Philosophy**

**Department of Chemistry**

©Houston John Stinson Brown

Fall 2013  
Edmonton, Alberta

Permission is hereby granted to the University of Alberta Libraries to reproduce single copies of this thesis and to lend or sell such copies for private, scholarly or scientific research purposes only. Where the thesis is converted to, or otherwise made available in digital form, the University of Alberta will advise potential users of the thesis of these terms.

The author reserves all other publication and other rights in association with the copyright in the thesis and, except as herein before provided, neither the thesis nor any substantial portion thereof may be printed or otherwise reproduced in any material form whatsoever without the author's prior written permission.

## Abstract

Salt metathesis between  $\text{CoCl}_2$  and  $[\text{KNPEt}_3]_n$  provides a new route to the halide-substituted cobalt phosphoranimide cluster  $[\text{CoCl}(\text{NPEt}_3)]_4$ . This cluster is a useful precursor for the preparation of alkyl-capped cobalt phosphoranimide complexes. The methylated heterocubane  $[\text{CoMe}(\text{NPEt}_3)]_4$  was synthesized in high yield by transmetallation of  $[\text{CoCl}(\text{NPEt}_3)]_4$  with  $\text{Me}_2\text{Mg}\cdot\text{dioxane}$  in dioxane. The structural, magnetic, and electrochemical properties of the cluster have been rigorously evaluated. The type (III) mixed-valence cluster  $[\text{CoMe}(\text{NPEt}_3)]_4\text{PF}_6$  was prepared from  $[\text{CoMe}(\text{NPEt}_3)]_4$  by outer-sphere electron transfer with  $\text{Cp}_2\text{FePF}_6$ . The cationic cluster has been fully characterized. Both  $[\text{CoMe}(\text{NPEt}_3)]_4$  and  $[\text{CoMe}(\text{NPEt}_3)]_4\text{PF}_6$  are active precatalysts for reductive C–S bond cleavage. The catalytic activity of  $[\text{CoMe}(\text{NPEt}_3)]_4\text{PF}_6$  has been investigated in more detail. Under basic conditions, the mixed-valence cluster catalyzes the complete hydrodesulfurization of a number of organosulfur compounds under mild conditions (110–170°C, 1 atm  $\text{H}_2$ ): dibenzothiophene, 4,6-diethyldibenzothiophene, benzothiophene, 3-hexylthiophene, diphenyl sulfide, benzyl phenyl sulfide, and phenoxathiin. In all instances no products indicative of aromatic ring hydrogenation were noted. The desulfurization of dibenzothiophene was investigated over a range of temperatures. A preliminary mechanistic ‘road map’ for the reaction was proposed. The mixed valence cluster  $[\text{CoMe}(\text{NPEt}_3)]_4\text{PF}_6$  also catalyzes C–O bond hydrogenolysis of unstrained ethers. Aromatic, benzyl, and aliphatic C–O bonds are all cleaved under mild conditions. The substrate scope includes diphenyl ether, 4-methoxybiphenyl, 2,3-

dihydrobenzofuran, 1,3-bis(4-methoxyphenoxy)benzene, dibenzofuran, and benzofuran. In no case were products indicative of aromatic ring hydrogenation noted. Catalytic hydrogenolysis in the presence of the Lewis acid  $\text{AlMe}_3$  results in higher turnover frequencies than those not including  $\text{AlMe}_3$ . The presence of the Lewis acid also promoted further C–O bond reductions to give complete hydrodeoxygenation of resistant substrates.

***Preface. A design scheme for tailor-made reductive catalysts: Sterically and electronically tuneable discrete first-row metal clusters***

Last year, the journal *Organometallics* featured a roundtable discussion among seventeen experts in the field of organotransition metal chemistry and catalysis.<sup>1</sup> When asked to describe their ‘wish-lists’ and to foreshadow advancement in the state-of-the-art, the participants focused on a handful of interconnected themes: first row metal systems with ‘precious metal-like’ reactivity, systems that bridge the gap between homogeneous and heterogeneous catalysis, and systems that can be modulated to promote desirable catalytic activity. These themes are embodied in the seminal advances made during this thesis research: the identification of a discrete ligand-supported first row metal cluster, electronically tuned for facile activation and high activity in energetically-demanding reductive catalysis applications.

Second and third row transition metals are most frequently associated with high reactivity, but their high cost, toxicity and scarcity raise barriers to their use in economically and environmentally sustainable large-scale industrial processes. First row transition metals, which are cheaper, broadly abundant, and often less toxic, can become useful candidates for catalysis, provided an appropriate coordination environment can be identified and exploited. The catalysts discussed herein are designed around this concept. Assembling first-row transition metals into discrete ligand-supported clusters induces reactivity uncharacteristic of monomeric first row metal complexes and traditional cluster catalysts; the

presence of multiple electronically-interacting coordinatively unsaturated metal sites absolves any single metal of the burden of mediating the full suite of transformations necessary for catalytic function.

Discrete ligand supported cluster catalysts also bridge the gap between heterogeneous and homogeneous catalysis. Reductive catalytic processes typically employ extended (bulk or nanoscale) solids comprised almost entirely of catalytically inactive, coordinatively saturated, and physically inaccessible metal centres; the catalytically active metals are typically limited to a few highly unsaturated ‘corner’ or defect sites at surface incongruences. The molecular clusters discussed herein feature a heterocubane structural motif: *every* metal occupies a true corner site and *every* metal functions as part of a cooperative metal-nitride-like array. There is no bulk phase. Instead, the metals are supported by robust inorganic scaffolds that facilitate efficient metal-metal electronic interactions and, gratifyingly, precious-metal-like reactivity.

The catalysts discussed herein also demonstrate conclusively how clusters can be electronically modulated to promote optimal catalytic activity. Efficient intra-cluster electronic communication ensures that electronic manipulation of any one metal centre impacts all of the metals in the cluster. Removing a single electron from the homovalent cluster yields only fractional changes to the *cluster* oxidation state: a mechanism for precise electronic control untenable in realm of monometallic catalysis.

## Acknowledgments

I would like to express my deepest appreciation to my supervisor, Professor Jeffrey M. Stryker, who offered me a challenging project then guided me through it with wisdom and enthusiasm. It is a privilege to have him as a mentor; without his persistent help this dissertation would not have been possible.

In addition, I would like to thank the members of the Stryker Research Group (past and present) for their help, advice, and friendship: especially Dr. Robin Hamilton, Dr. Jeremy Gauthier, Dominique Hebert, Jeffrey Bunquin, Devin Reaugh, and Kirsten Tomlin.

I would also like to acknowledge the chemistry support staff who are integral to research conducted in the department. In particular, a big thank you to Dr. Mike Ferguson, Dr. Bob McDonald, and Wayne Moffat.

Thank you John Brown, Jane Brown, and Carina Van Olm Brown and Alex Brown for your love, support, and encouragement.

Most of all I want to thank my loving wife, Jenn Glover, who embodies Abraham Lincoln's words: "In the end, it's not the years in your life that count. It's the life in your years." I am a lucky man!

## Table of Contents

Preface: A design scheme for tailor-made reductive catalysts: Sterically and electronically tunable discrete first-row metal clusters	
1. Ligands and precursors: Iminophosphoranes and transition metal phosphoranimide clusters	1
1.1 Introduction and background	1
1.1.1 Structure and bonding in the phosphoranimide ligand	1
1.1.2 Methods of synthesis of the phosphoranimide ligand	4
1.1.3 Structure and bonding in transition metal phosphoranimide complexes	7
1.1.4 Synthesis of halide-substituted late metal phosphoranimide clusters by high temperature fluoro-desilylation and low temperature salt metathesis	11
1.2 Results and discussion	13
1.2.1 Synthesis of $[\text{CoCl}(\text{NPEt}_3)]_4$ by low temperature salt metathesis	13
1.2.2 Synthesis of related halide-substituted late metal phosphoranimide clusters by low temperature salt metathesis	15
1.2.3 Homoleptic bis(phosphoranimide) cobalt(II) complexes: $[\text{Co}(\text{NPEt}_3)_2]_4$ and related clusters	16
2. Alkyl and alkynyl capped phosphoranimido-metal complexes by transmetallation	22
2.1 Acetylide-substituted late metal phosphoranimide clusters	22
2.1.1 Catalytic alkyne hydrogenation using $[\text{FeCCPh}(\text{NPEt}_3)]_4$	27
2.2 Alkyl-capped cobalt phosphoranimide precatalyst complexes	28
2.2.1 Synthesis and characterization of $[\text{CoMe}(\text{NPEt}_3)]_4$	28
2.2.2 Magnetic and electrochemical studies on $[\text{CoMe}(\text{NPEt}_3)]_4$	35
2.3 Mixed-valence alkyl-capped metal phosphoranimide complexes	43

2.4	The benefits of mixed-valency: Differences between [CoMe(NPEt <sub>3</sub> ) <sub>4</sub> ] and [CoMe(NPEt <sub>3</sub> ) <sub>4</sub> ]PF <sub>6</sub>	47
2.4.1	Electron counting and EAN	48
2.4.2	Reactivity towards dihydrogen	53
2.4.3	Precatalyst activation mechanism(s)	52
2.4.4	[CoMe(NPEt <sub>3</sub> ) <sub>4</sub> ] and [CoMe(NPEt <sub>3</sub> ) <sub>4</sub> ]PF <sub>6</sub> as precatalysts for hydrodesulfurization	61
3.	Mixed-valence cluster catalysts for hydrodesulfurization	63
3.1	Introduction and background	63
3.1.1	Hydrodesulfurization with heterogeneous catalysts	63
3.1.2	Homogeneous hydrodesulfurization chemistry	65
3.2	Results and discussion	77
3.2.1	Catalytic desulfurization of dibenzothiophene by [CoMe(NPEt <sub>3</sub> ) <sub>4</sub> ]PF <sub>6</sub>	78
3.2.1.1	Control experiments	80
3.2.1.2	Mechanistic insights: Catalytic desulfurization of dibenzothiophene by [CoMe(NPEt <sub>3</sub> ) <sub>4</sub> ]PF <sub>6</sub>	83
3.2.1.3	Evaluating the catalytic activity of [CoMe(NPEt <sub>3</sub> ) <sub>4</sub> ]PF <sub>6</sub> at different temperatures	96
3.2.1.4	The role of scavengers in the catalytic desulfurization of dibenzothiophene by [CoMe(NPEt <sub>3</sub> ) <sub>4</sub> ]PF <sub>6</sub>	98
3.2.2	Substrate scope for catalytic desulfurization by [CoMe(NPEt <sub>3</sub> ) <sub>4</sub> ]PF <sub>6</sub>	102
3.2.2.1	Ultra deep HDS: 4,6-Dibenzothiophene	102
3.2.2.2	HDS of benzothiophene	104
3.2.2.3	3-Hexylthiophene	105
3.2.2.4	HDS of diphenyl sulfide	106
3.2.2.5	HDS of benzyl phenyl sulfide	107

3.2.2.6 C–O and C–S bond hydrogenolysis in phenoxathiin	108
3.3 Conclusions	109
4. Towards efficient catalysts for lignin valorization: Mixed-valence cluster catalysts for C–O bond hydrogenolysis	112
4.1 Introduction and background	112
4.1.1 Lignin valorization	112
4.1.2 C–O bond hydrogenolysis in homogeneous systems	116
4.2 Results and discussion	125
4.2.1 C–O bond hydrogenolysis of lignin model compounds	125
4.2.1.1 diphenyl ether	126
4.2.1.2 4-methoxybiphenyl	129
4.2.1.3 2,3-dihydrobenzofuran	131
4.2.1.4 1,3-bis(4-methoxyphenoxy)benzene	132
4.2.2 C–X bond hydrogenolysis related to crude oil processing	133
4.2.2.1 dibenzofuran	134
4.2.2.2 benzofuran	135
4.2.2.3 N-methylcarbazole	136
4.3 Conclusions and future work	138
5. General conclusions and future work	140
6. Experimental section	145
6.1 General procedures	147
6.2 Method for determining mass susceptibility	147
6.3 Instrumentation	148
6.4 Chemical materials	149
6.5 Synthetic procedures	150

6.6 Catalytic procedures	157
Bibliography	175
Appendix 1 Crystallography Data	185

## List of Tables

Chapter 1		
	Table 1.1: Key bond lengths and bond angles for the bis(phosphoranimido)cobalt(II) cluster $[\text{Co}(\text{NPEt}_3)_2]_4$	18
Chapter 2		
	Table 2.1: Selected bond lengths and bond angles for $[\text{Fe}(\text{CCPh})(\text{NPEt}_3)]_4$	27
	Table 2.2: Principle IR and FIR absorbances and assignments for $[\text{CoMe}(\text{NPEt}_3)]_4$	32
	Table 2.3: Selected bond lengths and bond angles for $[\text{CoMe}(\text{NPEt}_3)]_4$	34
	Table 2.4: Redox potentials for the three redox events observed for $[\text{CoMe}(\text{NPEt}_3)]_4$ in difluorobenzene and tetrahydrofuran	40
	Table 2.5: Principle IR and FIR absorbances and assignments for $[\text{CoMe}(\text{NPEt}_3)]_4\text{PF}_6$	45
	Table 2.6: Selected bond lengths and bond angles for $[\text{CoMe}(\text{NPEt}_3)]_4\text{PF}_6$	47
	Table 2.7: Catalytic hydrodesulfurization of dibenzothiophene by $[\text{CoMe}(\text{NPEt}_3)]_4$ and $[\text{CoMe}(\text{NPEt}_3)]_4\text{PF}_6$	62
Chapter 3		
	Table 3.1: Differentiating heterogeneous and homogeneous processes in the catalytic desulfurization of dibenzothiophene by $[\text{CoMe}(\text{NPEt}_3)]_4\text{PF}_6$	81
	Table 3.2: Preliminary evaluations of the relationship between rate of catalytic desulfurization of dibenzothiophene by $[\text{CoMe}(\text{NPEt}_3)]_4\text{PF}_6$ and reaction temperature	97
	Table 3.3: Alternative scavengers for the catalytic desulfurization of dibenzothiophene	100
	Table 3.4: Summary of catalytic hydrodesulfurization of organosulfur moieties common in crude petroleum feedstocks by $[\text{CoMe}(\text{NPEt}_3)]_4\text{PF}_6$	111

## List of Figures

### Chapter 1

- Figure 1.1: Lewis resonance structures for the phosphoranimide ligand 2
- Figure 1.2: Isolobal relationship between cyclopentadienyl- and phosphoranimido-ligands 2
- Figure 1.3: Cone angles and key bond distances for a series of cyclopentadienyl phosphoranimido-titanium halide complexes 3
- Figure 1.4: Phosphoranimide bonding modes A and B with representative examples 9
- Figure 1.5: Phosphoranimide bonding modes C and D with representative examples 10
- Figure 1.6: Phosphoranimide bonding mode E and a representative example 11
- Figure 1.7: 'Melt-preparation' of halide substituted late metal phosphoranimide clusters 12
- Figure 1.8: Dimeric halide-substituted late metal phosphoranimide complexes with bulky-alkyl substituents at phosphorus. 16
- Figure 1.9: ORTEP diagram of the homoleptic bis(phosphoranimide)  $[\text{Co}(\text{NPEt}_3)_2]_4$  18
- Figure 1.10: Key bond lengths and bond angles in  $[\text{Co}(\text{N}(\text{TMS})_2)_2]_2$  20
- Figure 1.11: Homoleptic cobalt(II) phosphoranimide clusters synthesized and characterized in the Stryker group 21

### Chapter 2

- Figure 2.1: Synthesis of acetylide-substituted late metal phosphoranimide clusters by transmetallation 23
- Figure 2.2: ORTEP diagram of  $[\text{Fe}(\text{CCPh})(\text{NPEt}_3)]_4$  26
- Figure 2.3: ORTEP diagram of  $[\text{CoMe}(\text{NPEt}_3)]_4$  33
- Figure 2.4: Qualitative d-orbital correlation diagram summarizing the electronic effects associated with distorting a tetrahedral-ligand field around Co(II) 36

Figure 2.5: Energy splitting of the cobalt d-orbitals in the local trigonal-pyramidal ligand field at one corner of the cube	37
Figure 2.6: Cyclic voltammogram of $[\text{CoMe}(\text{NPEt}_3)_4]$ in THF and difluorobenzene	39
Figure 2.7: Irreversible oxidation/reduction of $[\text{Re}_2(\mu\text{-Cl})_2\text{Cl}_4(\text{PMe}_3)_4]$	40
Figure 2.8: Cyclic voltammogram of $[\text{CoMe}(\text{NPEt}_3)_4]$ in the presence of equimolar amounts of cobaltocene and ferrocene in tetrahydrofuran	43
Figure 2.9: ORTEP diagram of $[\text{CoMe}(\text{NPEt}_3)_4]\text{PF}_6$	46
Figure 2.10: Electron counting and the EAN rule for $[\text{CoMe}(\text{NPEt}_3)_4]$	49
Figure 2.11: Solution UV-Vis of $[\text{CoMe}(\text{NPEt}_3)_4]$ and $[\text{CoMe}(\text{NPEt}_3)_4]\text{PF}_6$ before and after reaction with hydrogen	52
Figure 2.12: $\sigma$ -CAM and OA/RE pathways for the reaction of $[\text{CoMe}(\text{NPEt}_3)_4]$ with hydrogen	57
Figure 2.13: Metathesis reactions of two similar iridium systems shown to proceed by different mechanisms	59
Figure 2.14: Hydrogen activation at a single iridium centre with intramolecular hydride transfer to give a bimetallic dihydride complex	60
Figure 2.15: Schematic and DFT depictions of the HOMO of $[\text{CoMe}(\text{NPEt}_3)_4]$	61
Chapter 3	
Figure 3.1: Organosulfur moieties common in crude oils	64
Figure 3.2: Common coordination modes observed in thiophene coordinated metal complexes	67
Figure 3.3: C–S and C–H bond activation by an electron rich low-valent rhodium fragment	70
Figure 3.4: A bis(phosphine) nickel hydride dimer capable of stoichiometric desulfurization of dibenzothiophene under ambient conditions	73

Figure 3.5: A generalized cycle for the catalytic hydrodesulfurization of an organosulfur substrate by a transition metal cluster	85
Figure 3.6: Mechanistic proposal for the activation of $[\text{CoMe}(\text{NPEt}_3)]_4\text{PF}_6$ for the catalytic desulfurization of dibenzothiophene	89
Figure 3.7: Mechanistic proposal for the first C–S bond cleavage and M–C hydrogenolysis events for the catalytic desulfurization of dibenzothiophene by $[\text{CoMe}(\text{NPEt}_3)]_4\text{PF}_6$	92
Figure 3.8: Mechanistic proposal for the C–S bond activation, Co–C bond hydrogenolysis, and catalyst regeneration steps of the catalytic desulfurization of dibenzothiophene by $[\text{CoMe}(\text{NPEt}_3)]_4\text{PF}_6$	94
Chapter 4	
Figure 4.1: Three aromatic alcohols used in lignin synthesis by enzymatic dehydrogenative polymerization.	114
Figure 4.2: Schematic representation of a softwood lignin	115
Figure 4.3: Ether C–O bond hydrogenolysis by a tandem catalyst system consisting of a lanthanide triflate species and supported palladium nanoparticles	123

## List of Schemes

Chapter 1		
	Scheme <b>1.1</b> .....	5
	Scheme <b>1.2</b> .....	7
Chapter 2		
	Scheme <b>2.1</b> .....	29
	Scheme <b>2.2</b> .....	42
	Scheme <b>2.3</b> .....	54
Chapter 3		
	Scheme <b>3.1</b> .....	71
	Scheme <b>3.2</b> .....	72
	Scheme <b>3.3</b> .....	74
Chapter 4		
	Scheme <b>4.1</b> .....	121
	Scheme <b>4.2</b> .....	125
	Scheme <b>4.3</b> .....	127
	Scheme <b>4.4</b> .....	130
	Scheme <b>4.5</b> .....	132
	Scheme <b>4.6</b> .....	135
	Scheme <b>4.7</b> .....	136

## List of Equations

### Chapter 1

Eqn. 1.1.....	13
Eqn. 1.2.....	14
Eqn. 1.3.....	17

### Chapter 2

Eqn. 2.1.....	23
Eqn. 2.2.....	25
Eqn. 2.3.....	31
Eqn. 2.4.....	44
Eqn. 2.5.....	49

### Chapter 3

Eqn. 3.1.....	63
Eqn. 3.2.....	75
Eqn. 3.3.....	79
Eqn. 3.4.....	81
Eqn. 3.5.....	82
Eqn. 3.6.....	83
Eqn. 3.7.....	98
Eqn. 3.8.....	103
Eqn. 3.9.....	105
Eqn. 3.10.....	106
Eqn. 3.11.....	107
Eqn. 3.12.....	108
Eqn. 3.13.....	109

### Chapter 4

Eqn. 4.1.....	117
Eqn. 4.2.....	118

Eqn. 4.3.....	119
Eqn. 4.4.....	119
Eqn. 4.5.....	133
Eqn. 4.6.....	138

## List of Abbreviations

Å	Angstroms
atm	Atmosphere
Bu	Butyl
cm <sup>-1</sup>	Wavenumbers
COD	Cyclooctadiene
Cp	Cyclopentadienyl
Cp*	Pentamethylcyclopentadienyl
Cy	Cyclohexyl
D	Days
DFT	Density functional theory
E	Electron
EHMO	Extended Huckel molecular orbital
equiv.	Equivalents
Et	Ethyl
G	Grams

h	Hours
HOMO	Highest occupied molecular orbital
Hz	Hertz
IR	Infrared
kcal	Kilocalories
KDA	Potassium di-isopropyl amide
LDA	Lithium di-isopropyl amide
L <sub>n</sub>	Ligand
LUMO	Lowest unoccupied molecular orbital
M	Metal
Me	Methyl
mg	Milligrams
MHz	Megahertz
min	Minutes
mL	millilitre
mmol	millimoles
mol	Moles

NHC	N-heterocyclic carbene
NMR	Nuclear magnetic resonance
Ph	Phenyl
Pm	Picometers
Ppm	Parts per million
Pr	Propyl
R	Generic alkyl/aryl substituent
r.t.	Room temperature
SOMO	Singly occupied molecular orbital
<sup>t</sup> Bu	Tert-butyl
THF	Tetrahydrofuran
TMS	Trimethylsilyl
TOF	Turnover frequency
$\sigma$ -BM	Sigma bond metathesis
$\sigma$ -CAM	Sigma complex assisted metathesis
M	Mu (bridging mode)
°C	Degrees Celsius

$\nu$

Nu (frequency)

$\eta$

Eta (hapticity)

# ***1. Ligands and precursors: Iminophosphoranes and transition metal phosphoranimide clusters***

## *1.1 Introduction and background*

### *1.1.1 Structure and bonding in the phosphoranimide ligand*

The phosphoraneiminato anion  $[\text{R}_3\text{PN}]^-$  (also known as phosphoranimide and phosphoranimido) is a versatile ligand for coordination of transition metals and main group elements. The ligand exhibits excellent thermal stability due, in part, to the high oxidation state of the phosphorus atom. As nitrogen-based anionic ligands, phosphoranimides are capable of forming strong bonding interactions with electrophilic metals. The  $[\text{R}_3\text{PN}]^-$  ligand is valence isoelectronic with a series of common ligands, including silyloxo  $[\text{R}_3\text{SiO}]^-$  and silylimido  $[\text{R}_3\text{SiN}]^{2-}$ .<sup>2</sup> The resonance structures in Figure 1.1 illustrate how the phosphoranimide ligand can donate up to six electrons to a metal centre: two *via*  $\sigma$ -donation and two or four *via*  $\pi$ -donation. While a discrete  $[\text{R}_3\text{PN}]^-$  ion has not been isolated, DFT calculations indicate that Lewis structure **A** best describes the bonding in the anion.<sup>3</sup> In Lewis structure **A** electron density is shared between nitrogen and phosphorus in the form of a double bond, and the nitrogen atom is singly anionic. Upon coordination to a transition metal the negative charge on nitrogen increases while the N–P bond order decreases. Thus, the zwitterionic resonance structure **B** best describes the bonding in metal-bound phosphoranimide ligands. In this description the N–P bond is best considered to be a strongly polar single bond.

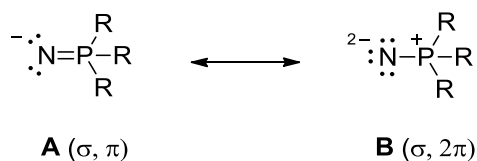


Figure 1.1: Lewis resonance structures for the phosphoranimide ligand.

Extended Hückel calculations provide a more detailed description of the bonding in phosphoranimide ligands.<sup>3</sup> The highest occupied orbitals of the  $[\text{R}_3\text{PN}]^-$  ligand consist of one  $sp$ -hybridized orbital ( $\sigma$ -symmetry) and a pair of degenerate  $p$ -orbitals ( $\pi$ -symmetry) (Figure 1.2). The highest occupied molecular orbitals of the cyclopentadienyl ligand  $[\text{Cp}]^-$  are similar; phosphoranimide and cyclopentadienyl ligands are *isolobal*. Isolobal ligands show similar bonding capabilities and electronic structures.

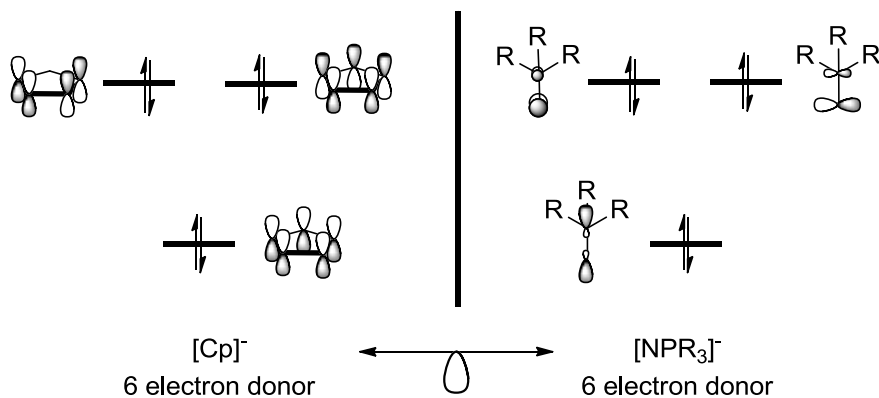


Figure 1.2: Isolobal relationship between cyclopentadienyl- and phosphoranimido-ligands. Two fragments or molecules are said to be isolobal if their frontier orbitals are (1) the same in number, (2) pose the same symmetries, (3) have the same occupancy by electrons, and (4) are similar in radial extension.<sup>4</sup>

A series of early transition metal complexes illustrate the isolobal relationship between  $[\text{Cp}]^-$  and  $[\text{R}_3\text{PN}]^-$  and highlight some important characteristics of the

phosphoranimide ligand (Figure 1.3).<sup>5</sup> Cyclopentadienyl and phosphoranimide ligands occupy approximately similar volumes when coordinating a metal centre. This feature is quantified by Tolman's cone angle, a measure of the maximum angle subtended at the metal.<sup>6</sup> The Tolman cone angle for tri-*t*-butylphosphoranimide is 87°, which is similar to that of the cyclopentadienyl ligand (83°). While the volumes occupied by these two ligand types are similar, the distance separating the metal centre from the ligand's steric bulk is notably different. The [TiCp(NPR<sub>3</sub>)Cl<sub>2</sub>] complexes(1-4) in Figure 1.3 have Ti–P distances of approximately 360 pm whereas the Ti–Cp-centroid distances are approximately 220 pm. The N–P bond of the phosphoranimide ligand acts as a molecular “spacer” between the metal centre and the bulk of the ligand. This is a key feature in terms of ligand design for catalysis; the phosphoranimide ligand occupies a large spatial “volume fraction” of metal coordination sphere without crowding the metal itself, leaving adequate room for the metal(s) to participate in other chemistry.<sup>7</sup>

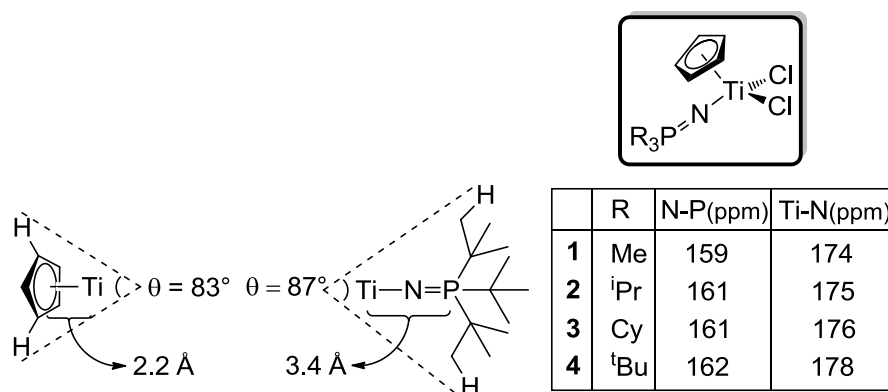


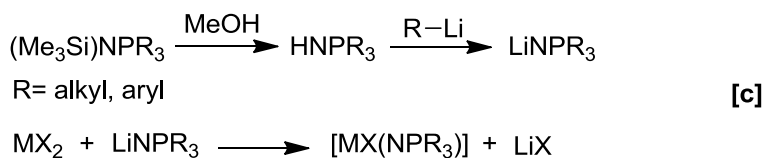
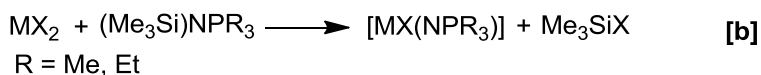
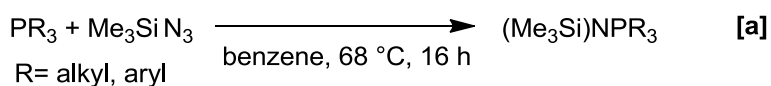
Figure 1.3: Cone angles and key bond distances for a series of cyclopentadienyl phosphoranimido-titanium halide complexes.<sup>5</sup>

The table of bond distances in Figure 1.3 highlights another important feature of phosphoranimide ligands: tuneable steric and electronic properties, through variance of the substituent (R) groups at phosphorus. The observed N–P bond lengths increase with the electron donating ability of the R groups (Me < Cy ~ <sup>i</sup>Pr < <sup>t</sup>Bu). This implies that shorter N–P bond lengths are the result of additional contributions of electron density from nitrogen to the empty phosphorus  $\pi$ -type orbital. Highly electron donating substituents (*i.e.* more bulky alkyl groups) are more capable of stabilizing the electrophilic phosphorus centre, which in-turn, decreases the need for electron donation from nitrogen resulting in a longer N–P bond. The same reasoning applies to the observed Ti–N bond lengths: More electron donating substituents on phosphorus reduce N→P electron donation, yielding more nucleophilic nitrogen atoms capable of forming stronger (shorter) bonds with the  $d^0$  metal centre. The phosphoranimide ligand can be prepared bearing a wide variety of alkyl and aryl substituents. Consequently, the phosphoranimide ligand provides an opportunity to manipulate the steric *and* electronic state of a metal's coordination sphere by modulating the substituents at phosphorus.

### *1.1.2 Methods of synthesis of the phosphoranimide ligand*

There are two common precursors used to install phosphoranimide ligands on transition metals, neutral N-(trimethylsilyl)phosphoranimines and alkali-metal salts with phosphoranimide anions. N-(trimethylsilyl)phosphoranimines are prepared by a Staudinger-type oxidation of the desired phosphine with

trimethylsilylazide (Scheme **1.1 [a]**)<sup>2</sup>. Typical procedures involve heating the reactants to reflux in benzene to promote the loss of dinitrogen from the intermediate phosphazide. The vastly different boiling points of the starting materials and the products allow purification by vacuum distillation. A wide variety of alkyl and aryl substituted N-(trimethylsilyl)phosphoranimines can be prepared in this fashion.



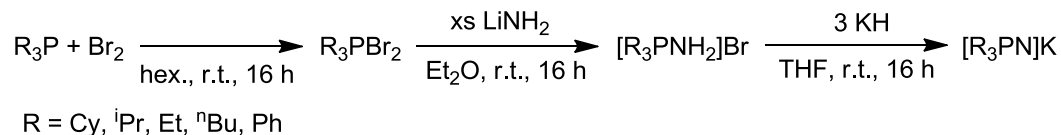
### Scheme 1.1

The desilylation of N-(trimethylsilyl)phosphoranimines can be executed by direct addition to the metal **[b]** or by hydrolysis **[c]**. For direct addition to the metal, the desilylation is only feasible when conducted in the melt-phase using low molecular weight silylphosphoranimines (*i.e.*, R = Me, Et; see section 1.1.4). This method involves treatment of the N-(trimethylsilyl)phosphoranimine with an anhydrous metal(II) halide precursor in the presence of excess sodium fluoride or potassium fluoride. The stability of the Si–F bond provides a thermodynamic driving force for the desilylation. An alternative method involving hydrolysis of

the N–Si bond followed by deprotonation to yield an anionic phosphoranimide is also known.<sup>8</sup> A typical procedure involves desilylation of the N-(trimethylsilyl)phosphoranimine in anhydrous methanol to form the intermediate phosphoranimine. Subsequent deprotonation using an alkyl-lithium reagent affords the corresponding lithium phosphoranimide, which can then be used to install the phosphoranimide ligand on a transition metal by salt metathesis (see section 1.1.4).

Both the direct addition to a transition metal (**b**), and the formation of the anionic phosphoranimide for salt metathesis (**c**) require the use of N-(trimethylsilyl)phosphoranimine precursors and therefore require the use of silylazide reagents. Trimethylsilylazide is potentially explosive, particularly when used on large scale, acutely toxic (level 2: oral, dermal, inhalation risks) and expensive.<sup>9</sup> Dehnicke and co-workers have published an ‘azide-free’ method of synthesis for the alkali-metal salts of triphenyl-, trimethyl- and triethylphosphoranimide.<sup>10</sup> This procedure, the reaction between a dihalophosphorane and a heavier metal amide (M = K, Rb, Cs), can be conducted on multi-gram scale. However it does require caution, especially in the Rb and Cs analogs, which require the use of highly reactive metal(0) powders in ammonia. Access to the larger-alkali metal phosphoranimide salts is synthetically useful, as they are vastly more soluble than the smaller (Li, Na) analogs. The increased solubility of the larger alkali metal phosphoranimide salts is presumably due to their tendencies to form large unsolvated aggregates.<sup>10</sup>

Hamilton and co-workers in our group have extended this chemistry to scalable syntheses of a wide range of additional trialkyl- and triarylphosphoranimides (Scheme 1.2)<sup>11</sup>. This modified methodology does not require ammonia as a reaction solvent.



### Scheme 1.2

In this optimized procedure, the parent phosphine is oxidized with bromine in a polar aprotic solvent, giving the dibromophosphorane ( $R_3PBr_2$ ). Although the structure of the phosphorane depends on the polarity of the solvent (inner vs. outer sphere coordination of the second bromine atom), the choice of solvent is not key to controlling the subsequent reactivity; both intermediates react cleanly with lithium amide in ethereal solvent to afford the protonated phosphoraniminium bromide salt,  $[R_3PNH_2]Br$ , which can be isolated by simple filtration. The phosphoraniminium salts are ideal ligand precursors because they are air and water stable and can be stored on the bench top indefinitely. Deprotonation gives the neutral phosphoranimine ( $R_3PNH$ ) or the anionic phosphoranimide ( $R_3PNK$ ), depending on the stoichiometry of the base.

#### 1.1.3 Structure and bonding in transition metal phosphoranimide complexes

The coordination chemistry of phosphoranimides has developed into a broad area of research. The chemistry of phosphoranimide- main group<sup>12</sup> and transition

metal<sup>2</sup> complexes has been reviewed, therefore this discussion of structure and bonding will focus on issues most relevant to the development of phosphoranimide-supported late transition metal clusters for reductive catalysis.

Phosphoranimide ligands coordinate transition metals in a number of modes. The key metrics for classifying phosphoranimide-transition metal bonding are M–N bond lengths and M–N–P bond angles, obtained from single-crystal X-ray diffraction. The bonding mode observed is primarily dependent on the oxidation state of the transition metal. Bonding modes **A** and **B** are preferred for coordination to transition metals in high oxidation states (Figure 1.4). Bonding mode **A** implies a ( $\sigma$ ,  $2\pi$ ) set of orbitals involved in a metal-nitrogen triple bond, resulting in near linear M–N–P bond angles. These features are illustrated in the structure of  $[\text{WCl}_5(\text{NCl}_3)]$  (**5**), which has a short W–N bond (177 pm) and a bond angle close to  $180^\circ$  ( $176^\circ$ ).<sup>13</sup> The phosphoranimide ligand of **5** acts as a six electron donor towards the high oxidation state tungsten atom ( $\text{W}^{+6}$ ,  $d^0$ ). Bonding mode **B** involves a ( $\sigma$ ,  $\pi$ ) set of orbitals engaging in a metal–nitrogen double bond. The remaining  $\pi$ -type nitrogen orbital is primarily localized on the nitrogen atom, resulting in M–N–P bond angles that are more acute than those of bonding mode **A**. The phosphoranimide-metal bonding in  $[\text{WCl}_4(\text{NCl}_3)_2]$  (**6**) exemplifies bonding mode **B**; the W–N–P bond angles are bent ( $160^\circ$ ) and the W–N bond lengths are longer than those observed in **5** (182 vs. 177 pm).<sup>13</sup> In bonding mode **B** the phosphoranimide ligand is formally a 4-electron donor. By this count, **6** is a 16 electron complex, which resonates with its observed electrophilic reactivity.<sup>2</sup>

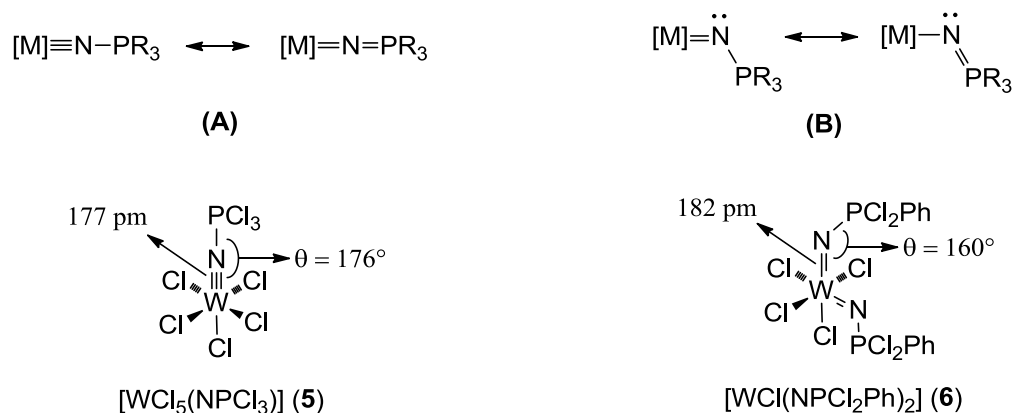
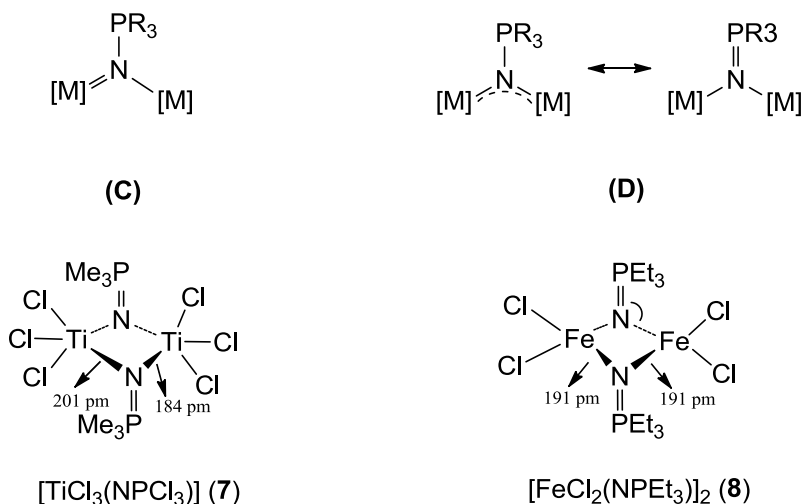


Figure 1.4: Phosphoramidate bonding modes **A** and **B** with representative examples.<sup>13,2</sup>

In bonding modes **C** and **D**, the phosphoramidate moiety acts as a  $\mu_2$ -bridging ligand (Figure 1.5). In both cases the phosphoramidate is formally a six electron donor, engaging in bonding interactions with the  $\sigma$ - and both  $\pi$ -type orbitals on nitrogen. Bonding modes **C** and **D** differ with respect to the symmetry of bonding interactions. In bonding mode **C**, the phosphoramidate ligand bridges unsymmetrically; the two M–N bonds are different lengths. In bonding mode **D**, the M–N bonds are the same length and the bridge is symmetrical. The phosphoramidate-supported titanium complex  $[TiCl_3(NPMe_3)]_2$  (**7**) is illustrative of bonding mode **C**. In this dimer each phosphoramidate forms one short and one long Ti–N bond (201 and 184 pm respectively), to give an unsymmetrical four-membered ring. In the presence of a Lewis-basic solvent (*e.g.*, THF) the dimer is split by cleavage across the two long Ti–N bonds. Facile cleavage of the longer (weaker) of the two M–N bonds in unsymmetrical  $\mu_2$ -phosphoramidate bridges is common.<sup>2</sup> Cleavage of the symmetrical M–N bonds in  $\mu_2$ -phosphoramidate

bonding mode **D** does not occur as readily. For example, all four Fe–N nitrogen bonds in  $[\text{FeCl}_2(\text{NPEt}_3)]_2$  (**8**) are the same length (bonding mode **D**), and the complex retains its dimensionality at reflux in common Lewis basic solvents.<sup>14</sup>



**Figure 1.5:** The unsymmetrical **C** and symmetrical **D**  $\mu_2$ -phosphoramidate bonding modes and representative examples.<sup>2</sup>

Phosphoramidates predominantly coordinate to low-oxidation state transition metals *via* bonding mode **E** (Figure 1.6). In this state, the phosphoramidate acts as a  $\mu_3$ -bridging ligand. The vast majority of phosphoramidate complexes that exhibit bonding mode **E** maintain a phosphoramidate to metal ratio of 1 : 1, resulting in a cube-like cluster with alternating metal and nitrogen atoms occupying the vertices. The equivalent metal centres adopt tetrahedral coordination, to three phosphoramidate nitrogen atoms and an exocyclic anionic ligand (almost always a halide). When coordinating through bonding mode **E**, phosphoramidates are best described as weak-field ligands because the donating capacity is diffused amongst three metals centres. The M–N bonds are generally

symmetrical, giving  $[M_4N_4]$  cores that deviate only slightly from an ideal cubic structure. These features are exemplified by the halide capped nickel-phosphoranimide cluster  $[NiBr(NPMe_3)]_4$  (**9**) which has twelve close-to-uniform M–N bonds ( $202.1 \pm 0.2$  pm), and M–N–M and N–M–N bond angles of  $89.5^\circ$  and  $90.5^\circ$  respectively.<sup>15</sup>

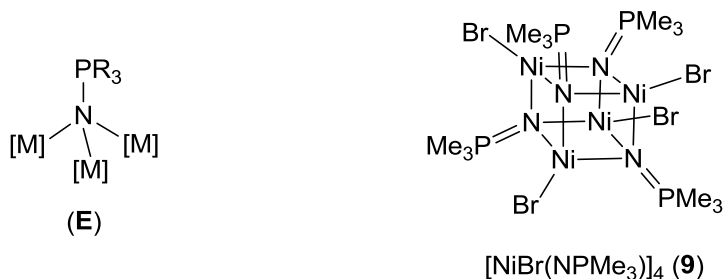


**Figure 1.6**  $\mu_3$ -Phosphoranimide bonding mode **E** and a representative cluster,  $[NiBr(NPMe_3)]_4$ .<sup>15</sup>

#### *1.1.4 Synthesis of halide-substituted late metal phosphoranimide clusters by high temperature fluoro-desilylation and low temperature salt metathesis*

Dehnicke and co-workers have prepared a series of halide-substituted late metal phosphoranimide clusters, all exhibiting the heterocubane structure, by allowing an anhydrous metal(II) halide to react in molten N-(trimethylsilyl)phosphoranimine at high temperature (Figure 1.7). Excess sodium or potassium fluoride is required to encourage desilylation of the phosphoranimine – the strong Si–F bond and the release of gaseous trimethylsilyl fluoride drive the reaction to completion. In the absence of anhydrous fluoride, the reactions yield only dative N-(trimethylsilyl)phosphoranimine metal(II) halide compounds.

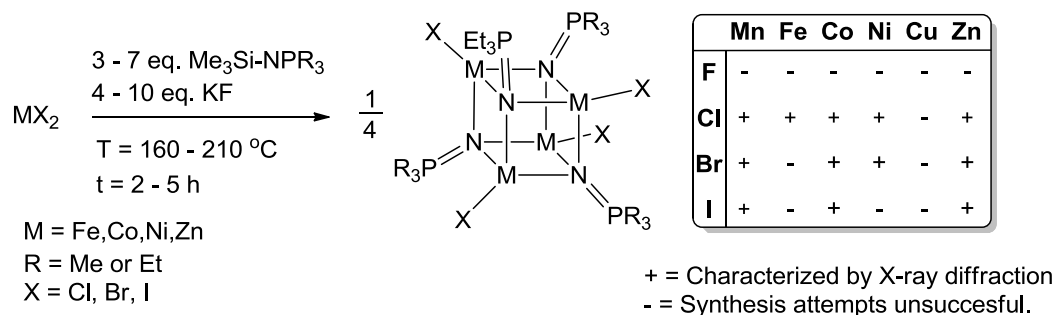


Figure 1.7: ‘Melt-preparation’ of halide-substituted late metal phosphoranamide clusters.<sup>16</sup>

There are a number of limitations to this method of synthesis. First, the molten-state of the reaction requires an excess (two to six equivalents) of N-(trimethylsilyl)phosphoranimine.<sup>i</sup> Second, as noted, the preparation of the N-(trimethylsilyl)phosphoranimines require the use of expensive and hazardous organic azide reagents. Third, and most importantly, the procedure is only possible when using small trialkyl phosphoranamide complexes (R = Me, Et); the high melting points of larger trialkyl and triaryl derivatives preclude use of the molten state.

Phosphoranamide ligands with large alkyl groups, can in principle be installed on late metals by anionic salt metathesis at low temperature. Although very little synthetic work has been reported, Stephan and co-workers have prepared the iron(III) dimer  $[\text{FeBr}_2(\text{NP}^t\text{Bu}_3)]_2$  (**10**) by addition of lithium tri-*tert*-butylphosphoranamide to a slurry of iron(III) bromide in toluene (Eqn. 1.1)<sup>14</sup>.

<sup>i</sup>Although the authors don’t say so, it is possible to collect un-reacted (trimethylsilyl)phosphoranimine and purify it by vacuum distillation.



Eqn. 1.1

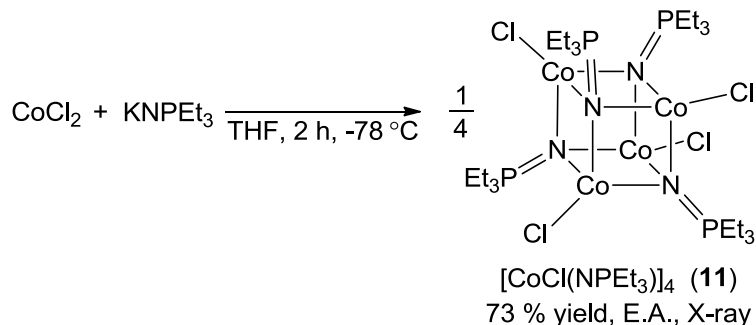
## 1.2 Results and Discussion

### 1.2.1 Synthesis of $[\text{CoCl}(\text{NPEt}_3)]_4$ by low temperature salt metathesis

The cobalt(II) phosphoranimide cluster  $[\text{CoCl}(\text{NPEt}_3)]_4$  (**11**) is a useful starting material for the preparation of discrete precatalyst clusters for reductive processes such as hydrodesulfurization and hydrodeoxygenation. This cluster can be prepared by high-temperature fluoro-desilylation, but the preparation lacks scalability, as discussed above. The first contributions to our research objectives was the adaptation of Stephan's low-temperature metathesis methodology to the preparation of **11** and the development of a scalable (>10 g) procedure. Prior to this work, Stephan's anionic metathesis methodology had not been used to prepare transition metal complexes of the less sterically-imposing trialkylphosphoranimides.

Complex **11** is optimally prepared by drop-wise addition of a solution of potassium triethylphosphoranimide to a slurry of anhydrous cobalt(II) chloride in THF (Eqn. 1.2). Cobalt dichloride is partially soluble in THF, reducing the

potential for rate-limited heterogeneous reaction conditions. The reaction is best run at low temperature to prevent equilibrium disproportionation to form cobalt dichloride and the previously unreported cobalt(II) bis-triethylphosphoranimide (section 1.2.3).



**Eqn. 1.2**

Of the alkali-metal phosphoranimides screened for this reaction, potassium triethylphosphoranimide provided the highest yield and the easiest purification. Potassium triethylphosphoranimide is soluble in common organic solvents and the potassium chloride by-product can be removed by simple filtration. Trials with lithium and sodium triethylphosphoranimide required filtration and subsequent recrystallization(s) to remove the lithium/sodium chloride by-products. Optimal yields of **11** were obtained with phosphoranimide : cobalt ratios between 1.1 and 1.0. The slight excess of potassium triethylphosphoranimide results in the formation of a small amount of a hexane soluble byproduct that can be washed away with low-polarity organic solvents; **11** is soluble in toluene but not in hexane or pentane. Thus the optimal work-up involves removing the reaction

solvent under reduced pressure, trituration with toluene and filtration to remove potassium chloride, removing the toluene solution under reduced pressure, and washing the residual solid with hexane. This procedure yields green crystalline material that matches the chemical formula  $[\text{CoCl}(\text{NPEt}_3)_4]$  by elemental analysis (73 % yield). Single-crystal diffraction experiments confirm the identity of the product to be the same as that prepared by high-temperature fluorodesilylation, as reported by Dehnicke.<sup>17</sup>

### *1.2.2 Synthesis of related halide-substituted late metal phosphoranimide clusters by low temperature salt metathesis*

The salt metathesis strategy for the preparation of metal clusters with small alkylphosphoranimide ligands can be extended to synthesis of the analogous iron complex,  $[\text{FeCl}(\text{NPEt}_3)_4]$  (**12**). Iron(II) chloride is insoluble in THF and is best replaced by the more soluble precursor  $\text{FeCl}_2 \cdot \text{dioxane}$ . Maintaining a slow rate of potassium triethylphosphoranimide addition is critical to the success of this reaction, ensuring the isolation of **12** in good yield. Elemental analysis of the iron compound isolated from this procedure matches the chemical formula  $[\text{FeCl}(\text{NPEt}_3)_4]$  and X-ray diffraction confirmed that the product is identical to that prepared by high temperature fluoro-desilylation.<sup>18</sup>

Concomitant with this work to improve the synthesis of halide-substituted late metal complexes of sterically small trialkylphosphoranimides, other members of the Stryker group used salt metathesis to optimize the synthesis of cobalt and iron clusters of tri-*tert*-butyl- and tricyclohexylphosphoranimides.<sup>19</sup> The large alkyl

substituents on these phosphoranimide ligands sterically preclude the formation of tetramers;  $[\text{FeBr}(\text{NP}^t\text{Bu}_3)]_2$  (**13**) and  $[\text{CoCl}(\text{NPR}_3)]_2$  (**14/15**) are thus dimeric in the solid state with phosphoranimide ligands engaging in  $\mu_2$ -bonding mode **D** (Figure **1.8**).

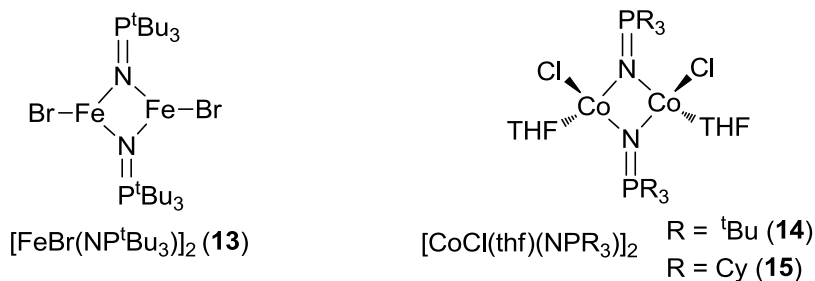
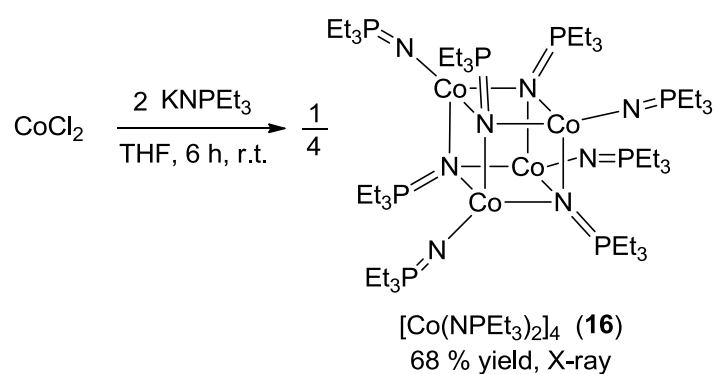


Figure **1.8**: Dimeric halide-substituted late metal phosphoranimide complexes with bulky-alkyl substituents at phosphorus.<sup>18</sup>

### 1.2.3 Homoleptic bis(phosphoranimide) cobalt(II) complexes: $[\text{Co}(\text{NPEt}_3)_2]_4$ and related clusters

Salt metathesis also allows access to a series of homoleptic bis(phosphoranimide) metal clusters of the late first-row transition metals. Fluoro-desilylation methodology cannot access this class of clusters: trimethylsilylphosphoranimines are not nucleophilic enough to displace the second halide from a metal(II) salt, even under forcing conditions.<sup>16</sup> The homoleptic bis(phosphoranimide) complex  $[\text{Co}(\text{NPEt}_3)_2]_4$  (**16**), however, was readily synthesized and characterized by a simple salt metathesis. The tetrameric cluster is obtained upon treatment of anhydrous cobalt dichloride with two equivalents of potassium triethylphosphoranimide (Eqn. **1.3**). Unlike the salt-metathesis preparation of **11**, this reaction can be conducted at room temperature, as **16** cannot

conproportionate. Careful control of the reaction stoichiometry, using slightly less than two equivalents of potassium triethylphosphoranimide per equivalent of cobalt(II) chloride, ensures that **16** is the only species present after the reaction that is soluble in non-polar media. This simplifies the purification: trituration of the crude products with hexanes separates **16** from the potassium chloride and residual **11**.



Eqn. **1.3**

The choice of recrystallization techniques for the purification of **16** is limited by the high solubility of the cluster. Single-crystals were grown by slow evaporation of a concentrated hexane solution at  $-35\text{ }^{\circ}\text{C}$ . X-ray diffraction analysis confirm the tetrameric  $\text{Co}_4\text{N}_4$  heterocubane core, similar to that of **11** (Figure **1.9**).

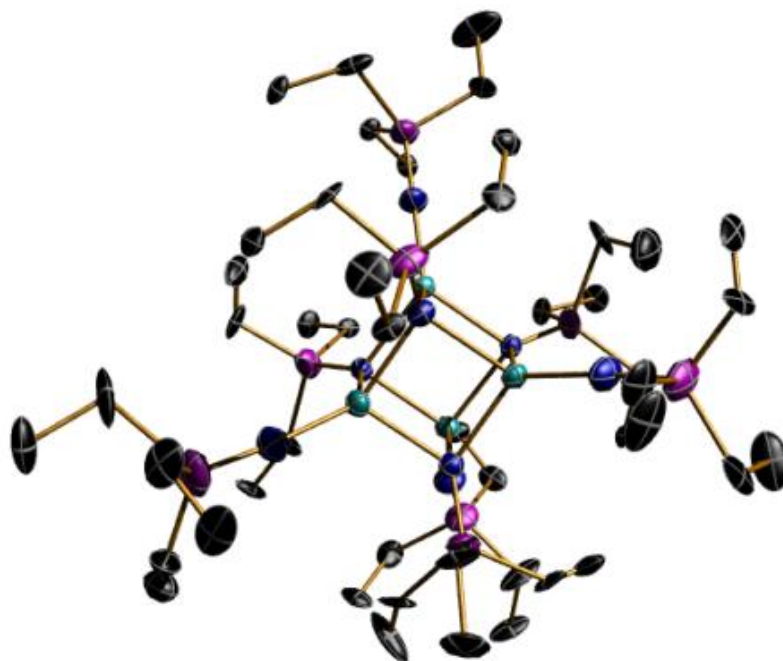


Figure **1.9**: ORTEP diagram of the homoleptic bis(phosphoranimide)  $[\text{Co}(\text{NPEt}_3)_2]_4$  (**16**). Thermal ellipsoids are shown at 30 % probability. Hydrogen atoms have been omitted for clarity. The crystallographic disorder in the ligand ethyl groups is significant, but the coordinates of the  $\text{Co}_4\text{N}_4$  core are well defined.

Significant disorder in the coordinates of the ethyl groups is clear from the structure, but the most important features of the cluster could be reliably extracted. Table **1.1** contains relevant average bond lengths and angles for **16**.

Table **1.1**: Key bond lengths and bond angles for the bis(phosphoranimido) cobalt(II) cluster  $[\text{Co}(\text{NPEt}_3)_2]_4$ .

Interatomic distances (pm)					Bond angles (°)	
Co••Co	Co–N	N–P	Co–N <sub>(exo)</sub>	P–N <sub>(exo)</sub>	N–Co–N	Co–N <sub>(exo)</sub> –P
290.22(1)	207.86(5)	154.88(5)	188.54(6)	149.44(9)	90.9(1)	173.6(9)

The heterocubane core in **16** is very close to ideal; the N–Co–N and Co–N–Co bond angles are 89.1(3)° and 90.9(1)° respectively. This, in combination with the relatively long Co–N bond lengths in the core (207.86(5) pm) result in **16** having the longest Co•••Co interatomic distance of the cobalt-phosphoranimide heterocubane clusters reported to date. Very little is known about how metal-metal electronic communication is affected by variations in interatomic distances in the heterocubane series.

The four exocyclic (terminal) phosphoranimide ligands of **16** bond *via* mode **A**, with Co–N–P bond angles close to 180° (173.6(9)°). This is both unexpected and unusual: linear bonding mode **A** is normally observed only in early metal phosphoranimide complexes. In **16**, this coordination mode implies multiple bond character in the unbridged Co–N interaction; the nitrogen atom is sp-hybridized with near linear geometry, presumably facilitating efficient overlap between  $\pi$ -symmetric orbitals on nitrogen and cobalt. The exocyclic Co–N bond lengths in **16** average 188.54(6) pm, much shorter than those comprising the heterocubane core (average Co–N bond length = 207.86(5) pm) and well short of the accepted range of Co–N single bonds in the literature.<sup>20</sup>

The homoleptic cobalt dimer [Co(N(TMS)<sub>2</sub>)<sub>2</sub>]<sub>2</sub> (**17**)<sup>21</sup> provides a useful point of comparison for discussion of structure and bonding in **16**. The geometry of the terminal amido ligands in **17** also implies that the ligand to metal  $\pi \rightarrow d$  bonding interaction is facilitated by N-rehybridization (Figure **1.10**). In this structure, N' and N'' are trigonal planar with bond angles near 120°. Like **16**, this complex also

has exocyclic Co–N bond lengths that are shorter than the bridging Co–N bond lengths (192.3 pm and 206.2 pm respectively).

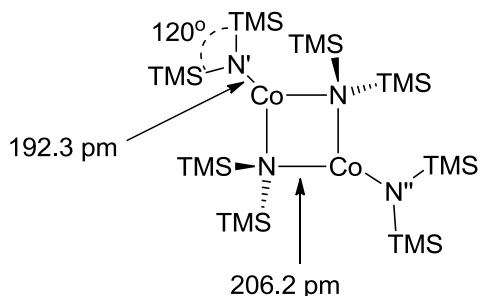


Figure **1.10**: Key bond lengths and bond angles in [Co(N(TMS)<sub>2</sub>)<sub>2</sub>]<sub>2</sub> (**17**).<sup>21</sup> The 120° bond angles around N' and N'' imply an orbital rehybridization to allow  $\pi \rightarrow d$  electronic interactions.

Concurrent work in the group has yielded late metal bis(phosphoranimide) clusters of the large tri-*tert*-butyl- and tricyclohexylphosphoranimides. That series shows the clear relationship between the steric encumbrance of the phosphoranimide substituents and the nuclearity of the cluster (Figure **1.11**). Although the majority of the ligand volume is displaced from the metal centre, the tri-*tert*-butyl- and tricyclohexylphosphoranimide ligands are too sterically imposing to allow tetramer formation around Co(II) centres; both [Co(NPCy<sub>3</sub>)<sub>2</sub>]<sub>2</sub> (**18**) and [Co(NP<sup>*t*</sup>Bu<sub>3</sub>)<sub>2</sub>]<sub>2</sub> (**19**) are dimeric in the solid state.<sup>22</sup> The planar, less sterically demanding phenyl substituents lead to a third structural motif; bis(triphenylphosphoranimide) cobalt(II), [Co(NPPh<sub>3</sub>)<sub>2</sub>]<sub>3</sub> (**20**), is trimeric in the solid state, demonstrating a clear correlation between ligand steric pressure and cluster nuclearity. The ethyl groups of **16** are small enough to allow the formation of a tetrametallic cluster. While the series of homoleptic bis(phosphoranimide)

clusters are attractive candidates for reductive catalysis, very little work has as yet been done to elucidate the relationship between cluster dimensionality and catalytic activity. In the Stryker group, Dominique Hebert demonstrated that **19** is an active catalyst for the hydrogenation of alkenes and alkynes.<sup>23</sup> This complex has the lowest cluster dimensionality and the most electron rich metal centres in the bis(phosphoranimide) cluster series.

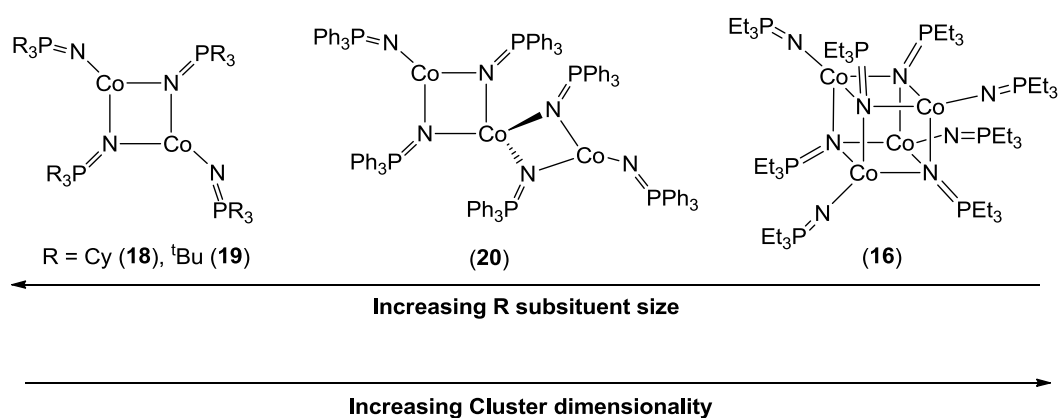


Figure 1.11: Homoleptic cobalt(II) phosphoranimide clusters synthesized and characterized by researcher in the Stryker group.

## ***2. Alkyl and alkynyl capped phosphoranimido-metal complexes by transmetallation***

The most important synthetic work outlined in this chapter features an adaptation of traditional transmetallation methodologies to overcome difficulties in the synthesis of the tetramethyl-substituted cobalt phosphoranimide cluster  $[\text{CoMe}(\text{NPEt}_3)]_4$ , a precatalyst for reductive catalysis. The alkylation procedures developed by Dehnicke and co-workers for manganese fail in the case of cobalt.<sup>16</sup> Alkynylation of the cobalt cluster, however, does proceed, and a series of alkynyl-substituted late-metal phosphoranimide clusters have been reported.<sup>17</sup> Section 2.1 provides a review of the synthesis and characterization of alkynylated late-metal phosphoranimide clusters and introduces the iron alkynyl complex  $[\text{Fe}(\text{CCPh})(\text{NPEt}_3)]_4$  that was synthesised and characterized as part of this research. The catalytic reactivity of  $[\text{Fe}(\text{CCPh})(\text{NPEt}_3)]_4$  is also discussed, highlighting the discovery that phosphoranimide-supported alkyl and alkynyl complexes are potent hydrogenation and hydrogenolysis catalysts. Section 2.2 details the synthesis and characterization of  $[\text{CoMe}(\text{NPEt}_3)]_4$  followed by a discussion of the structure, bonding, and redox activity of the cluster. Section 2.3 discusses the synthesis of the mixed-valence cluster  $[\text{CoMe}(\text{NPEt}_3)]_4\text{PF}_6$ . The differences between the neutral cluster  $[\text{CoMe}(\text{NPEt}_3)]_4$  and the cationic cluster  $[\text{CoMe}(\text{NPEt}_3)]_4\text{PF}_6$  are discussed in section 2.4.

## 2.1 Acetylide-substituted late metal phosphoranimide clusters

The most commonly employed method for the synthesis of metal alkyl and metal alkynyl complexes is the metathesis of a transition metal halide complex by a main group organometallic species (Eqn. 2.1).



M = Li, Mg, ...

M' = transition metal

Eqn. 2.1

Organolithium and -magnesium reagents are commonly used in these transmetallation processes. Both lithium and magnesium are highly electropositive, more so than the majority of transition metals metal centres, so they form stronger bonds with electronegative halides. As a result, the equilibrium constants for such transmetallation reactions are usually large.<sup>4</sup>

Dehnicke and co-workers used transmetallation protocols to prepare a series of acetylide-substituted late-metal phosphoranimide clusters, treating the parent halide derivatives with *in-situ* generated alkynyl lithium reagents (Figure 2.1).

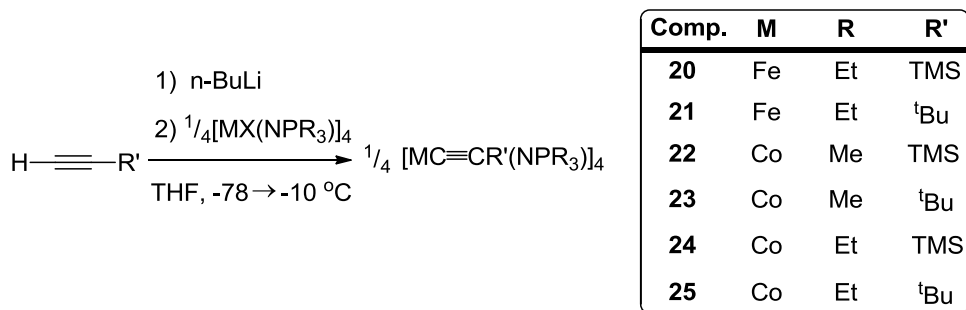


Figure 2.1 Synthesis of acetylide-substituted late metal phosphoranimide clusters by transmetallation.<sup>16</sup>

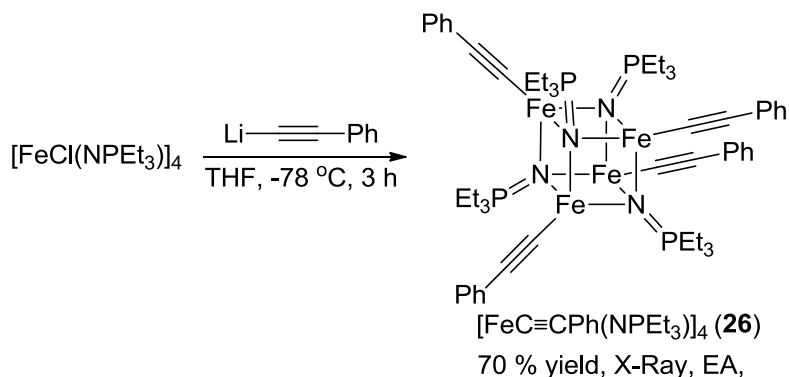
The solid-state structures of clusters **20–25** show an interesting effect of the metal on structure: while cobalt alkynyl complexes have near ideal cube-shaped cores (M–N–M bond angles close to 90°), the cores of the iron complexes are significantly distorted. For example, the M–N–M bond angles in cobalt compound **24** are  $91.8 \pm 0.2^\circ$ , while those in the iron complex **21** range from 92.1° to 95.4°. The distortions in the iron clusters arise from a Jahn-Teller effect.<sup>3</sup> The iron centres are formally Fe(II),  $d^6$  in a local  $C_{3v}$ -symmetry ligand field, resulting in one electron occupying a doubly-degenerate pair of orbitals; such molecular structures are unstable towards any distortion that destroys the 3-fold symmetry axis and removes the degeneracies. The cobalt centres are in a similar ligand field but the metals are  $d^7$ , resulting in doubly-degenerate orbitals that are both singly occupied, conferring no electronic advantage upon distortion of the cube.

The IR spectra of clusters **20–25** show single absorptions associated with the P=N and M–N stretches, in accord with the high molecular symmetry observed in the solid-state structures. Likewise, the IR spectra of **20–25** show single absorptions associated with the symmetric stretches of the carbon-carbon triple bonds.

Dehnicke and co-workers report the  $\nu(\text{CC})$  for the alkyne functionality in **20–25**, and make comparisons to the analogous “free” mono-substituted acetylene (HCCR) compounds.<sup>18,17</sup> However, related work by Lichtenberger and co-workers suggests that the relationship is not straightforward: mono- and di-substituted acetylenes absorb IR radiation of drastically different frequencies due to coupling effects between the  $\text{C}\equiv\text{C}$  and  $\text{C-H}$  stretching vibrations that are only present in

mono-substituted acetylenes.<sup>24</sup> Disubstituted acetylene compounds are more appropriate references for comparison and here the differences are more drastic. For example, the  $\nu(\text{CC})$  of compound **20** is  $1998\text{ cm}^{-1}$  which is  $178\text{ cm}^{-1}$  lower in energy than that of methyl(trimethylsilyl)acetylene. This large difference could be due to a strong back donation of electron density from the metal to an acetylide  $\pi^*$ -orbital.

As part of this research, the alkynylated iron phosphoranimide cluster  $[\text{Fe}(\text{CCPh})(\text{NPEt}_3)]_4$  (**26**) was prepared, using a transmetalation procedure similar to that reported by Dehnicke, et al. In the event, the compound was isolated in 70 % yield (Eqn. 2.2), by trituration into hexanes.



### Eqn. 2.2

Single crystals of **26** were grown by cooling a concentrated solution in THF to  $-35\text{ }^\circ\text{C}$ . The X-ray crystal structure of **26** is shown in Figure 2.2. Crystal, data collection, and refinement parameters for **26** are tabulated in the experimental section. Selected bond lengths and angles are given in Table 2.1.

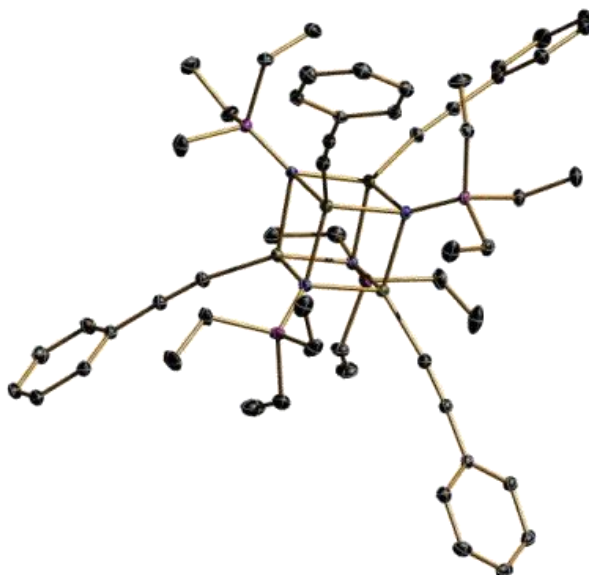


Figure 2.2: ORTEP diagram of  $[\text{Fe}(\text{CCPh})(\text{NPEt}_3)]_4$  (**26**). Thermal ellipsoids are shown at 30 % probability. Hydrogen atoms have been omitted for clarity.

As is observed in the iron clusters **20** and **21**, the  $\text{Fe}_4\text{N}_4$  heterocubane core in **26** is distorted from ideal geometry, with N–Fe–N bond angles around each iron centre ranging from  $92.18(5)^\circ$  to  $95.42(5)^\circ$ , similar to the Jahn-Teller distortions previously described. The Fe–C bond in **26** is 200.61(20) pm, slightly longer than that observed in **1** (199.20(11) pm). This observation is in accord with trimethylsilylacetylide being a stronger  $\sigma$ -donor than phenylacetylide.

Lichtenburger, et al., have shown that the Fe–C bond length in electron rich  $\eta^1$ -acetylide complexes is more indicative of the strength of the metal-acetylide  $\sigma$ -bond than the presence of significant  $\pi$ -type interaction(s).<sup>24</sup> Complex **26** has an average Fe–N bond length of 211.51(12) pm, notably longer than the average Fe–N bond length in **12** (207.7 (6) pm).<sup>18</sup> Perhaps this is because the iron centres in **26** are more electrophilic than those in halide-capped **12**, due to the superior  $\pi$ -

acceptor character of the phenylacetylide ligand. The length of the C–C triple bond in **26** is 121.52 (23) pm which is longer than that in **1** (119.7(1) pm). It is tempting to speculate about  $\pi$ -type metal-acetylide bonding interactions here, but it has been well established that structural data is of limited value in assessing  $\pi$ -bonding character in late metal-acetylide complexes. This is because of the relative insensitivity of the C–C bond length to small changes in population of the  $\pi$  or  $\pi^*$ -orbitals.<sup>25</sup> Photoemission spectroscopy, in combination with DFT computations, might tease apart the  $\sigma$ - and  $\pi$ - type bonding interactions present in this series.

Table 2.1: Selected bond lengths and bond angles for [Fe(CCPPh)(NPEt<sub>3</sub>)<sub>4</sub>] (**26**).<sup>ii</sup>

Interatomic distances (pm)				Bond angles (°)		
Fe••Fe	Fe–C	Fe–N	P–N	Fe–C–C	N–Fe–N	Fe–N–Fe
284.50(4)	200.61(20)	211.51(15)	158.73(13)	170.66(16)	94.11(5)	85.82(5)

### 2.1.1 Catalytic alkyne hydrogenation using [Fe(CCPPh)(NPEt<sub>3</sub>)<sub>4</sub>]

Preliminary results establish that **26** is a precatalyst for the hydrogenation of alkynes and alkenes. For example, stirring a toluene solution of diphenylacetylene and 5 mol % **26**, under 34 atm H<sub>2</sub>, affords quantitative conversion to diphenylethane in 16 hours. The use of homogeneous iron complexes as catalysts

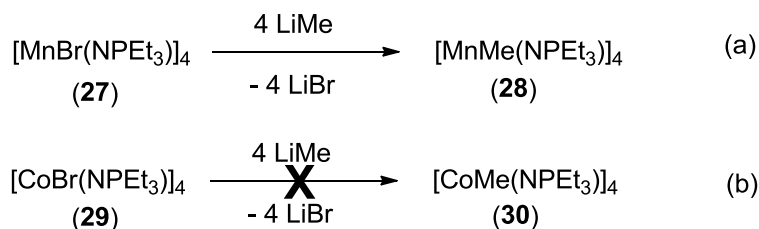
<sup>ii</sup> The bond lengths and angles reported in crystallography tables are averaged values.

for the hydrogenation of unsaturated hydrocarbons is currently under intense study due to the “green” credentials and low cost of iron.<sup>26</sup> Further investigation of the catalytic activity of **26** was abandoned in favor of studies on the cobalt cluster  $[\text{CoMe}(\text{NPEt}_3)_4]$ , which was discovered around the same time. The latter cluster is better suited for reductive catalysis. Metal-alkynyl bonds are stronger than metal-alkyl bonds, and are therefore slower to undergo hydrogenolysis (scission of a bond by molecular hydrogen) under mild conditions. The cobalt(II) centres in  $[\text{CoMe}(\text{NPEt}_3)_4]$  are each capped by a small alkyl substituent (methyl), so that a facile mechanism for precatalyst activation is built into the molecular architectures: late metal-alkyl bonds readily undergo irreversible hydrogenolysis yielding highly-reactive, coordinatively unsaturated cobalt-hydride centres.

## *2.2 Alkyl-capped cobalt phosphoranimide precatalyst complexes*

### *2.2.1 Synthesis and characterization of $[\text{CoMe}(\text{NPEt}_3)_4]$*

Dehnicke and co-workers successfully prepared a series of alkynyl substituted late metal phosphoranimide clusters, but their attempts to prepare alkyl substituted late metal phosphoranimide clusters were unsuccessful. When applied to the analogous manganese phosphoranimide clusters, their transmetallation procedures yield alkyl substituted complexes (Scheme **2.1**).

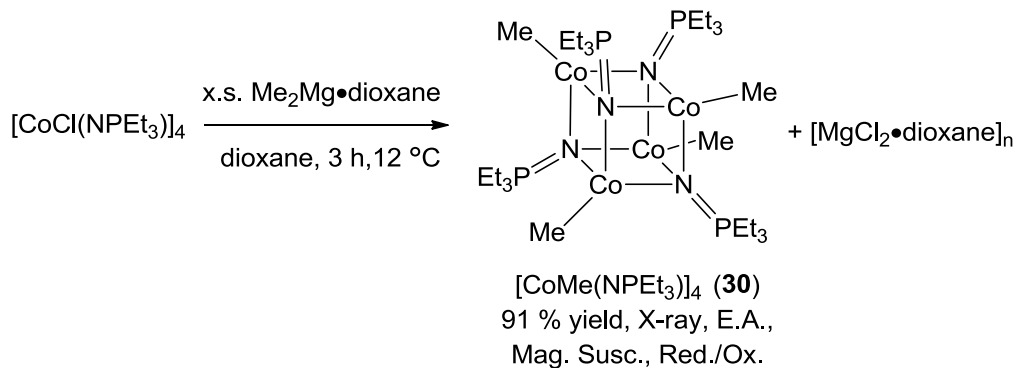


Scheme 2.1

Compared to any of the alkynylated clusters, the reported methylated manganese complex is less thermodynamically stable; metal-alkynyl ( $\text{M-C}_{\text{sp}}$ ) bonds are notably stronger than metal-alkyl bonds ( $\text{M-C}_{\text{sp}^3}$ ), and transition metal-carbon bond strengths decrease from left to right in a series ( $\text{Mn-C} > \text{Fe-C} > \text{Co-C}$ ). Trends in metal-carbon bond strengths can be rationalized in a number of ways.<sup>27</sup> The most useful approach, where *both* the transition metal and the hydrocarbyl fragment are variable, is by considering valence electron repulsions:  $\text{M-C}$  bonds are destabilized by the electron-electron repulsions that occur between the hydrocarbyl substituents and the metal valence orbitals. On the hydrocarbon side of the  $\text{M-C}$  bond, the alpha carbon of a methyl ligand has three filled valences (three bonds to hydrogen) that repel the valence electrons on the metal, while the alpha carbon of an alkynyl ligand has only one, and it is rigidly distal to the metal centre and remains unengaged. Thus, the metal-alkyl bond has more destabilizing valence electron repulsive forces and is weaker than the metal-alkynyl bond. On the metal side of the  $\text{M-C}$  bond, manganese has two fewer d-electrons than cobalt so the electron repulsion experienced by the earlier metal is attenuated compared to the later metal. Metal alkyl bonding becomes inherently weaker as the electron

count on the metal increases. Provided the metals are in the same oxidation state, Mn–C bonds are stronger than Co–C bonds.

Although previous attempts to prepare alkyl substituted late-metal phosphoranimide complexes were unsuccessful, these clusters are accessible in principle. We propose that alkylation with methyl lithium fails because the reaction equilibrium does not favor the formation of the methylated complex enough to isolate it. A procedure for the synthesis of the tetramethyl-substituted cobalt phosphoranimide cluster  $[\text{CoMe}(\text{NPEt}_3)_4]$  (**30**) had to be developed, modifying the transmetallation procedure employed by Dehnicke and co-workers. Addition of excess methyl lithium or methyl magnesium bromide to **11** in toluene or THF appears to result in a reaction, with a notable change in the color of the reaction solution. However, attempts to isolate a product only yielded **11**, presumably because it is the least soluble entity in the equilibrium. However, treatment of **11** with excess dimethylmagnesium in dioxane solvent gives analytically pure **30** in 91 % yield, after isolation by trituration with hexanes and purification by recrystallization (Eqn. **2.3**). This synthesis controls the equilibrium in the transmetallation reaction – 1,4-dioxane forms an insoluble coordination complex by chelation with the magnesium halide salt, thus removing it from solution as it forms.<sup>28</sup> The dialkyl magnesium reagent is also a more aggressive transmetallating reagent and minimizes the quantity of magnesium salts formed during the alkylation.



Eqn. 2.3

Table 2.2 summarizes the principle infrared vibrational frequencies of **30** and some related clusters for comparative purposes. In accord with the infrared activity of other late-metal phosphoranimide heterocubanes, **28** displays a single absorption for  $\nu_{\text{sym}}(\text{M}-\text{N})$  in the cubane framework, a single absorption for the exocyclic  $\nu_{\text{sym}}(\text{M}-\text{X})$ , as well as one absorption for the  $\nu_{\text{sym}}(\text{N}-\text{P})$  of the phosphoranimide ligand, in the IR/FIR spectra. This is due to the high symmetry of the complex ( $T_d$ ), which, according to selection rules, allows for triply degenerate vibrations only.<sup>29</sup> The solution IR data are therefore in agreement with the heterocubane-type molecular structure determined by single-crystal X-ray diffraction, as discussed below.

Table 2.2: Principle IR and FIR absorbances and assignments from solution phase analyses of [CoMe(NPEt<sub>3</sub>)<sub>4</sub>] and some related clusters.

Entry	Complex	$\nu(\text{P-N})$ $\text{cm}^{-1}$	$\nu(\text{M-N})$ $\text{cm}^{-1}$	$\nu(\text{Co-X})$ $\text{cm}^{-1}$	Reference
1	[CoMe(NPEt <sub>3</sub> ) <sub>4</sub> ] ( <b>30</b> )	1066	487	463	Chapter 6
2	[CoBr(NPEt <sub>3</sub> ) <sub>4</sub> ] ( <b>29</b> )	1045	494	221	16
3	[Co(CCTMS)(NPEt <sub>3</sub> ) <sub>4</sub> ] ( <b>31</b> )	1089	492	532	16
4	[MnMe(NPEt <sub>3</sub> ) <sub>4</sub> ] ( <b>28</b> )	1078	482	366	16
5	[MnBr(NPEt <sub>3</sub> ) <sub>4</sub> ] ( <b>27</b> )	1051	490	217	16

As evident from Table 2.2, absorptions arising from the N–P moiety are affected by the nature of the exocyclic functionality in this series of heterocubane complexes. The substitution of methyl for halide at cobalt leads to an increase in the energy of the N–P fundamental by 21  $\text{cm}^{-1}$  (Entry 1 vs. 2). A similar substitution for an alkynyl group increases the energy of the P–N fundamental by 44  $\text{cm}^{-1}$ . Since  $\nu(\text{N-P})$  can be used as a probe for the strength of the N–P bond of the phosphoranimido ligand, these shifts are indicative of a strengthening of the N–P bonding interaction. A similar trend exists between manganese phosphoranimide clusters **27** and **28** (Entry 4 vs. 5). Likewise, comparisons between the energies of the Co–N fundamentals of **30**, [Co(C≡CTMS)(NPEt<sub>3</sub>)<sub>4</sub>] (**31**) and [CoBr(NPEt<sub>3</sub>)<sub>4</sub>] (**29**) suggest that substitution of a halide for a hydrocarbyl ligand results in a weakening of the Co–N bonding interaction (Entries 1,3 vs. 2). This trend is also mirrored in the manganese series (Entries 2, 4).

X-ray quality crystals of **30** were first prepared by slow precipitation from dioxane; the structure of the complex is shown in Figure 2.3. Crystal, data

collection, and refinement parameters are provided in the experimental section.

Table 2.3 summarizes the relevant average bond lengths and angles for **30**.

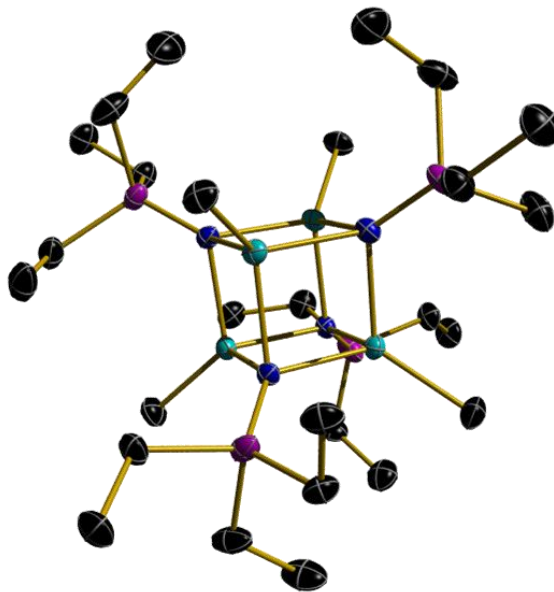


Figure 2.3: ORTEP diagram of  $[\text{CoMe}(\text{NPET}_3)_4]$  (**30**). Thermal ellipsoids are shown at 30 % probability. Hydrogen atoms have been omitted for clarity.

The crystal structure confirms that the  $\text{Co}_4\text{N}_4$  core of the halide substituted precursor **11** is not altered by the replacement of the exocyclic chlorine atoms with methyl functionalities. The Co–N–Co and N–Co–N bond angles that make up the cores of these clusters are, within experimental error, identical (86.1(1) and 93.9(1) pm vs. 86.0(2) and 93.1(3) pm for **30** and **11** respectively). The average P–N bond length for **30** is 158.4(3) pm, again identical within error to that of **11** (159.2(6) pm). Thus the diffraction data does not support the putative trend observed in the infrared spectra correlating the identity of the exocyclic functionality and the strength of the P–N bond. More likely is that the changes in

P–N bond lengths are too subtle to be accurately measured by X-ray diffraction, making vibrational spectroscopy better suited to revealing such small changes in bond strengths.

The average Co–N bond length in **30** is 207.3(2) pm, approximately three pm longer than the average Co–N bond lengths in both **29** and **31**. This data (and the IR data discussed above) suggest that the strength of the Co–N bond is inversely related to the sigma-bonding ability of the exo-cyclic ligand. The methyl ligand is the strongest sigma-donor (strongest Lewis base) **30**, the halide ligand is the weakest sigma-donor (weakest base), and the  $\sigma$ -alkynyl ligand is intermediate. This effect is similar to the trans-influence commonly observed in octahedral and square planar complexes,<sup>30</sup> however the ‘trans’ label does not apply well to the tetrahedral disposition of the ligands at cobalt.

The average Co–C bond length in **30** is 202.9(5) pm, within the normal range for Co(II)-alkyl single bonds.<sup>31</sup> The Co–C bond length in **31** is 195.3(6) pm, significantly shorter, reflecting the 7 pm difference in covalent radii between  $sp^3$ - and  $sp$ -hybridized carbon.<sup>32</sup>

Table 2.3: Selected bond lengths and bond angles for [CoMe(NPEt<sub>3</sub>)<sub>4</sub>].

Interatomic distances (pm)				Bond angles (°)	
Co••Co	Co–C	Co–N	P–N	N–Co–N	Co–N–Co
285.7(5)	202.9(5)	207.3(2)	158.4(3)	93.9(1)	86.1(1)

### 2.2.2 Magnetic and Electrochemical Studies on $[\text{CoMe}(\text{NPEt}_3)]_4$

Magnetic measurements on **30** provide insight into the electronic structure of the cluster. Solution magnetic susceptibility experiments (Evan's method)<sup>33</sup> establish that **30** is a 4.01-electron paramagnet ( $\mu_{\text{eff}} = 4.90 \mu_{\text{Bo}}$ ) at room temperature: one unpaired electron per cobalt atom. Magnetic measurements on pseudotetrahedral cobalt(II) complexes typically reflect three unpaired electrons per cobalt centre,<sup>34</sup> as the weak splitting energy of a tetrahedral ligand field favours high-spin configurations (see diagram [A] in Figure 2.4). The low magnetic-moment measured for **30** could be due to a number of factors. One explanation is that low-spin configurations for the metals in **30** are thermodynamically favourable in the coordination environment imposed by the cluster's ligand set. Diagram [B] illustrates how the d-orbitals are affected by distortion of the ligand sphere away from  $T_d$  symmetry. As the bond angles between the metal and the basal positions of the trigonal-pyramid become increasingly acute, the energy of the  $d_{z^2}$  orbital lowers due to decreasing angular overlap between the ligand donors and the  $d_{z^2}$  orbital. In cases where the ligand-field splitting becomes unusually large – which will be the case with a strongly  $\sigma$ -donating ligand set held in distorted-tetrahedral coordination by geometric restraints – a low-spin configuration is obtained. The monomeric cobalt(II) complex  $[\text{Co}(\text{PhB}(\text{P}^{\text{Ph}_2})_3)(\text{OSiPh}_3)]$  (**32**) (where  $\text{PhB}(\text{P}^{\text{Ph}_2})_3$  is the singly anionic phenyl tris-terphenylphosphinoborate ligand) exemplifies this effect; the constraints of the tripodal ligand result in an average P–Co–P bond angle of  $90.6^\circ$ .<sup>35</sup> The ligand-sets coordinating the cobalt centres of **30** fit the

description above well, as the cubane structure results in N–Co–N bond angles that are close to  $90^\circ$  ( $93.9(1)^\circ$ )– significantly more acute than the ideal tetrahedral angles of  $109.5^\circ$ , and potentially distorted enough to favour a low-spin configuration.

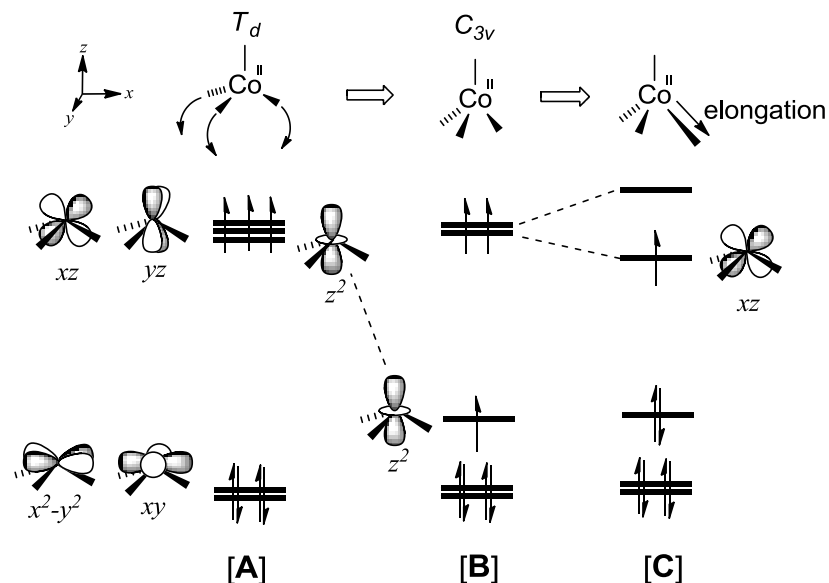


Figure 2.4: Qualitative d-orbital correlation diagram summarizing the electronic effects associated with distorting a tetrahedral-ligand field around Co(II).<sup>34</sup>

One issue with this rationalization of the low magnetic-moment measured for **30** is that low-spin configurations for the  $d^7$  cobalt atoms would result in single-electron occupation of doubly-degenerate orbitals at each metal centre. Such an arrangement would be unstable towards geometric distortions that remove the orbital degeneracies (diagram [C]); the X-ray diffraction data for **30** do not reflect such distortions. Moreover, the reactivity of **30** is not representative of a cluster with empty low-lying orbitals (see section 2.4). The energy levels of the metal d-

orbitals in **30** are best represented by diagram [B], which is reproduced with more structural details in Figure 2.5. Extended Huckel calculations on the hypothetical cluster  $[\text{MBr}(\text{NPH}_3)]_4$  are in accord with this qualitative splitting diagram.<sup>3</sup>

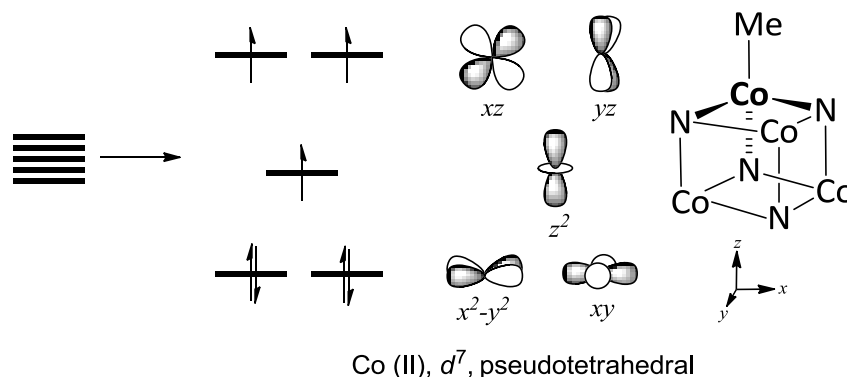


Figure 2.5: Energy splitting of the cobalt d-orbitals in the local trigonal-pyramidal ligand field at one corner of the cube.<sup>3</sup>

A more plausible explanation for the low magnetic-moment measured for **30** is that the total spin-moment for the cluster is reduced by anti-ferromagnetic coupling between neighbouring cobalt atoms. The measured average  $\text{Co}\cdots\text{Co}$  interatomic distance of 285.7(5) pm in the solid state structure **30** limit the potential for direct Co–Co bonding interactions. Computational results provided by collaborators suggest the electronic interactions between metal centres are facilitated by the single-atom nitrogen bridges of the phosphoranimide ligands.<sup>36</sup> While specific values for the anti-ferromagnetic coupling constants have not yet been established, the experimentally determined magnetic moment of **30** can be reproduced *in-silico*.

Cyclic voltammetry experiments on **30**, also performed by collaborators<sup>37</sup> provide insight into the redox activity of the cluster. Two reversible one-electron oxidation events are observed for **30** in both difluorobenzene and tetrahydrofuran (Figure **2.6a**). The potentials for these redox events are tabulated below. The first oxidation (-0.894 V) is attributed to the transition  $4\text{Co}^{\text{II}}/3\text{Co}^{\text{II}}1\text{Co}^{\text{III}}$ . The reversibility of the process implies the redox event is associated with only minor structural reorganization in the cluster core.<sup>38</sup> X-ray diffraction studies on the cationic complex  $[\text{CoMe}(\text{NPEt}_3)_4]\text{PF}_6$  confirm this observation (see Section 2.3). Based on the structural data, the oxidation of  $[\text{CoMe}(\text{NPEt}_3)_4]$  to  $[\text{CoMe}(\text{NPEt}_3)_4]^+$  does not result in any bond formation/cleavage events but does result in shorter Co–N bond lengths in the  $\text{Co}_4\text{N}_4$ -core. The strengthening of the Co–N bonding interactions implies the electron is removed from an orbital of anti-bonding character. This inference is in accord with computational results that suggest the HOMO of **30** is high in energy, and delocalized around the  $\text{Co}_4\text{N}_4$  core (see Figure **2.15b**, pg. 61). Similar structural changes have been observed in the reversible oxidation of other transition metal systems. For example, X-ray diffraction data for the familiar ferrocenium/ferrocene redox congeners show the oxidation of  $[\text{FeCp}_2]$  to  $[\text{FeCp}_2]^+$  results in a 5.6 pm decrease in the Fe– $\text{Cp}_{\text{centroid}}$  distance while the sandwich geometry around the metal centre is maintained.<sup>38</sup>

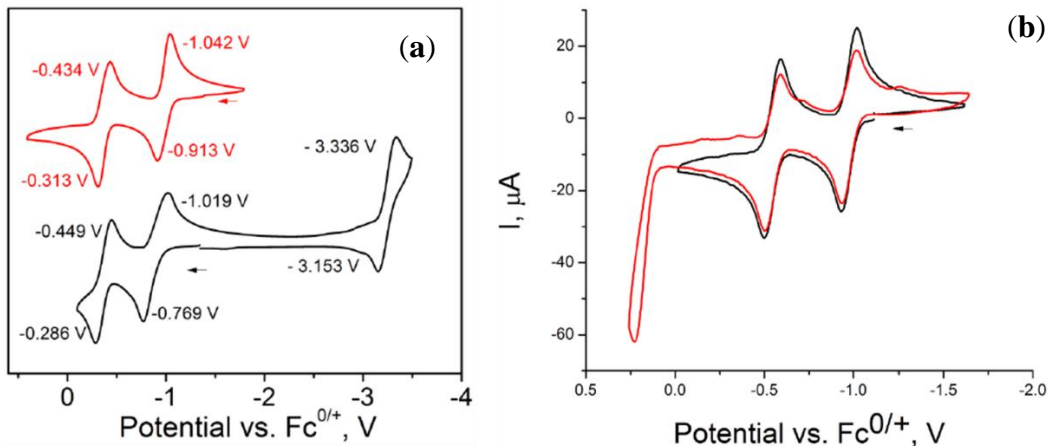


Figure 2.6. (a) Cyclic voltammogram of  $[\text{CoMe}(\text{NPEt}_3)_4]$  (**30**) in difluorobenzene (red) and tetrahydrofuran (black) with  $E_{1/2}$  values versus ferrocene, scan rate = 100 mV/s. (b) Cyclic voltammogram of  $[\text{CoMe}(\text{NPEt}_3)_4]$  in tetrahydrofuran displaying the irreversible oxidation beyond  $E_2$ .

The second oxidation event is associated with the transition

$3\text{Co}^{\text{II}}1\text{Co}^{\text{III}}/2\text{Co}^{\text{II}}2\text{Co}^{\text{III}}$ . The dicationic  $[\text{CoMe}(\text{NPEt}_3)_4]^{2+}$  cluster has not been prepared and isolated, but the cyclic voltammetry data suggests that it is stable and should be accessible by treating **30** with two equivalents of an appropriate chemical oxidant. The choice of oxidant for the preparation of  $[\text{CoMe}(\text{NPEt}_3)_4]^{2+}$  requires care as scans to more positive potentials indicate the presence of a third oxidation event that is irreversible (Figure 2.6b). The potential of the second oxidation of **30** is -0.3675 V (table 2.4) while the irreversible oxidation occurs at higher potential than the  $[\text{FeCp}_2]^{0/+}$  couple. Thus the ferrocenium cation is an ideal chemical oxidation reagent for preparation of  $[\text{CoMe}(\text{NPEt}_3)_4]^{2+}$ .

Table 2.4: Redox potentials (V) for the three redox events observed for [CoMe(NPEt<sub>3</sub>)<sub>4</sub>] in difluorobenzene and tetrahydrofuran.  $E_1$  and  $E_2$  are the first and second oxidations of the neutral complex respectively.  $E_3$  is the reduction of the neutral complex observed in THF only.

<i>Solvent</i>	$E_1$	$E_2$	$E_3$	$\Delta E_{1,2}$
DFB	-0.9775	-0.3735	–	0.6040
THF	-0.8940	-0.3675	-3.2445	0.5265

The occurrence of an electrochemically irreversible process implies a very large activation barrier to electron transfer, and irreversible processes are often tied to the disassembly of molecular frameworks.<sup>38</sup> One possibility is that the oxidation results in the dissociation of the tetramer into two dimers. A similar event is observed in the irreversible oxidation of the dirhenium(III) complex [Re<sub>2</sub>(μ-Cl)<sub>2</sub>Cl<sub>4</sub>(PMe<sub>3</sub>)<sub>4</sub>] (**32**).<sup>39</sup> Structural characterization confirms that the oxidation of the dimer results in irreversible dissociation to form the Re<sup>V</sup> cation [ReCl<sub>4</sub>(PMe<sub>3</sub>)<sub>2</sub>]<sup>+</sup> (**33**) (Figure 2.7). Interestingly, the single electron reduction of **32** is also irreversible, forming the anion [Re<sub>2</sub>(μ-Cl)<sub>3</sub>Cl<sub>2</sub>(PMe<sub>3</sub>)<sub>4</sub>]<sup>-</sup> (**34**).<sup>39</sup>

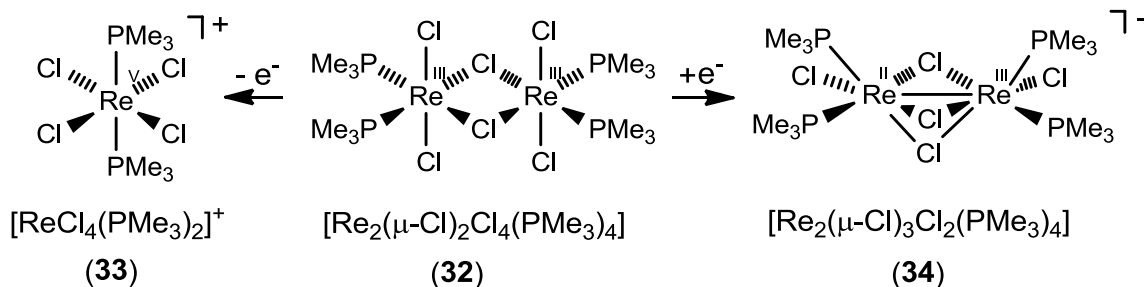
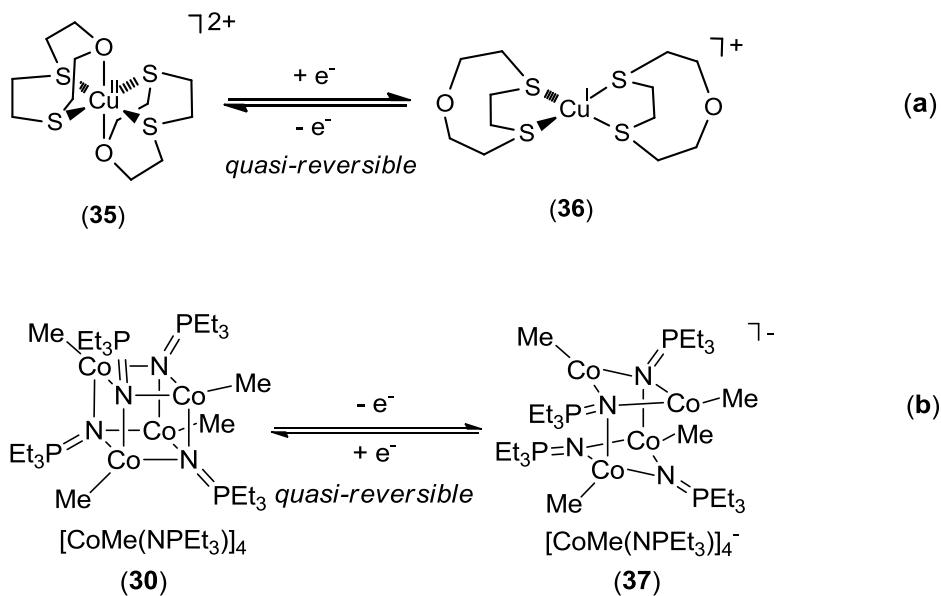


Figure 2.7: Irreversible oxidation/reduction of [Re<sub>2</sub>(μ-Cl)<sub>2</sub>Cl<sub>4</sub>(PMe<sub>3</sub>)<sub>4</sub>] (**32**).<sup>39</sup>

Quasi-reversible electrochemical processes are associated with significant structural reorganizations of molecular frameworks that do not result in fragmentation.<sup>38</sup> The extent of structural reorganization associated with a quasi-reversible event can be qualitatively correlated to the peak-to-peak separation observed in the CV. The larger the deviation in peak-to-peak separation from the theoretical value of 59 mV (for a reversible one electron process) the more significant the associated structural reorganization.<sup>38</sup> A single quasi-reversible reduction event is observed in scans of **30** in THF to very negative potentials (Figure **2.6a**). The reductive event is associated with the transition  $4\text{Co}^{\text{II}}/3\text{Co}^{\text{II}}1\text{Co}^{\text{I}}$  and has a peak-to-peak separation of 183 mV at a scan rate of 100 mV/s. A similar quasi-reversible peak-to-peak separation (114 mV at a scan rate of 100 mV/s in acetonitrile) is observed in the CV of the redox active  $\text{Cu}^{\text{III/I}}$  complex illustrated in Scheme **2.2a**.<sup>40</sup> The hetero-chelated complex  $[\text{CuL}_2]^{2+}$  (**35**) ( $\text{L} = 1,4,7\text{-oxadithionane}$ ) possesses an octahedral geometry with four neutral sulfur- and two neutral oxygen-ligands coordinating the metal centre. Reduction of the complex results in a shift to tetrahedral coordination around the  $\text{Cu}(\text{I})$  centre with the loss of the covalent  $\text{Cu-O}$  interactions (**36**). The quasi-reversible reduction of **30** could be associated with a similar loss of metal/neutral-donor interactions with one, or more, of the phosphoranimide ligands slipping from  $\mu_3$  to  $\mu_2$  coordination (Scheme **2.2b**).



### Scheme 2.2

In order to understand the reactivity of **30** it is important to know its dimensionality in solution: is the complex a tetramer in solution (like it is in the solid state) or does it dissociate to form dimers, or even monomers? Cyclic voltammetry experiments provide evidence that **30** remains a tetramer in solution. The peak current values from the anodic scan of a 1:1:1 solution of **30**, cobaltocene, and ferrocene are within error of each other (Figure 2.8). Knowing that each process is a single-electron oxidation, **30** must be tetrameric in solution; dissociation into a dimer would yield a 2:1 ratio of  $[\text{CoMe}(\text{NPEt}_3)]_2$  to  $\text{CoCp}_2/\text{FeCp}_2$  and therefore a 2:1 ratio of the corresponding peak current values. The same argument applies for the one electron oxidation of  $[\text{CoMe}(\text{NPEt}_3)]_4^+$  to  $[\text{CoMe}(\text{NPEt}_3)]_4^{2+}$  therefore the cationic cluster must also remain a tetramer in solution. Moreover, as discussed above, the fracture of a tetrameric cluster into

two dimers is a major structure change that would likely be irreversible on the CV-timescale.

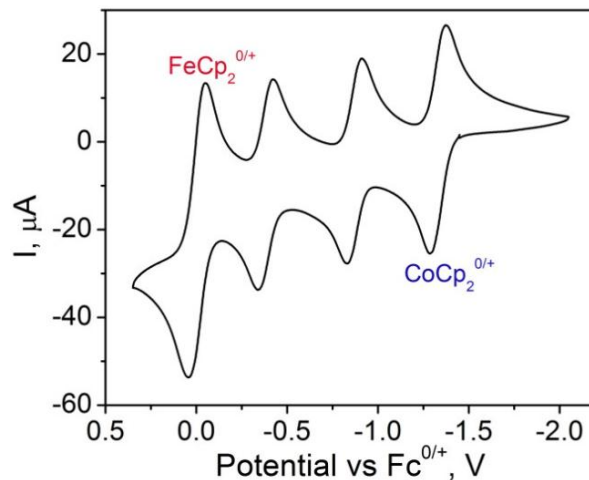
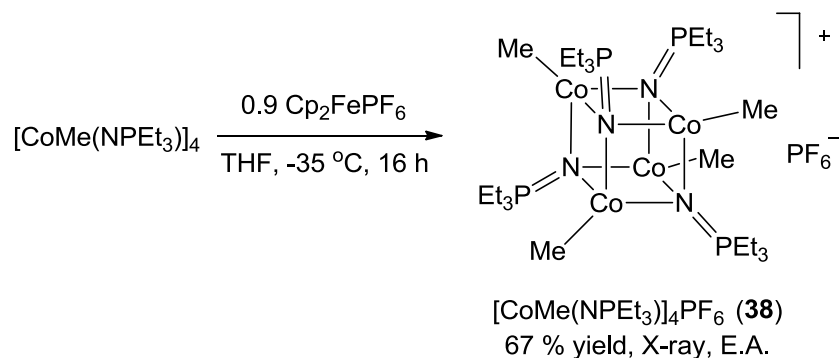


Figure 2.8 Cyclic voltammogram of  $[\text{CoMe}(\text{NPEt}_3)_4]$  (**30**) in the presence of equimolar amounts of cobaltocene and ferrocene in tetrahydrofuran.

### 2.3 Mixed-valence alkyl-capped metal phosphoranimide complexes

As predicted by the electrochemical data, the cationic cluster  $[\text{CoMe}(\text{NPEt}_3)_4]^+$  is a stable species. Treatment of **30** with an equimolar amount of  $\text{Cp}_2\text{FePF}_6$  in THF yields the mixed-valence cluster  $[\text{CoMe}(\text{NPEt}_3)_4]\text{PF}_6$  (**38**) in good yield (Eqn. 2.4). The ferrocenium cation is a mild one-electron oxidant usually regarded as an outer-sphere electron transfer reagent<sup>41</sup>. Outer-sphere electron transfer occurs while leaving the inner coordination sphere of both the oxidant and the reductant intact in the transition state.<sup>42</sup>



Eqn. 2.4

The reaction produces a stoichiometric quantity of ferrocene which can be removed by washing with a non-polar solvent or, if necessary, by sublimation. Using toluene as the reaction medium and adding a slight excess of **30** ensures **38** can be isolated by simple filtration. The reaction is likely heterogeneous due to the limited solubility of  $\text{Cp}_2\text{FePF}_6$  in toluene, but the rate is sufficient for the reaction to go to completion overnight.

Table 2.5 summarizes the principle infrared vibrational frequencies noted for **38**. In accord with the infrared activity of other late metal-phosphoranimide heterocubanes, the infrared spectra of **38** display a single absorption corresponding to each of the principle functionalities:  $\nu(\text{M-N})$ ,  $\nu(\text{M-X})$  and  $\nu(\text{N-P})$ . The oxidation of **30** to **38** appears to have little effect on the P-N bond order, as  $\nu(\text{N-P})$  for the two clusters are similar ( $1066$  and  $1059 \text{ cm}^{-1}$  respectively). In contrast, the oxidation appears to substantially increase the strength of the Co-N bonding interactions;  $\nu(\text{Co-N})$  is  $70 \text{ cm}^{-1}$  higher for **38** than for **30**. Comparisons of the Co-N bond lengths from X-ray diffraction experiments also support this

conclusion. The  $\nu(\text{Co-C})$  for **38** is  $33 \text{ cm}^{-1}$  higher in energy than that of **30**, suggesting the Co-Me bond order also increases during the oxidation. This conclusion is also supported by structural data and can be rationalized by considering the effect of valence repulsions on M-C bond strengths discussed in section 2.2.1: removing an electron from the metal centres of **38** decreases the repulsive force between the metal valence electrons and the valence electrons of the  $\text{CH}_3$  ligand, and thus the oxidized cluster forms stronger Co-Me bonds than the neutral cluster. Valence electron repulsion can also be used to rationalize the considerable difference in the  $\nu(\text{Co-N})$  values observed for **30** and **38** ( $487$  and  $557 \text{ cm}^{-1}$ ) respectively. This increase in Co-N bond order is also reflected in the structural data.

Table 2.5: Principle IR and FIR absorbances and assignments for  $[\text{CoMe}(\text{NPET}_3)_4\text{PF}_6]$  (**38**).

Absorbance ( $\text{cm}^{-1}$ )	Assignment
496	$\nu(\text{Co-C})$
557	$\nu(\text{Co-N})$
1059	$\nu(\text{P-N})$

X-Ray quality single-crystals were obtained by vapour-diffusion of pentane into a solution of **38** in THF; the crystal structure is shown below.

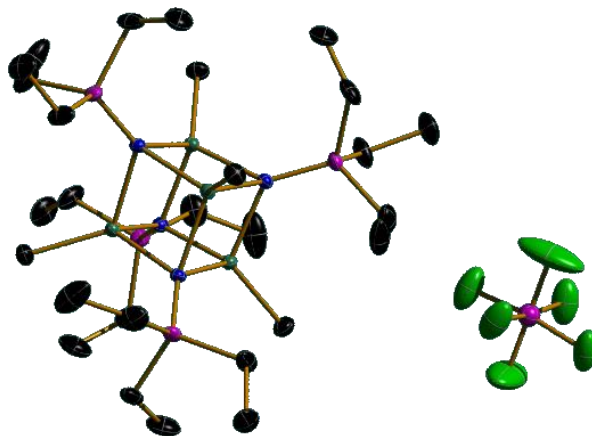


Figure 2.9: ORTEP diagram of  $[\text{CoMe}(\text{NPEt}_3)]_4\text{PF}_6$  (**38**). Thermal ellipsoids are shown at 30 % probability. Hydrogen atoms have been omitted for clarity.

Table 2.6 contains relevant average bond lengths and angles for **38**. While the  $\text{Co}_4\text{N}_4$  core remains intact on oxidation of **30** to **38**, the geometry of the heterocubane framework is significantly altered. The loss of an electron results in more acute Co–N–Co bond angles ( $84.3(9)$  vs.  $86.1(1)^\circ$ ) and more obtuse N–Co–N bond angles ( $95.6(9)$  vs.  $93.9(1)^\circ$ ). The Co–N bond lengths in **38** are 4.8 pm shorter than those of **30** ( $202.5(3)$  and  $207.3(2)$  respectively). The shorter Co–N bonds, and more acute Co–N–C bond angles result in notably reduced Co•••Co interatomic distances in **38** (13.5 pm shorter than those in **30**). The Co–C bonds in **38** are also shorter than those of **30** ( $199.4(7)$  vs.  $202.9(5)$  pm respectively). Thus,

the overall structural change associated with the one electron oxidation is a contraction of the cluster, and a distortion away from ideal cubic geometry.

Table 2.6: Selected bond lengths and bond angles for [CoMe(NPEt<sub>3</sub>)<sub>4</sub>PF<sub>6</sub> (**38**).

Interatomic distances (pm)				Bond angles (°)	
Co••Co	Co–C	Co–N	P–N	N–Co–N	Co–N–Co
272.2(7)	199.4(7)	202.5(3)	159.5(3)	95.6(9)	84.3(9)

The most striking feature of the crystal structure of the mixed-valence cation [CoMe(NPEt<sub>3</sub>)<sub>4</sub>]<sup>+</sup> is the symmetry of the cluster: removing an electron does not result in three discrete cobalt(II) centres and one Co(III) centre, all of the cobalt centres in **38** are equivalent and best described by a non-integral oxidation state (4 x Co<sup>2.25+</sup>). Robin and Day suggest classifying mixed-valence systems by the strength of the electronic interaction between the oxidized and reduced sites, ranging from essentially zero (class I), to moderate (class II), to very strong electronic coupling (class III).<sup>43</sup> Based on the structural data, **38** is a class III mixed-valence complex: no individual properties of the metals can be distinguished and bonding descriptions should consider the molecular orbitals of the cluster as a whole.<sup>44</sup> Computationally generated descriptions of the bonding in **38** support this classification, as discussed below.

## 2.4 The benefits of mixed-valency: Differences between $[\text{CoMe}(\text{NPEt}_3)]_4$ and $[\text{CoMe}(\text{NPEt}_3)]_4\text{PF}_6$

After a passing glance at the crystal structures of the homovalent cluster **30** and mixed-valent cluster **38** it is tempting to speculate that the two clusters will have similar reactivity. This is not the case. The mixed-valent cluster behaves as a coordinatively unsaturated complex reacting under mild conditions. The homovalent cluster is significantly less reactive. This section aims to highlight and explain the different reactivities observed for clusters **30** and **38**.

### 2.4.1 Electron counting and EAN

In order to coordinate hydrogen, a metal centre requires a vacant low-energy orbital. In other words, the metal must be coordinatively unsaturated. The 18-electron rule is used in coordination and organometallic chemistry to determine the degree of coordination saturation at a metal centre.<sup>4</sup> The rule is useful in predicting the reactivity of monomeric transition metal complexes, but its utility does not necessarily extend to metals assembled in clusters. The ‘Effective Atomic Number Rule’ (EAN rule) is a modified version that applies to small clusters.<sup>45</sup> The tenets of the two models are the same: complexes with enough electrons to populate all of the low energy orbitals are said to be coordinatively saturated, and are likely un-reactive; electron deficient complexes that do not fully occupy the low energy orbitals are said to be coordinatively unsaturated, and are more likely to be reactive. The EAN rule also accounts for the presence of metal-

metal bonding interactions, as expressed in Eqn. 2.5, where  $EAN$  is the effective atomic number, as defined by the number of valence electrons in the cluster,  $x$  is the number of metals in the complex, and  $y$  is the number of metal-metal bonds.<sup>iii</sup>

$$EAN = 18x - 2y \quad 2.5$$

When metals in a cluster are supported by bridging ligands – as opposed to metal-metal bonds – the EAN rule can be used to determine the number of metal-metal bonds required to saturate the cluster (Eqn. 2.6).

$$y = \frac{18x - EAN}{2} \quad 2.6$$

The cobalt(II) heterocubane **30** has 60 valence electrons, as accounted for in Figure 2.10. Applying the EAN rule to this cluster suggests that six metal-metal bonds need to be present to saturate the bonding orbitals. The physical manifestation of this calculation is that the saturated cluster is predicted to have one metal-metal bond for each face of the cubane core.

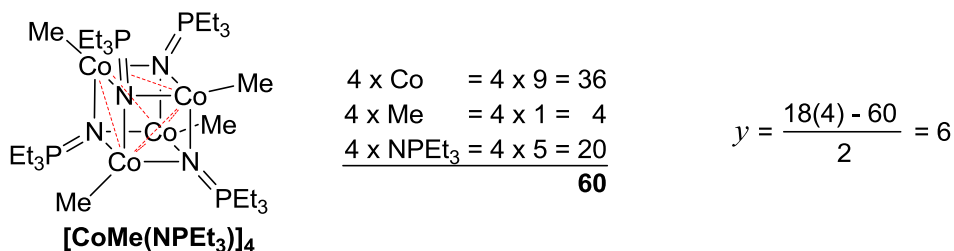


Figure 2.10: Electron counting and the EAN rule for  $[\text{CoMe}(\text{NPEt}_3)]_4$  (**30**).

<sup>iii</sup> When considering only one metal ( $x = 1$ ,  $y = 0$ )  $EAN$  equals 18, reducing to the simple 18-electron rule for monomeric complexes.

Crystallographic and magnetic measurements provide experimental data relevant to the metal-metal bonding present in **30**. The average Co•••Co distance is 285.7(5) pm: well outside the Co–Co single-bond value of 248 pm..<sup>46</sup> At room temperature, the cluster has a magnetic moment of 4.90  $\mu_{\text{B}}$ , considerably lower than the calculated spin-only value.<sup>36</sup> Taken together, these data suggest that there is little, if any, direct metal-metal bonding across the faces of the heterocubane. Yet there is still a significant amount of metal-metal electronic communication, presumably via the single-atom  $\mu_3$ -nitrogen bridges. Unfortunately, these data alone do not provide a definitive assignment of the ‘degree of unsaturation,’ which is the primary goal of the EAN calculation. For this reason, **30** is best described as latently unsaturated; low energy orbitals capable of accepting electron density from exogenous donors exist, but are being placated by pseudo metal-metal bonding interactions across the edges of the cubane.

Applying the EAN rule to **38** is also straightforward. The mixed-valence cluster has 59 valence electrons and is coordinatively unsaturated. Computational models reflect the differences in the electron states of **30** and **38**. DFT calculations (GGA-PBE), validated by accurately reproducing the experimentally determined bond lengths, bond angles, and magnetic characteristics of both clusters, afford quantitative descriptions of the frontier molecular orbitals.<sup>36</sup> The lowest unoccupied molecular orbital (LUMO) for mixed-valence **38** was determined to be 0.36 eV lower in energy than that of homovalent **30**. The LUMO(-1) and LUMO(-2), with orbital energies comparable to the low-lying LUMO of the

cationic complex, are degenerate and singly occupied. In other words, the mixed-valent cluster **38** is much better suited to coordinate a Lewis donor.

#### 2.4.2 Reactivity towards dihydrogen

The descriptions of complexes **38** and **30** as coordinatively unsaturated and latently unsaturated, respectively, are in accord with the observed reactivity toward hydrogen. The cationic cluster **38** visibly reacts with hydrogen at room temperature and lower than atmospheric pressure. Solution UV-Vis spectra of **38** before and after exposure to one atmosphere of hydrogen at room temperature reveal a shift in absorbance characteristics (Figure 2.11). Before hydrogen exposure, a solution of **38** exhibits a broad, nearly featureless absorbance between 620–750 nm (a). After hydrogen exposure, the feature narrows to 600–680 nm and the molecular absorptivity drops. Under the same conditions, UV-Vis spectra of neutral cluster **30** before and after hydrogen addition show no change. However, heating the solution of **30** to 110 °C under 34 atm H<sub>2</sub> does alter the UV-Vis spectrum, with the broad bi-modal absorption feature observed before hydrogen exposure (620–650 nm) flattens out to a weak absorbance around 750 nm (b). Both reactions are associated with changes in color from green to light brown. Presumably, the difference between LUMO energies for **30** and **38** underlies the disparate reactivity towards hydrogen. The LUMO of **38** is more energetically accessible for the  $\sigma_{\text{H}_2} \rightarrow d_{\text{M}}$  electronic interaction associated with H<sub>2</sub> coordination.

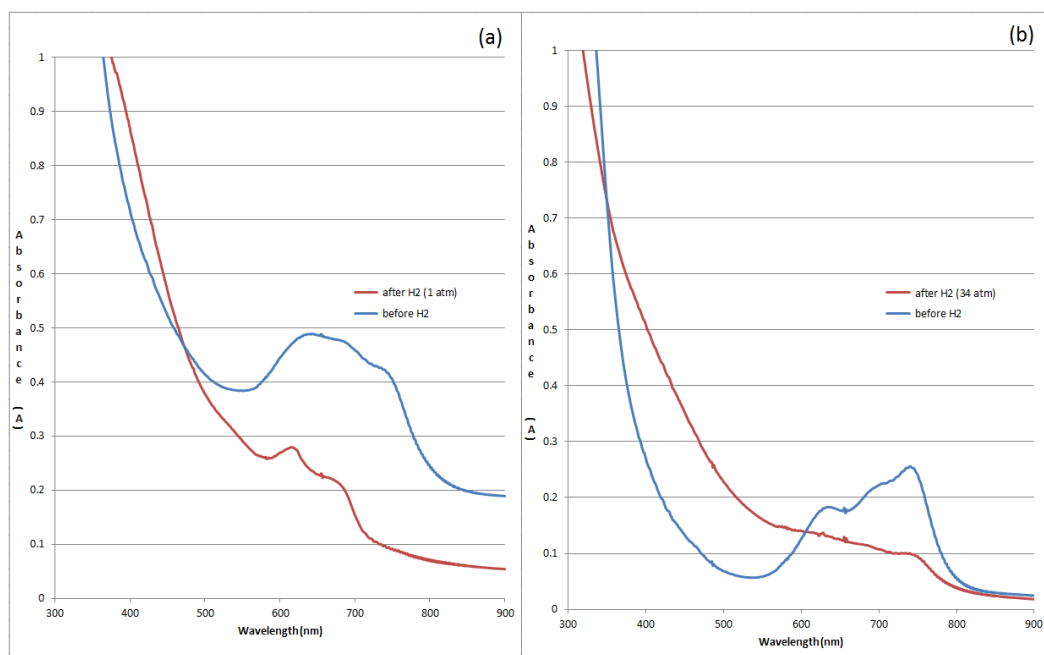


Figure 2.11: Solution UV-Vis of  $[\text{CoMe}(\text{NPEt}_3)_4]\text{PF}_6$  (**38**) and  $[\text{CoMe}(\text{NPEt}_3)_4]$  (**30**) before and after reaction with hydrogen. (a)  $5.0 \times 10^{-2}$  M  $[\text{CoMe}(\text{NPEt}_3)_4]\text{PF}_6$  in THF before and after stirring under one atm of hydrogen for five minutes. (b)  $3.0 \times 10^{-2}$  M  $[\text{CoMe}(\text{NPEt}_3)_4]$  before and after stirring at  $110^\circ\text{C}$  for 30 minutes under 34 atm of hydrogen.

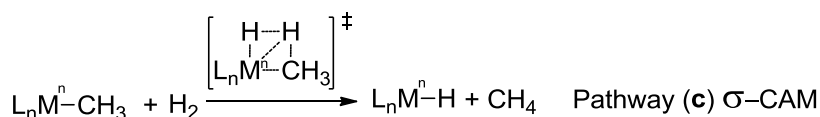
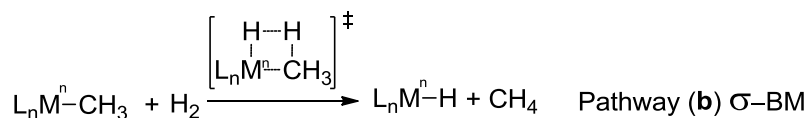
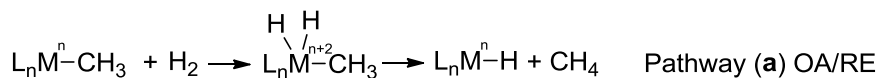
#### 2.4.3 Precatalyst activation mechanism(s)

Each of the cobalt atoms in **30** and **38** is capped by an anionic  $\text{CH}_3$  ligand. We posit that both clusters are activated for reductive catalysis by hydrogenolysis of one or more of the Co–C bonds. The scission of the bond by molecular hydrogen releases methane and forms a new Co–H bond.<sup>iv</sup> While the hydrogenolysis is theoretically reversible, in an open system, the methane will diffuse out of solution, driving any equilibrium in favor of hydride formation. The reaction is

<sup>iv</sup>Preliminary attempts to confirm the presence of Co–H bonds with IR spectroscopy were not successful. The paramagnetic natures of **30** and **38** preclude  $^1\text{H}$  NMR experiments from providing confirmation of cobalt-hydride formation. Current grad students and collaborators are continuing this effort with traditional methods and *in-situ* Raman spectroscopy

also enthalpically favored, as Co–H bonds are considerably stronger than Co–CH<sub>3</sub> bonds;<sup>47</sup> the reverse reaction is thus associated with a higher activation barrier. The molar equivalents of hydrogen involved in cluster activation and the resulting cluster structure(s) are not known. Neutron diffraction studies have revealed many polymetallic clusters with bridging hydride ligands, while polymetallic clusters with terminally bound hydride ligands have yet to be structurally characterized.<sup>48</sup> For this reason it seems likely that the hydrogenolysis of **30/38** yields cobalt phosphoranimide clusters with bridging hydride ligands. On the other hand, bridging across the face of the cubane requires a single hydrogen atom to span more than 285 pm (provided hydrogenolysis does not drastically alter the structural arrangements in **30/38**). Moreover, a  $\mu_2$ -hydride ligand would require high-energy structural reorganizations, with all of the bonds forced into one hemisphere of the metal coordination sphere. One possibility is that the hydrides will be terminally coordinated at very low-temperature, but fluxional under reaction conditions, isomerizing through bridging transition states.

Detailed mechanistic studies on related late metal systems provide insight into how the hydrogenolysis of Co–C bonds in **30/38** may occur. The mechanisms suggested for the vast majority of transition metal-alkyl bond hydrogenolysis reactions fall somewhere between the three simplified mechanisms ( Scheme **2.3**).



### Scheme 2.3

Pathway **(a)** is a two-step oxidative addition/reductive elimination (OA/RE) process where the intermediate dihydride complex has a formal oxidation state two charges higher than the precursor and product complexes. The OA event involves the transfer of electron density from the coordinating species to a vacant metal-based orbital, and the concomitant donation of electron density from the metal back into an antibonding orbital on the coordinating species, provided one is accessible. Electron rich, low valent metals are well suited for such back-bonding interactions. Pathway **(b)** describes a  $\sigma$ -bond metathesis mechanism ( $\sigma$ -BM): a one-step transformation during which the metal oxidation state does not change. The concept of  $\sigma$ -BM stems from the chemistry of high valent  $d^0$  metals for which oxidative addition is impossible.<sup>49</sup> Investigations of the  $\sigma$ -complexes that proceed and follow such four-centre transition states have revealed variations on the  $\sigma$ -BM theme, including adaptations to suit the chemistry of late metals. In late metal systems, filled metal-based orbitals can participate in single step

transformations, with the metal maintaining a constant oxidation state while acting as a cam on which the ligands reorganize. This process has been termed  $\sigma$ -complex assisted metathesis ( $\sigma$ -CAM, pathway (c))<sup>49</sup>.

The mechanistic pathway by which the metathesis occurs depends on the ligand environment and the ability of the metal centre to accommodate the higher oxidation state inherent to the OA/RE mechanism. For example, theoretical studies on the metathesis process  $[\text{Tp}(\text{PH}_3)\text{MH}(\eta^2\text{-H-CH}_3)] \rightarrow [\text{Tp}(\text{PH}_3)\text{MCH}_3(\eta^2\text{-H}_2)]$  ( $\text{M} = \text{Fe, Ru, Os}$ ;  $\text{Tp} = \text{hydrotris(pyrazolyl)borate}$ ) show different mechanisms for each of the metals studied.<sup>50</sup> Metathesis with the iron complex proceeds, without change in metal oxidation state, through a four centred transition state, consistent with the concerted  $\sigma$ -CAM mechanism. For the second row analog ( $\text{M} = \text{Ru}$ ), the metathesis has features resembling both  $\sigma$ -CAM and OA/RE pathways; the mechanism is one-step, with an ‘oxidative-addition-like’ three centre transition state. Metathesis involving the third row metal analog ( $\text{M} = \text{Os}$ ) does not retain any semblance of the  $\sigma$ -CAM mechanism. In fact, the intermediate that results from oxidative-addition,  $[\text{Tp}(\text{PH}_3)\text{Os}(\text{H})_2\text{CH}_3]$ , is stable enough that the ensuing reductive elimination is energetically unfavorable. The authors note that the large size and electron-rich character of the osmium centre enable sufficient  $d_{\text{M}} \rightarrow \sigma_{\text{CH}}^*$  backbonding to fully cleave the C-H bond and support the formal (IV) charge.

The mechanisms that underlie the reactions of **30/38** with hydrogen are the focus of ongoing computational investigations.<sup>36</sup> Figure **2.12** depicts the reaction of **30** with H<sub>2</sub> using simplified  $\sigma$ -CAM and OA/RE templates (pathway **A** and **B** respectively).<sup>v</sup> In pathway **A** the metathesis proceeds as a single step with concomitant Co–C bond breaking and Co–H bond making events. A filled metal based orbital is involved in the four-centre transition state **TS**. In pathway **B**, the oxidative addition of H<sub>2</sub> to one cobalt centre yields an intermediate (**INT**) with a six-coordinate cobalt(IV) centre. Subsequent reductive elimination reduces the formal oxidation state to Co(II) with the release of methane.

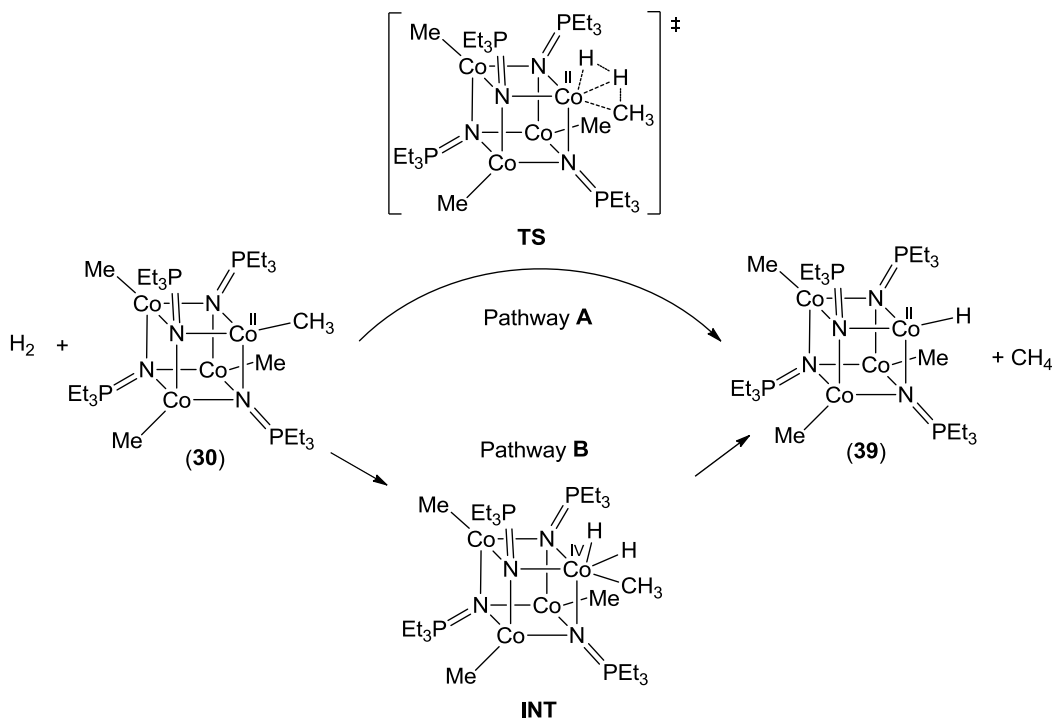


Figure **2.12**:  $\sigma$ -CAM and OA/RE pathways for the reaction of [CoMe(NPEt<sub>3</sub>)<sub>4</sub>] (**30**) with hydrogen.

<sup>v</sup> Figure **2.12** only shows the process for **30**. The non-integral oxidation states of **38** are more difficult to depict, but are conceptually similar.

There is little evidence to discount any pathway for the hydrogenolysis reactions of **30** and **38** *a priori*.  $\sigma$ -CAM type mechanisms are often favored in first row metal systems because small metals are limited in their ability to accommodate the increase in coordination number and oxidation state required in the oxidative-addition step. However, OA intermediates of **30/38** are likely to be accessible. The cobalt centres in **30/38** are relatively low coordinate, OA increases the coordination number to six, and six coordinate pseudo-octahedral geometries are well preceded in both mono-metallic and small cluster cobalt systems.<sup>51</sup> The stability of tetra-alkyl cobalt(IV) complexes<sup>52,53</sup> suggests that the 4+ oxidation state of one cobalt centre in intermediate **INT** is feasible, especially given the potential for charge attenuation *via* intra-cluster metal-metal bonding interactions.

It is almost certain that the reactions of **30** and **38** with hydrogen proceed through different mechanisms (*vide infra*). If so, it is likely that the mechanism for complex **30** would lie closer to the OA/RE end of the spectrum than the cationic cluster **38**. The cobalt centres of **30** are more electron rich and would be more capable of providing the  $d \rightarrow \sigma^*$  electron donation required for the cleavage of the dihydrogen bond. The fractionally higher formal charge on the metals of **38** would also make an OA intermediate less kinetically accessible and less stable. It may seem unlikely that the single electron oxidation that differentiates **38** from **30** could result in different activation mechanisms, but apparently slight steric/electronic manipulations in other late metal systems have been shown to induce great mechanistic consequences. For example, DFT calculations on the

hydrogen metathesis reactions of two superficially similar iridium systems,  $[(\text{PONOP})\text{Ir}(\text{H})(\text{CH}_3)]^+$  (**40**) (PONOP = 2,6-bis(di-*t*-butylphosphinito)pyridine) and  $[\text{CpIr}(\text{PMe}_3)(\text{CH}_3)]^+$  (**41**) (Cp = cyclopentadienyl), have been shown to proceed by different mechanisms (Figure 2.13).<sup>54</sup> Both precursors are five-coordinate cationic monometallic iridium(III) alkyl complexes. The Ir–C bond hydrogenolysis of **41** proceeds by OA/RE through a cationic seven-coordinate iridium(V) intermediate. No intermediate(s) were located on the Ir–C bond hydrogenolysis energy surface for **40**; the process proceeds in a single step *via* a four-centred transition state ( $\sigma$ -CAM).

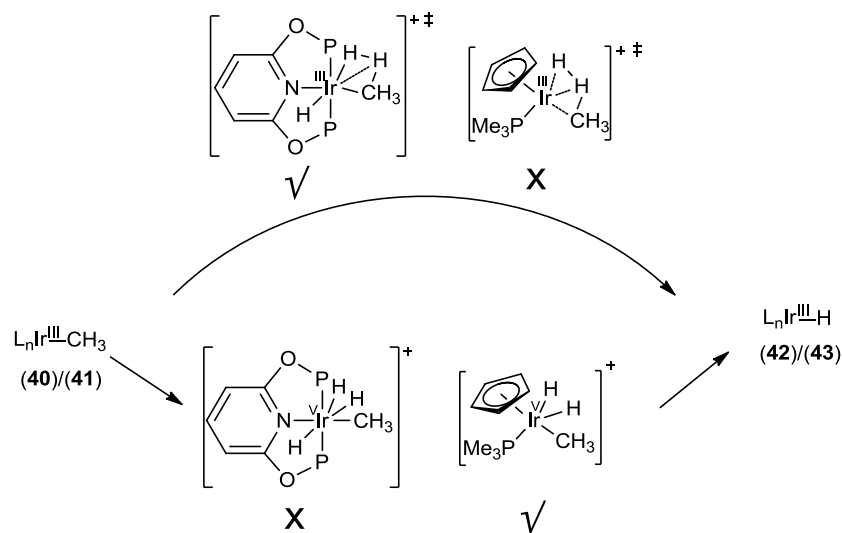


Figure 2.13: Metathesis reactions of two similar iridium systems,  $[(\text{PONOP})\text{Ir}(\text{H})(\text{CH}_3)]^+$  (**40**) (PONOP = 2,6-bis(di-*t*-butylphosphinito)pyridine) and  $[\text{CpIr}(\text{PMe}_3)(\text{CH}_3)]^+$  (**41**) (Cp = cyclopentadienyl), shown to proceed by different mechanisms.<sup>54</sup>

Because precatalysts **30** and **38** are comprised of multiple metals, it is possible that their interactions with hydrogen could be bimetallic. Usually the addition of

hydrogen to a metal cluster is not a bimetallic process because 4-centre addition of H<sub>2</sub> across a metal-metal bond is technically symmetry-forbidden.<sup>55</sup> Instead, most bimetallic systems that activate hydrogen do so at one metal centre prior to intramolecular hydride transfer.<sup>56</sup> For example, DFT investigations on the bimetallic iridium system **44** suggest hydrogen activation occurs at a single iridium centre, followed by hydride transfer (Figure 2.14). Hydrogen coordinates to the mixed-valent Ir<sub>2</sub>(0/II)<sup>+</sup> core of **44** at the Ir(II) centre (the Ir(0) is electronically saturated), forming the η-dihydrogen complex **45**. Transition state **TS** shows the characteristics of both oxidative addition of the dihydrogen ligand to the Ir(II) centre and hydride transfer along the Ir–Ir bond. In the final product **46** the hydride ligands are orthogonal to each other on opposite metals.

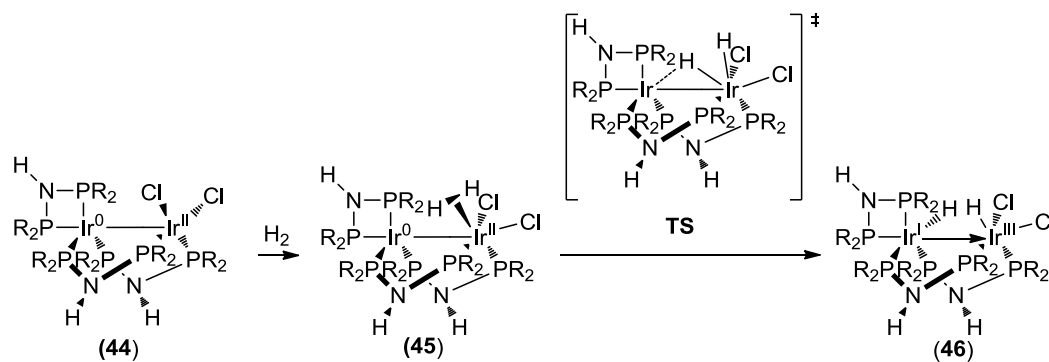


Figure 2.14: Hydrogen activation at a single iridium centre with intramolecular hydride transfer to give a bimetallic dihydride complex (**46**).<sup>56</sup>

Because **30** and **38** do not contain direct metal-metal bonds, bimetallic 4-centre hydrogen addition across the face of the cubane cluster is not symmetry forbidden. In fact, the HOMO's are well situated for such a process.<sup>36</sup> The two arrows in Figure 2.15 indicate the out-of-phase filled orbital interaction across the

face of the heterocubane **30**. The mixed-valence cluster **38** features a similar disposition of orbitals. These orbitals are of suitable orientation and phase to donate electron density into the  $\sigma^*$ -orbital of  $H_2$ . Bimetallic oxidative addition across one face of cluster **30** would yield two five-coordinate cobalt(III) hydride centres. Reductive elimination of methane at a single centre would yield a two-coordinate cobalt(I) centre. Such a low-valent electron rich centre would likely undergo OA of molecule of  $H_2$  with little activation barrier.

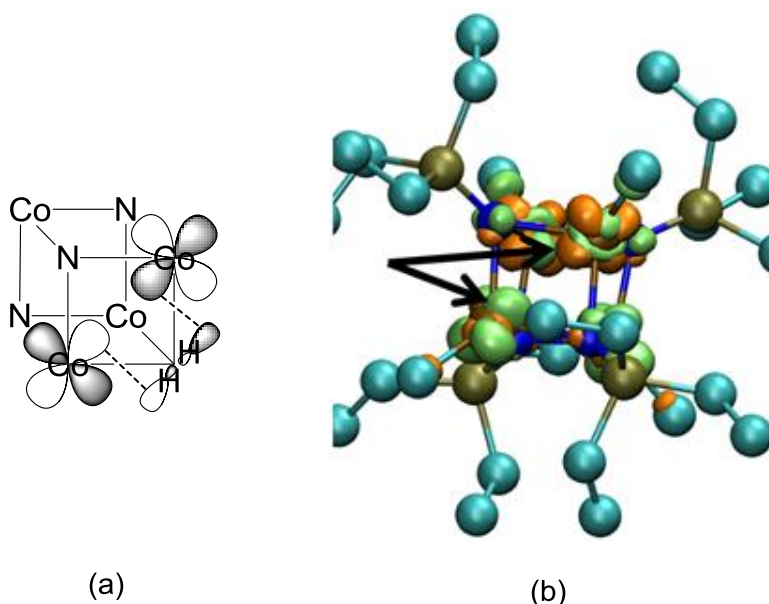


Figure **2.15**: Schematic (a) and DFT (b) depictions of the HOMO of  $[CoMe(NPEt_3)_4]$ . Green and orange coloring indicate orbital phases. Black arrows indicate an out of phase orbital interaction across the phase of the cubane core.

#### 2.4.4 $[CoMe(NPEt_3)_4]$ and $[CoMe(NPEt_3)_4]PF_6$ as precatalysts for hydrodesulfurization

While the following chapter presents our catalytic hydrodesulfurization in detail, a single example is included here to further this discussion of the differences

between neutral cluster **30** and cationic cluster **38**. Initial desulfurization trials using precatalyst **30** and dibenzothiophene show interesting trends in reactivity as a function of reaction and reactor conditions (Table 2.7). The reaction proceeds slowly but catalytically under high pressure (34 atm H<sub>2</sub>); at lower pressure (1 atm H<sub>2</sub>), the reaction does not proceed at all (entries **1** vs. **2**). Also, under high pressure conditions, longer reaction times afford higher TOF's than shorter-term reactions (entries **1** vs. **3**). When the reaction time is limited to less than two hours, essentially no turn-over is observed (entry **4**). These observations establish that the catalytic activity is preceded by an induction period. During this time, the precatalyst is converted very slowly into its active form, presumably by Co–C bond hydrogenolysis.

Table 2.7: Catalytic hydrodesulfurization of dibenzothiophene by [CoMe(NPEt<sub>3</sub>)<sub>4</sub>] (**30**) and [CoMe(NPEt<sub>3</sub>)<sub>4</sub>]PF<sub>6</sub> (**38**).<sup>a</sup>

Entry	[Cat]	H <sub>2</sub> Pressure (atm)	Time (h)	TOF <sup>b</sup> (h <sup>-1</sup> )
1	<b>30</b>	34	17	4.62
2	<b>30</b>	1	17	0.0
3	<b>30</b>	34	2.0	4.06
4	<b>30</b>	34	1.2	0.0
5	<b>38</b>	1	0.5	95.00

- a. Experiments under 1 atm H<sub>2</sub> pressure were conducted in sealable medium-walled glass vessels charged with 1 atm H<sub>2</sub> at 25°C and excess KH, followed by immersion in a thermostat-regulated oil bath at the given temperature. High pressure experiments were conducted in a similar manner using in a stainless steel autoclave.
- b. Moles of C–S bonds cleaved per mol of cluster per hour.

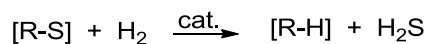
We proposed that precatalyst **30** is slow to activate because it lacks a low-lying empty orbital for hydrogen coordination (see Section 2.2.1). This hypothesis prompted our synthesis of the mixed-valence cluster **38** by single electron outer-sphere oxidation. Cationic complex **38** is a vastly superior precatalyst, catalytically desulfurizing dibenzothiophene at 110 °C under one atmosphere of hydrogen, without a notable induction period, and at a much higher rate than observed for precatalyst **30** under much harsher conditions (entries **5** vs. **1**). This increase in reactivity is discussed in detail in section **3.2**.

### ***3. Mixed-valence cluster catalysts for hydrodesulfurization***

#### *3.1 Introduction and background*

##### *3.1.1 Hydrodesulfurization with heterogeneous catalysts*

Hydrodesulfurization (HDS) is the reaction of organosulfur compounds with hydrogen over a catalyst leading to the extrusion of hydrogen sulfide, with concomitant production of the corresponding hydrocarbon (Eqn. **3.1**).<sup>57</sup> As the principle method for sulfur removal from petroleum feedstocks, HDS is an enormously important and thoroughly researched catalytic process. Escalating costs associated with upgrading high sulfur content resources and increasingly strict government regulations on sulfur content in liquid fuels heighten the need for hydrodesulfurization technologies that are rigorously efficient and cost effective on a massive scale.



Eqn. **3.1**

Crude oil sulfur content typically varies between 0.5–7 %<sub>wt.</sub> depending on origin and geological history.<sup>58</sup> The organosulfur compounds common in crude oils can be broadly categorized as either organosulfides or thiophenic derivatives (Figure **3.1**). Organosulfides – including thiols, thioethers, and disulfides – are relatively easy to desulfurize using conventional HDS technologies; thiophenic derivatives – thiophenes, benzothiophenes, and dibenzothiophenes – are not. After

conventional HDS processing, virtually all of the sulfur compounds remaining in diesel and middle distillate fractions are thiophenic derivatives.<sup>58</sup> Clear trends within the thiophenic series show reactivity decreasing in the order thiophene >> benzothiophenes > dibenzothiophenes.<sup>59</sup> The excision of sulfur from these compounds – the most refractory organosulfur derivatives common in crude oils – has been termed ‘deep desulfurization’. Alkyl substituents, particularly those positioned proximal to sulfur, further increase the refractory character of thiophenic derivatives as they inhibit productive interactions with catalysts by physically limiting access to the C–S bonds. The desulfurization of 4,6-dialkyl dibenzothiophenes has been termed ‘ultra-deep desulfurization’. In light of the pursuit of zero-sulfur content fuels, modern HDS catalyst design aims to develop cost-effective systems capable of deep and ultra-deep desulfurization under mild conditions.

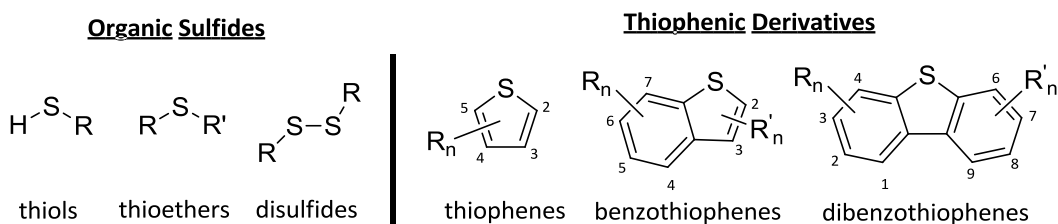


Figure 3.1: Organo-sulfur moieties common in crude oils. The thiophenic derivatives are labeled with conventional numbering schemes used to indicate substituent placement.<sup>57</sup>

Conventional HDS catalysts are prepared by impregnating high surface-area alumina with ammonium molybdate and hydrated cobalt salts.<sup>60</sup> After drying, calcination, and sulfidation, the surface is composed primarily of molybdenum

sulfide, cobalt sulfide, and cobalt molybdates. Extensive physical characterizations (EXAFS, emission Mössbauer and IR spectroscopy, X-ray diffraction, and electron microscopy) suggest that the catalytically active sites are broadly comprised of MoS<sub>2</sub> crystallites with unsaturated cobalt atoms occupying edge and corner positions: the “CoMoS” phase model. In spite of extensive surface characterizations, the true structure of active sites and the mechanisms by which these catalysts function remain poorly understood.<sup>61</sup> Rational design of optimal heterogeneous hydrotreatment catalysts remains a great challenge. The abundant literature pertinent to catalytic HDS in particular lacks consensus reactivity patterns and catalyst structure/reactivity relationships, largely because of variability in catalyst compositions and inadequate characterization.

The lack of well-defined trends can be mitigated by systematic mechanistic and kinetic studies using rigorously characterized, hydrocarbon-soluble catalysts. Within this context, organometallic chemistry has become a powerful tool for understanding HDS on a mechanistic level.<sup>62</sup> Studies of metal complexes stable enough to be characterized, yet primed for reactivity towards organosulfur derivatives, have added substantial depth to the current understanding of HDS reactions.

### *3.1.2 Homogeneous catalysts for hydrodesulfurization*

Investigation of molecular chemistry pertinent to HDS began in the 1980's and research continues unabated. The large number of thiophene-coordinated

transition metal complexes synthesized and characterized over the last 30 years afford a thorough account of the common thiophenic bonding modes.<sup>57</sup> The activation of thiophenic C–S bonds has been observed in a number of systems, and some mediate stoichiometric desulfurization reactions. Researchers are pushing the state-of-the-art towards systems that are capable of *catalytic* deep desulfurization and significant strides have been made towards this end. Homogeneous HDS-related chemistry has been reviewed in detail,<sup>57</sup> this section highlights a handful of case-studies that provide sufficient background for the discussion of the results disclosed here. While the vast majority of research in this area features monomeric complexes of the second and third row transition metals, this section focuses on cluster-mediated HDS and monometallic systems comprised of the first-row metals.

A handful of bonding modes have been identified in thiophene transition metal complexes (Figure 3.2) and general patterns have emerged relating bonding modes to reactivity profiles. The coordination mode most often associated with C–S bond activation is  $\eta^1(\text{S})$ . In this mode, the thiophenic sulfur atom is coordinated to the metal and pyramidal, corresponding to approximate  $sp^3$  hybridization. The ring system maintains planarity but is typically perturbed by  $d \rightarrow \pi^*$  back-bonding, resulting in elongated C–C and C–S bond lengths.<sup>63</sup> Crystallographically characterized complexes featuring  $\eta^2(\text{C}_2)$  and  $\eta^3(\text{SC}_2)$  coordinated thiophenic ligands are rare, but both such modes have also been implicated in C–S activation processes.<sup>64,65</sup> Computational studies suggest these

bonding modes interconvert rapidly with the  $\eta^1(\text{S})$  mode, with little activation barrier in some systems.<sup>66</sup> The  $\eta^2(\text{C}_2)$  mode often precedes undesirable exocyclic C–H bond activation.<sup>65</sup> The  $\eta^5(\text{SC}_4)$  thiophene coordination mode is also common, but it is not often associated with HDS-related reactivity. The bonding of  $\eta^5$ -thiophene ligands is similar to that of cyclopentadienyl ligands, although  $\eta^5$ -thiophene ligands are weaker electron donors and stronger  $\pi$ -acceptors. Like cyclopentadienyl ligands,  $\eta^5$ -thiophene ligands are activated towards nucleophilic substitution reactions. The  $\eta^6(\text{C}_6)$  coordination mode observed in benzothiophenes and dibenzothiophene derivatives also results in increased nucleophilic substitution reactivity. This coordination mode is also important in HDS related reactivity:  $\eta^6(\text{C}_6)$  coordination by one metal centre can decrease the barrier towards C–S bond activation by a second metal centre.<sup>67</sup>

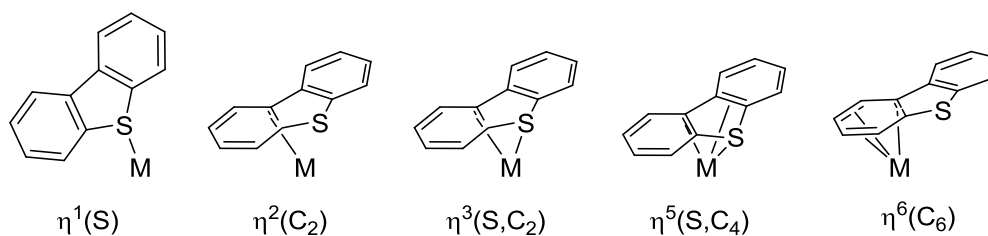


**Figure 3.2:** Common coordination modes observed in thiophene coordinated transition metal complexes.

Most demonstrations of thiophenic C–S bond activation by mononuclear complexes feature electron rich, coordinatively unsaturated metal centres. One archetypal example involves the  $\text{ML}_4$  16-electron fragment  $[\text{Cp}^*\text{Rh}(\text{PMe}_3)]$  which is formed by thermolysis of the rhodium(III) precursor **45** (Figure 3.3-I).<sup>68</sup> Heating a benzene solution of **45** and thiophene to reflux forms the  $\eta^2(\text{S,C})$ -

thiametallacycle complex **46**. The ring opening reaction is formally an oxidative addition of the C–S bond across the rhodium centre. The authors propose a two-step process. First, the  $[\text{Cp}^* \text{Rh}(\text{PMe}_3)]$  fragment coordinates thiophene sulfur forming the 18-electron intermediate  $\eta^1(\text{S})\text{-INT}$ . Donation of electron density from the electron rich rhodium(I) centre to the antibonding  $\pi$ -orbital presumably weakens the thiophene C–S bond of this intermediate. This lowers the activation barrier to the second step: migration of the  $\alpha$ -carbon from sulfur to rhodium to form the thiametallacyclohexadiene **46**. Similar C–S bond activation reactions occur when **45** is heated in the presence of 2-methylthiophene, 3-methylthiophene, 2,5-dimethylthiophene, benzothiophenes and dibenzothiophene. In the case of 2,5-dimethylthiophene, the ring-opened product was characterized crystallographically. The structure shows the sulfur and diene fragment in a planar geometry with the rhodium atom approximately 0.7 Å above the plane. The bond distances indicate a localized diene structure for the two C–C double bonds. Thiametallacycle **46** is formally a six-coordinate rhodium(III) 18-electron complex. Under the conditions of the reaction, no further reaction to give partial or complete desulfurization products is observed. This is a common occurrence for monometallic systems – the activation of the first C–S yields a stable complex that cannot be provoked to complete the second C–S bond cleavage. Polymetallic systems do not necessarily rely on a single metal centre to mediate all of the steps required to complete full desulfurization, a common design feature we too have adopted.

Accessing the same low-valent rhodium(I) fragment by photolysis at low temperature leads to different reactivity towards thiophenic derivatives (Figure 3.3-II). Photolysis of dihydride **47** in the presence of thiophene forms a mixture of **46** and a new complex **48** – the result of C–H bond activation. Carbon-hydrogen bond activation events are not uncommon in HDS-related reactivity. Thiophenic derivatives have C–S bond energies around 93 kcal/mol; the corresponding C–H bond energies are of similar energy (~102 kcal/mol). In this case, complex **48** is a kinetic intermediate, which slowly interconverts to the thermodynamic product **46** over a number of weeks. Computational experiments suggest the formation of **48** proceeds through an  $\eta^2(\text{C}_2)$  intermediate.

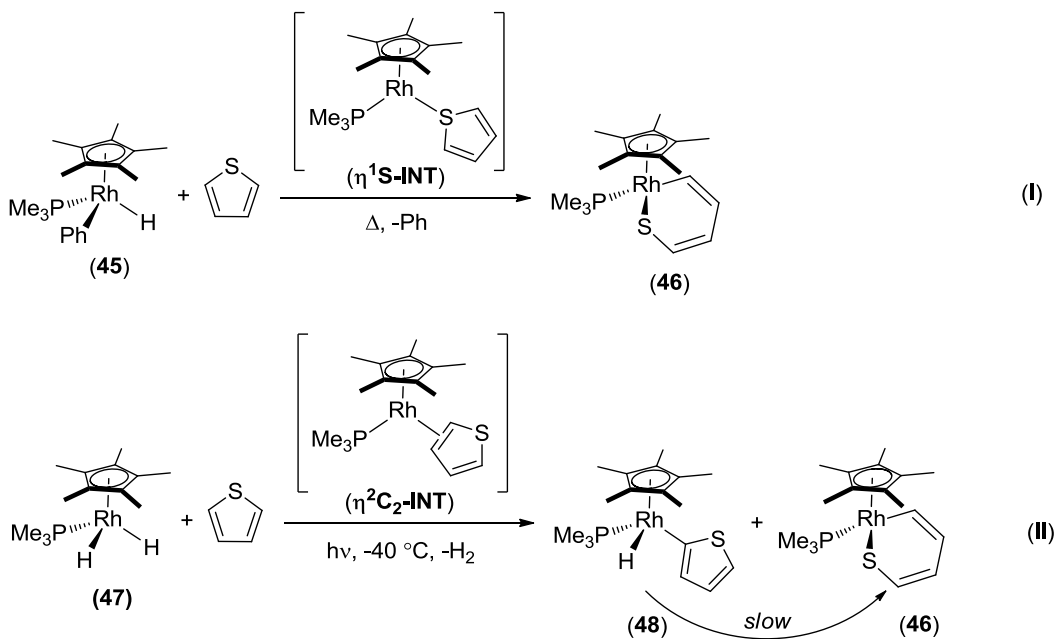
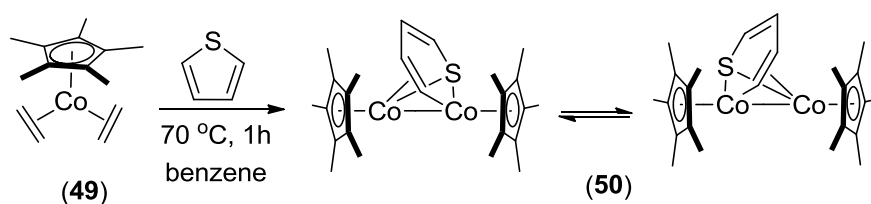


Figure 3.3: C–S and C–H bond activation by an electron rich low-valent rhodium fragment.<sup>68</sup>

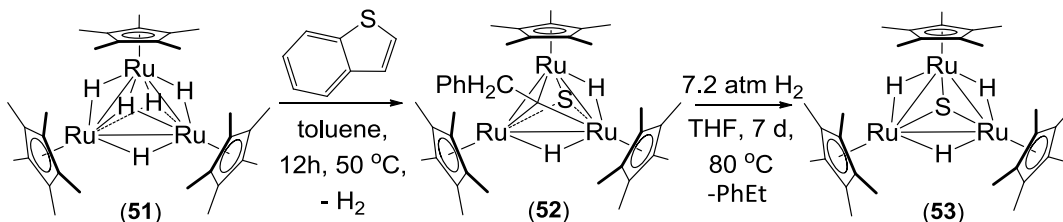
A similar ligand set has been used to support a low-valent cobalt centre capable of analogous chemistry. In spite of its enabling role in the CoMoS phase model for heterogeneous catalysts, very few accounts of cobalt-mediated C–S bond activation have been reported. The reaction of thiophene and the mononuclear cobalt(I) complex  $[\text{Cp}^*\text{Co}(\text{C}_2\text{H}_4)_2]$  **49** forms a dinuclear complex **50** where one cobalt has inserted into the thiophene C–S bond to form a six-membered ring.<sup>69</sup> A second  $[\text{Cp}^*\text{Co}]$  moiety coordinates the thiametallacycle in an  $\eta^3(\text{SC}_2)$  fashion to achieve electronic saturation (Scheme **3.1**). The authors propose complex **50** is formed by initial loss of ethylene, followed by thiophene coordination and insertion into the C–S bond. Loss of the second ethylene most likely occurs from this Co(III) intermediate, which then reacts with another  $[\text{Cp}^*\text{Co}]$  fragment to produce the dicobalt product. Variable temperature  $^1\text{H-NMR}$  experiments show the C–S bond activation to be reversible at room temperature: the thiametallacycle is ‘flipping’ between the two cobalt centres.



Scheme **3.1**

The  $\text{Cp}^*$ -capped triruthenium hydride cluster **51** mediates stoichiometric desulfurizations of benzothiophene and dibenzothiophene (Scheme **3.2**).<sup>70</sup> In the case of benzothiophene, activation of the aromatic C–S bond forms an

intermediate thiaruthenacyclohexadiene complex (not illustrated). This intermediate rearranges to the  $\mu_3$ -alkylidene- $\mu_3$ -sulfido cluster **52** upon warming to 50 °C. In this complex, the organic fragment and the sulfur atom coordinate to opposite sides of the tri-ruthenium plane. The reaction of **52** with hydrogen (7.2 atm) produces, after one week, the desulfurized product ethyl benzene and a new  $\mu^3$ -sulfido complex **53**. Dibenzothiophene is also stoichiometrically desulfurized by cluster **51** under similar conditions, forming biphenyl and the same  $\mu^3$ -sulfido complex **53**. This cluster is the most important precedent we used in adopting a cluster design for the first-row metals. Replacing the supporting Cp\*-ligands with “isoelectronic” phosphoramidate ligands opens two coordination sites per metal. The coordinative unsaturation is placated by the bridging nitrogen interactions. In this light, cluster **51** has exactly the coordination sphere targeted: one supporting ligand per metal and no ancillary ligands other than the hydrides and, in some catalyst stages, a bridging heteroatom or two to be removed by hydrogenolysis.



Scheme 3.2.

To date, *only one first row metal complex has been shown to mediate the complete desulfurization of dibenzothiophene*. The hydride-bridged dimer [(dippe)NiH]<sub>2</sub> **54** readily liberates dihydrogen and inserts into one C–S bond of

dibenzothiophene under ambient conditions (Figure 3.4).<sup>71</sup> The resulting thiametallacycle **55** has been fully characterized. Over the course of five days, **55** converts to four different organometallic products (**56-59**). Simple dippe complexes **56** and dimeric **59**, bearing the biphenyl and sulfur fragments, respectively, are the major products representing 82 % of the organometallic species. The authors propose that the reversible loss of free DBT from the C–S insertion product **55** generates reactive bisphosphine nickel(0) fragments which can further react with **55** to form the range of observed products. Thus, although intermediate **55** is mono-metallic, it is likely that the cleavage of the second C–S bond involves more than one metal centre. Importantly, the reaction of **56** under one atm of hydrogen at room temperature quantitatively yields **54** and free biphenyl: the system has the potential to be catalytic. Moreover, this demonstrates that hydrogen is not necessarily required for the desulfurization of dibenzothiophene, only for the hydrogenolytic release of the organic product. Subsequent research has shown **54** to be a precatalyst for deep desulfurization when “high energy” alkyl Grignard reagents are used instead of hydrogen as the stoichiometric reductant.<sup>72</sup> Unfortunately, a true catalytic deep desulfurization process has not been demonstrated using this catalyst system.

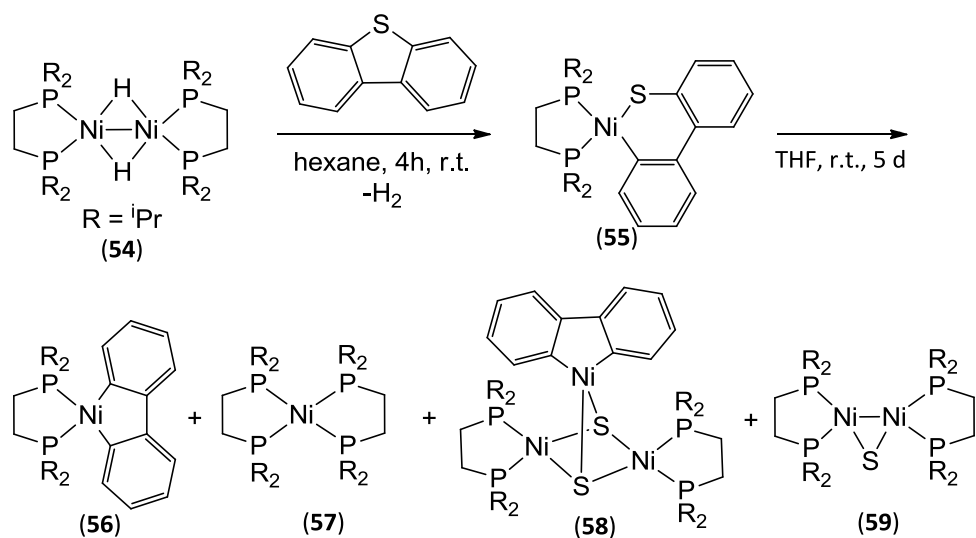
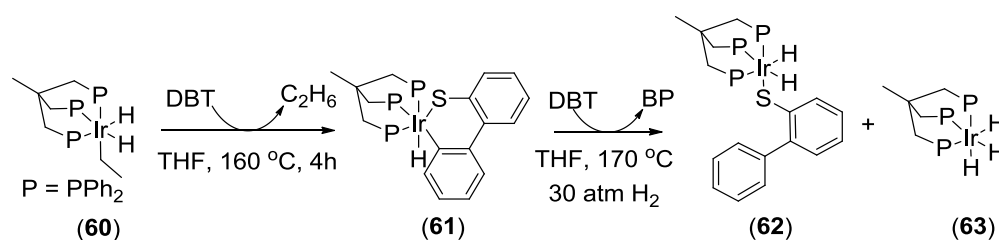


Figure 3.4: A bis(phosphine) nickel hydride dimer capable of stoichiometric desulfurization of dibenzothiophene under ambient conditions.<sup>71</sup>

The very few homogeneous systems reported to execute *catalytic* deep desulfurization are all characterized by a precise molecular architecture involving the tripodal ligand triphos.<sup>57</sup> These novel homogeneous transformations have been achieved for thiophene, benzothiophene, and dibenzothiophene using the electron-rich 16-electron neutral or anionic fragments  $[(\text{triphos})\text{MH}]^n$  ( $\text{M} = \text{Ru}, \text{Ru}, \text{Ir}; n = 0, -1$ ).<sup>73</sup> Typical reaction conditions involve temperatures around 160 °C, hydrogen pressures of 30 atm, and the presence of a strong base, such as potassium tert-butoxide. The *only* example of a complete homogeneous catalytic hydrodesulfurization reaction of dibenzothiophene to biphenyl was observed using the complex  $[(\text{triphos})\text{Ir}(\text{H})]$ . This complex is generated by solution-phase thermolysis of  $[(\text{triphos})\text{Ir}(\text{H})_2\text{Et}]$  (**60**) (Scheme 3.3).<sup>74</sup> Heating Complex **60** to 100 °C in the presence of excess dibenzothiophene promotes reversible C–H activation reactions. Above 100 °C both C–S bond activations occur, and heating

beyond 170 °C gives exclusively the C–S insertion product **61**. Unlike the 18-electron thiametallacycles previously discussed, complex **61** does not decompose under the forcing reaction conditions required to render the process catalytic. Complexes **62** and **63** have been isolated after catalytic runs; both can be reincorporated into the catalytic cycle. The authors note the very slow rate (TOF ~ 0.4 C–S cleavages/h), interference from several unproductive equilibria, formation of multiple products, and the drastic reaction conditions taken together preclude the possibility of a detailed mechanistic investigation for this system.

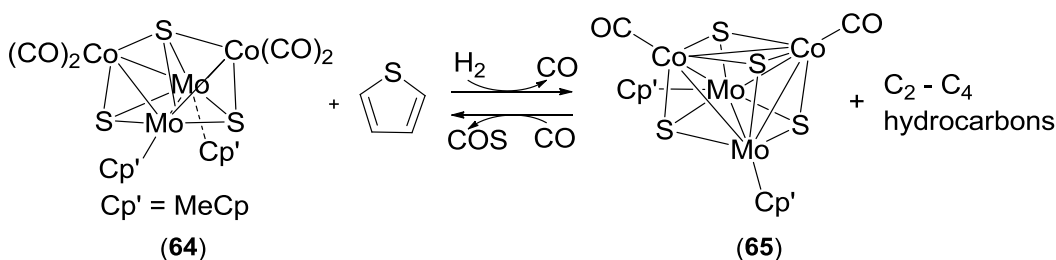


Scheme 3.3

Among the systems capable of mediating stoichiometric solution-phase deep desulfurization, the discrete heterobimetallic clusters published by Curtis and co-workers most closely resembles the surface active sites of heterogeneous hydrotreatment catalysts.<sup>75</sup> The butterfly-shaped cluster **64** is comprised of Cp-capped molybdenum centres and carbonyl-capped cobalt centres; the tetrametallic cluster is held together by  $\mu^3$ -sulfido bridges. This cluster reacts stoichiometrically with thiophene under moderate hydrogen pressure to produce  $C_2$ - $C_4$  hydrocarbons and a new distorted heterocubane cluster in which the extruded sulfur has been incorporated as one corner of the cube (**65**, Eqn. 3.2).

The original cluster **64** can be reformed under high pressure carbon monoxide, forming COS and thereby completing a pseudo-catalytic transformation. This pair of reactions suggest the possibility of constructing a catalytic cycle for the HDS of thiophene under a high pressure mixed atmosphere of CO and H<sub>2</sub>.

Unfortunately, the presence of free CO greatly inhibits the desulfurization reaction, and the process could not be rendered catalytic. Nonetheless, this heterobimetallic system represents the most sophisticated attempt to catalyze homogeneous HDS reported to date.



Eqn. 3.2

Curtis's heterobimetallic complexes are the only examples of clusters designed 'from the ground up' to facilitate hydrodesulfurization. Complex **64** has a number of features that we believe are important for this purpose, and that have direct analogies in the surface chemistry of the CoMoS phase model.<sup>61</sup> One feature pertains to the way the clusters interact with hydrogen: the presence of late metal centres and ancillary ligands with non-bonding electrons allow the cluster to support both hydridic and acidic hydrogen ligands. The geometry of the cluster ensures facile intra-cluster hydrogen migration. SEM characterizations of the

CoMoS phase of heterogeneous catalysts show hydrogen migration across a catalytic surface to be rapid, and the presence of both hydridic hydrogens and acidic protons on such surfaces is well established.<sup>76</sup> A second feature involves the facile formation/cleavage of bonds between bridging inorganic ligands and the metal centres of the clusters. Initial organosulfur coordination to **64** occurs at a cobalt centre, resulting in a slippage of a bridging sulfur atom from  $\mu_3$  to  $\mu_2$ . The authors conceptualize the low energy process associated with forming/cleaving structural-ligand/metal bonds as ‘latent vacancies’ since the metals react as if they have a vacancy in their coordination shell, yet in their resting state, a neighboring sulfur atom fills the metal coordination sphere.<sup>75</sup> Similar transient M–S bond forming/cleavage events are no doubt key in the CoMoS phase model, where the surface sulfur atoms are highly mobile.<sup>60</sup>

Both of these features are also present in the mixed-valence cluster **38**. When doubly bridging, the phosphoranimide ligand has a more or less non-bonding lone pair suitable for supporting acidic protons; the coordinatively unsaturated metal centres are equally well suited to support hydridic hydrogen atoms. Given the delocalized nature of the HOMO of **38**, hydrogen migration around the heterocubane is likely a low-energy process. In addition to the electronically unsaturated nature of precatalyst **38**, the variably hapticity of the phosphoranimide ligands ensures that the cluster embodies the concept of latent vacancies. One way that **38** differs from complexes **64** and **65** is the lack of ancillary ligands, particularly carbonyl ligands. It is well established that C–S

bond activation events are favoured for electron rich metal centres. Carbonyl ligands are strong  $\pi$ -acceptors, decreasing the electron density of late metal centres to which CO coordinates. In addition, carbonyl ligands are substitutionally labile under many reaction conditions and are further likely to undergo insertion reactions. Complex **38** completely lacks ancillary ligands; the cobalt centres are organized exclusively by the strongly-donating nitrogen atom of the phosphoranimide anion, ensuring that the electron density stays where it is needed most.

### ***3.2 Results and discussion***

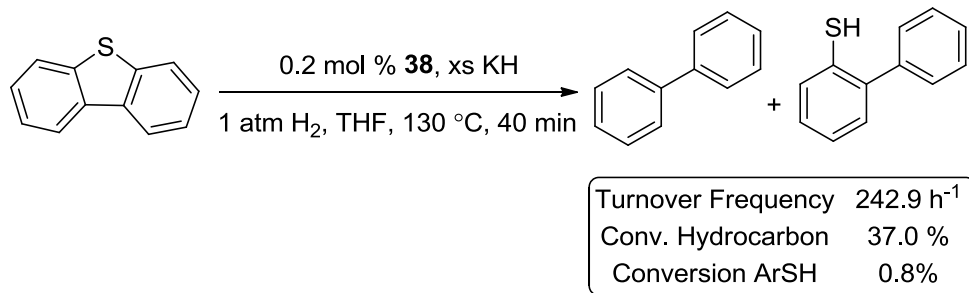
The mixed-valence complex **38** is a precatalyst for the desulfurization of dibenzothiophene and a series of related organosulfur compounds. The desulfurization of dibenzothiophene (Section 3.2.1) has been investigated in more detail than the desulfurization of the other substrates evaluated (section 3.2.2).

The catalytic experiments below report percent conversions and turnover frequencies (TOF's). Percent conversions are determined by integrating starting material/product peaks in the GC-MS spectra. TOF's are calculated based on starting material/product peak integration from GC-MS; one catalytic turnover is calculated as one mole of C-S bond activated product per mole of cluster per hour. In order to directly compare TOF's, determinations must be obtained under 'saturation-kinetics', where rate is not limited by substrate concentration. The

TOF's determined here are 'single-point determinations', and some are limited by substrate concentration. In these instances, the reported values should be considered minimum TOF's.

### *3.2.1 Catalytic desulfurization of dibenzothiophene by [CoMe(NPEt<sub>3</sub>)<sub>4</sub>PF<sub>6</sub>]*

Mixed-valence cluster **38** catalyzes the desulfurization of dibenzothiophene under a wide range of reaction conditions. Temperature, reaction time, scavenger, catalyst loading, and reaction medium all effect the rate of catalysis. The results from a 'typical' catalytic trial are given in Eqn. **3.3**. The reaction of dibenzothiophene and **38** (0.2 mol %) in the presence of KH affords 37 % conversion to biphenyl after 40 minutes at 130 °C. Longer reactions times under similar conditions afford quantitative conversions. These conditions are extremely mild by any metric. As discussed, the lone literature example of catalytic homogeneous HDS of dibenzothiophene requires higher temperatures, hydrogen pressures of 30 atm or more, and proceeds orders of magnitude more slowly.<sup>74</sup> Mild reaction conditions make monitoring reactions much easier; desulfurization reactions with **38** are executed in standard sealed glassware instead of a steel autoclave.



Eqn. 3.3

Catalysts loadings between 5–0.1 mol % give similar turn-over frequencies. It is worth pointing out that 0.2 mol % is a very low catalyst concentration for an exploratory investigation in homogeneous catalysis. The strong preference for biphenyl formation (complete desulfurization) over 1,1'-biphenyl-2-thiol formation (only one C–S cleavage), exemplified in Eqn. 3.3, is typical in this system. Product ratios are determined by GC-MS and reactions run to completion afford ~ 97 % isolated yields of pure biphenyl. The tendency toward complete desulfurization could result from a reaction pathway in which the substrate remains bound to the catalyst for both C–S bond activation events. The distribution could also be an extension of the relative strengths of the C–S bonds of dibenzothiophene and biphenyl thiol; the C–S bond of dibenzothiophene is ~ 12 kcal/mol stronger than that of biphenyl-2-thiol.<sup>77</sup> It is important to note that no products associated with aromatic ring hydrogenation were identified in catalytic desulfurization trials using this catalyst. Ring hydrogenation prior to C–S bond activation is one of two dominant mechanistic proposals for heterogeneous HDS catalysis.<sup>78</sup> Aromatic hydrogenation lowers the enthalpic barrier to C–S bond activation, as S–C<sub>sp3</sub> bonds are weaker than S–C<sub>sp2</sub> bonds. Hydrodesulfurization

via aromatic hydrogenation is undesirable because the hydrogenation events waste hydrogen and reduce fuel quality, lowering the octane rating.

### *3.2.1.1 Control experiments: preliminary mechanistic analysis*

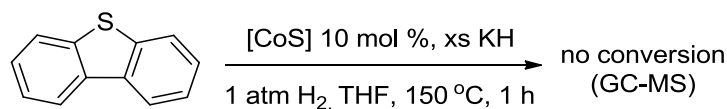
Control experiments provide insight into the factors contributing to the catalytic desulfurization of dibenzothiophene mediated by precatalyst **38**. The ‘mercury-puddle test’ is a well-established method for differentiating homogenous and soluble nanoparticle catalysts; Hg(0) most often poisons colloidal or metal-nanoparticle heterogeneous catalysts by amalgamating the metal or absorbing it on the mercury surface.<sup>79</sup> Parallel desulfurization reactions run in the presence/absence of a large excess of Hg(0) provide (negative) evidence that the active catalyst in the desulfurization of dibenzothiophene by **38** is homogeneous (Table **3.1**). Under the conditions tested, the presence of Hg(0) does not have a noticeable effect on the conversion of dibenzothiophene to biphenyl (entries **1** and **2**). While these results provide a strong indication that **38** does not decompose to form metallic nanoparticles, the ‘mercury-puddle test’ is not definitive on its own; homogeneous character can only be established by using a suite of testing methodology (TEM, quantitative ligand poisoning, “Crabtree’s test,” “Maitlis’ test,” etc.).<sup>80</sup>

Table 3.1: Differentiating heterogeneous and homogeneous processes in the catalytic desulfurization of dibenzothiophene by  $[\text{CoMe}(\text{NPEt}_3)_4]\text{PF}_6$ .

Entry	DBT (mg, mmol)	Hg(0) (g, mmol)	Biphenyl <sup>a</sup> (mg, mmol)	Isolated yield (%)
<b>1<sup>b</sup></b>	134.1, 0.72	2.2, 10.8	105.8, 0.69	95.3
<b>2<sup>c</sup></b>	134.9, 0.73	0.0, 0.0	107.9, 0.70	95.5

- Product identified by GC-MS.
- Experiment conducted in a sealable medium-walled glass vessel charged with THF, DBT and **38**, excess purified KH, and Hg(0) under 1 atm H<sub>2</sub> at 25 °C, followed by immersion in a thermostat-regulated oil bath at 150 °C for two hours.
- Experiment conducted as in (b), except no Hg was added to the reactor.

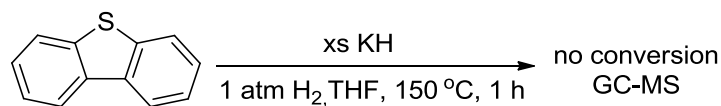
The potential for precatalyst **38** to decompose ultimately to colloidal cobalt sulfide prompted us to determine if bulk cobalt sulfide catalyzes the desulfurization of dibenzothiophene under the mild conditions used here (Eqn. 3.4).<sup>vi</sup> A slurry of cobalt sulfide, dibenzothiophene, and potassium hydride in THF under one atm of hydrogen does not result in the formation of either biphenyl or biphenyl sulfide after one hour at 150 °C. Under such mild conditions, cobalt sulfide is not an active catalyst for the desulfurization of dibenzothiophene, as might be anticipated.



Eqn. 3.4

<sup>vi</sup> Under the harsh reaction conditions employed in industrial HDS reactors (~300 °C, ~30 atm H<sub>2</sub>) cobalt sulfide does catalyze the desulfurization of dibenzothiophene.<sup>146</sup>

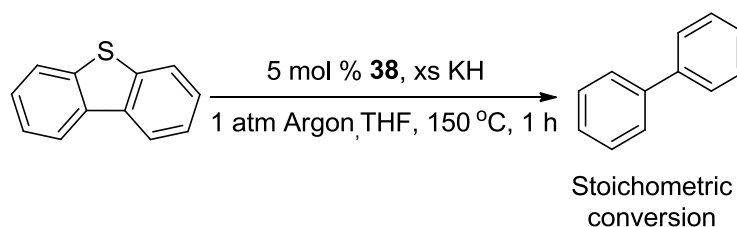
The inclusion of potassium hydride as acid scavenger in desulfurization trials prompted us to determine if potassium hydride itself catalyzes or co-catalyzes the desulfurization of dibenzothiophene (Eqn. **3.5**). A THF slurry of potassium hydride and dibenzothiophene under one atm of hydrogen at 150 °C does not produce either biphenyl or biphenyl sulfide after one hour. Although potassium hydride is not a catalyst under the short reaction times and mild conditions used in catalytic trials using precatalyst **38**, other group members have noted KH-induced C–S bond activation under longer reaction times and/or harsher reaction conditions.<sup>23</sup> For this reason, a rigorous purification protocol has been adopted by the group to eliminate the potassium metal content present in commercial potassium hydride.<sup>23</sup>



Eqn. **3.5**.

The potential for potassium hydride to act as a stoichiometric reductant prompted another important control experiment, now in the absence of hydrogen. Thus, a THF slurry of potassium hydride, precatalyst **38**, and dibenzothiophene under an argon atmosphere (instead of hydrogen) at 150 °C affords stoichiometric – not catalytic – conversion to biphenyl upon acid workup (Eqn. **3.6**). Given that the reaction proceeds catalytically under one atmosphere of hydrogen, it is thus likely that hydrogen is the active reductant in the catalytic trials discussed here. To

prove this rigorously, reactions under deuterium gas and/or reactions with potassium deuteride must be conducted to provide more information regarding the interplay between the species involved.



Eqn. 3.6

*3.2.1.2 Mechanistic discussion: Catalytic desulfurization of dibenzothiophene by  $[CoMe(NPEt_3)]_4PF_6$*

Cluster-based catalytic systems are more difficult to study mechanistically than monomeric systems. The precatalyst **38** poses a greater challenge than other polymetallic precatalyst systems because the cluster is paramagnetic. There is little experimental evidence to direct a discussion of the mechanism(s) involved in the catalytic desulfurization of dibenzothiophene by this catalyst, but computational collaborators and experimental researchers in the Stryker group are working to address this.<sup>36</sup> For this reason, a general mechanistic discussion is pertinent as it may serve as a ‘road map’ for future synthetic, kinetic, electrochemical, and computational experiments.

Discussing a generalized scheme for homogeneous catalytic hydrodesulfurization is a useful prelude to a specific discussion of precatalyst **38** and its interactions with hydrogen and dibenzothiophene. The highly simplified scheme shown in Figure **3.5** highlights the key steps involved in any desulfurization of an organosulfur compound (RSR') by a transition metal complex of any nuclearity  $[L_iM]_n$ . The first step, off the catalytic cycle, involves the transformation of a kinetically stable precursor into an active catalytic species. In the second step, the activated species coordinates and inserts into one of the C–S bond of the substrate forming new S–M and C–M bonds. The third step involves the hydrogenolysis of the newly formed M–C bond to give a new C–H bond and a metal hydride species. Substrate release at this point in the cycle gives a 'partially desulfurized' thiol, which would be scavenged by the strongly basic additive. In the fourth step, recoordination (if necessary) and activation of the second carbon sulfur bond forms a new complex in which the sulfur and the hydrocarbyl fragment are no longer linked. The fifth step in the desulfurization process involves the hydrogenolysis of the C–M bond affording a 'fully desulfurized' hydrocarbon and a metal sulfide species. Transition metal sulfides are notoriously stable complexes; in catalytic desulfurization this is invariably the thermodynamic low-point of the cycle. (Industrial hydrotreatment catalysts are prepared and stored in this form, then activated by exposure to high hydrogen pressure and heat.<sup>57</sup>) The final step of the cycle – removing sulfur from the now deactivated catalyst – is rate limiting. This step is drawn as an equilibrium to highlight that the reaction needs to be driven forward to turn over the catalyst and close the cycle.

Laboratory scale catalytic hydrodesulfurization requires the use of basic salts to drive the equilibrium in favour of catalyst regeneration by ‘scavenging’ the hydrogen sulphide byproduct and sequestering the sulfur atoms. The function of sulfur scavengers is discussed in the following section; the mechanistic steps proposed and further discussed here pertain to scavenger-free conditions.

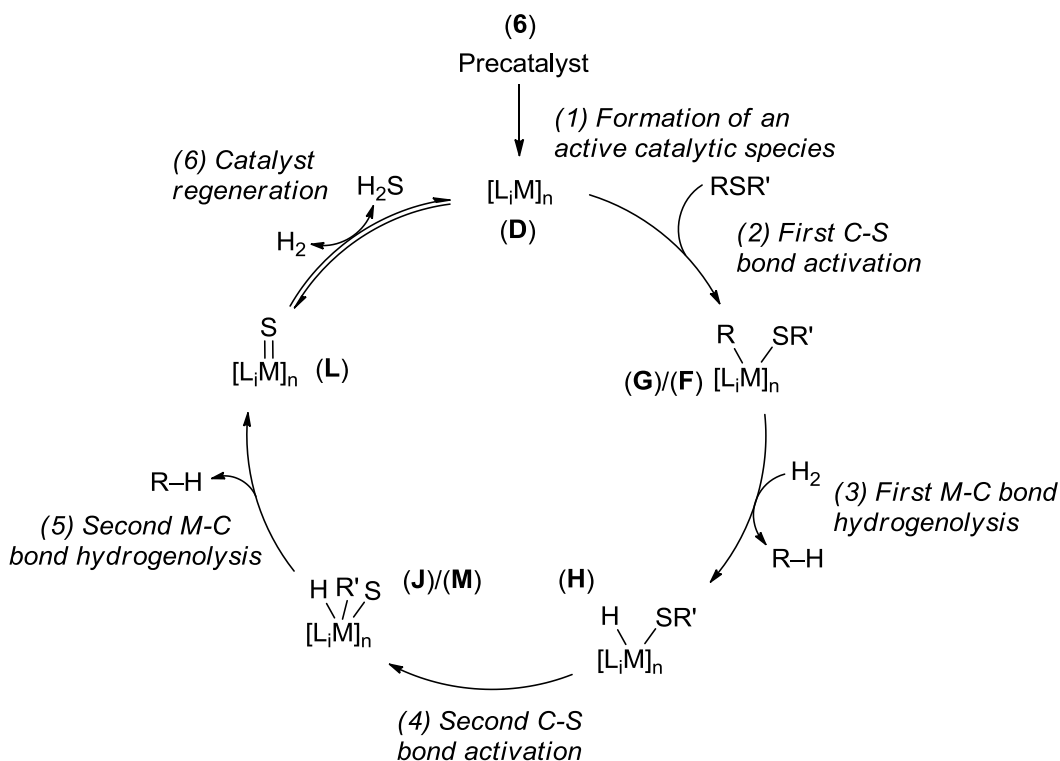


Figure 3.5: A generalized cycle for the catalytic hydrodesulfurization of an organosulfur substrate ( $RSR'$ ) by a transition metal cluster  $[L_iM]_n$ .<sup>vii</sup>

<sup>vii</sup> Compound numbers from Figures 3.7 and 3.8 are included to relate the proposed mechanism for the catalytic desulfurization of dibenzothiophene by 38 to the generalized cycle.

*(1) Formation of an active catalytic species*

The following experimental observations provide clues about how precatalyst **38** is converted into an active species: [1] Bubbling hydrogen gas through a THF solution of **38** and then removing the solvent under reduced pressure leaves a mixture of two solids – one with an elemental composition consistent with that of the neutral cluster **30**, the other with solubility characteristics similar to **38** but dissimilar elemental composition. [2] Cyclic voltammetry experiments conducted by our collaborators<sup>37</sup> indicate that *both 38 and 30 remain tetrameric in THF solution in the absence of hydrogen.*

We propose two processes for the activation of **38** that are in accord with these observations (Figure 3.6). In pathway (i), the reaction of **38** with hydrogen leads to an intermediate cobalt-hydride cluster **A**. Complex **A** is depicted with four hydride ligands and no methyl ligands for simplicity, but the ensuing process could proceed after as few as one Co–C hydrogenolysis event. An outer-sphere electron transfer from cluster **A** to a second molecule of **38** yields neutral cluster **30**, and a new cluster, **B'**, that is the proposed active species. Complex **B'** is drawn as a tetramer, but there is no experimental evidence to support any particular cluster nuclearity; complex **B'** is drawn as dimer **B** in later figures for simplicity and clarity. Since cyclic voltammetry experiments in the absence of hydrogen do not show any disproportionation of **38** to give **30** and the dication  $[\text{CoMe}(\text{NPEt}_3)]_4^{2+}$ , the reaction of **38** with hydrogen must precede electron transfer. It is possible that electron transfer is more facile in **A** than in **38** because

hydride ligands are stronger donors than methyl ligands. Cyclic voltammetry experiments in the presence of hydrogen are currently underway.

The alternate process for the activation of **38** involves the reversible dissociation of the tetramer into two dimers **C** and **D** (pathway **ii**). In the absence of hydrogen the equilibrium lies far to the left, in accord with the noted cyclic voltammetry data. In the presence of hydrogen, the equilibrium shifts to the right as cationic dimer **C** reacts to form **B**. Two molecules of the neutral dimer **D** re-aggregate to form **30**. Solution-phase molecular weight determinations by vapour phase osmometry indicate similar dissociation equilibria exist for the related cluster,  $[\text{CoCl}(\text{NPEt}_3)]_4$ .<sup>16</sup> The cationic dimer **B** is very low-coordinate, and would likely be heavily solvated, if not solvent coordinated, or may couple with a second molecule of **B** to form a tetramer. Complex **B** is drawn – with brackets – as a cluster of unknown nuclearity to indicate this. In the figures that follow all the intermediate complexes are depicted as dimers. Many of the structures could be higher nuclearity and/or solvent coordinated, but they are not drawn this way.

For (**i**) to be a reasonable pathway, the electron transfer reaction must be faster than the hydrogenolysis reaction that precedes it. This stipulation seems reasonable given that electron transfer reactions are typically orders of magnitude faster than bimolecular chemical reactions.<sup>38</sup> Under the conditions of pathway (**i**) no more than half the moles of precatalyst **38** are converted into active catalyst. If pathway (**i**) is involved in the formation of active catalytic species, the dicationic complex  $[\text{CoMe}(\text{NPEt}_3)]_4^{2+}$  will be a more efficient precatalyst.

In order for pathway (ii) to be in accord with the elemental analysis and cyclic voltammetry data, the dimerization of **D** must be faster than the reaction of **D** with hydrogen. This seems less likely given the high coordinative unsaturation of **D**, although hydrogen is not particularly soluble in THF – even at room temperature. Overall, pathway (i) appears more reasonable than pathway (ii), given the evidence available. Pathways (i) and (ii) both imply that a maximum of 50 % of the precatalyst is converted to one or more active catalytic species. Understanding how precatalyst **38** is activated will aid future catalyst development work, increasing the percentage of precatalyst that enters the catalytic cycle.

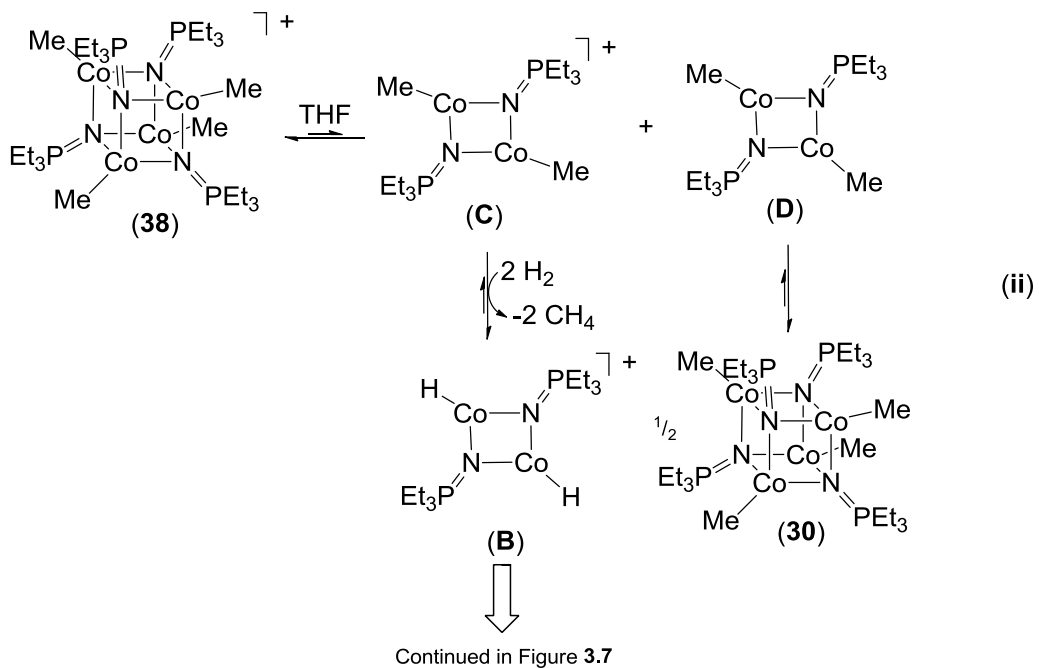
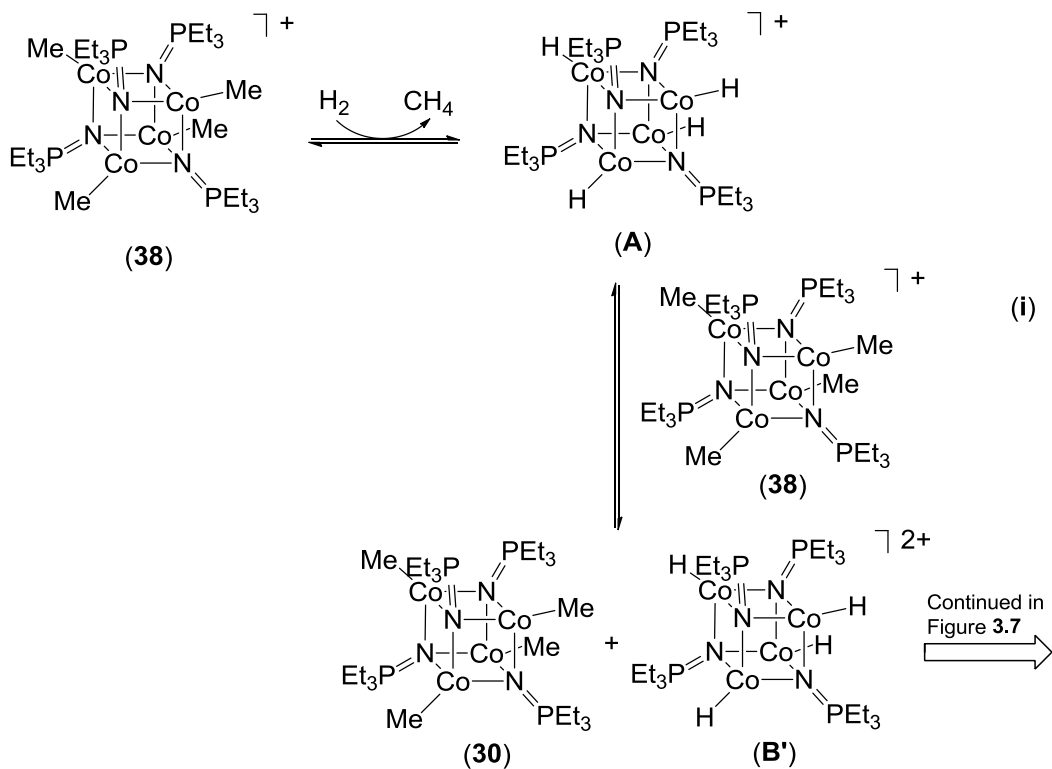


Figure 3.6: Mechanistic proposal for the activation of precatalyst **38** for the catalytic desulfurization of dibenzothiophene.

(2) C–S bond activation and (3) M–C bond hydrogenolysis.

The next two steps in the catalytic desulfurization of dibenzothiophene by **38** are shown in figure **3.7**, starting with nominally dimeric complex **B**. Dative  $\sigma$ -coordination of dibenzothiophene to complex **B** forms complex **E**. The coordination mode depicted is  $\eta^1$ -S mode but aromatic  $\pi$ -coordination modes are possible and may be mechanistically necessary. From complex **E**, the C–S bond activation event could proceed by a single step  $\sigma$ -BM/ $\sigma$ -CAM type mechanism, or by a two-step OA/RE type mechanism; both pathways lead to the biphenylthiolate coordinated complex **H**. The OA/RE could occur at a single metal centre or the process could be bi-metallic. A bimetallic OA/RE event would involve the coordinated thiophene extending across the dimer into the proximity of the second cobalt.  $\eta^1$ -S coordination at one cobalt centre reduces the entropic and, possibly, enthalpic barriers to C–S bond activation at the second cobalt centre. Complex **G** is the intermediate formed from bimetallic oxidative addition. Monometallic oxidative addition of the C–S bond to complex **E** involves  $\alpha$ -carbon migration from sulfur to cobalt to give complex **F**. Similar migrations have been implicated in C–S activation events in other first-row metal systems.<sup>81</sup> Monometallic C–S bond activation likely involves concurrent hydride migration to the other non-participant cobalt atom in order to minimize the energy of the intermediate. The hydride could also be bridging the two cobalt centres at this point. Alternatively, the reductive elimination – bimetallic from **G** or monometallic from **F** – leads to the formation of a new C–H bond and complex **H**. The hydrogenolysis of the first

C–S bond of dibenzothiophene is the first of a number of process that may occur by either  $\sigma$ -BM/ $\sigma$ -CAM type mechanisms, or by bimetallic/monometallic OA/RE pathways. No experimental evidence has been obtained to support one over the other.  $\sigma$ -BM/ $\sigma$ -CAM type mechanisms at a single metal centre look reasonable given that the catalyst is comprised of potentially oxidation-resistant first-row metals. Bimetallic OA/RE pathways appear to be more reasonable than monometallic OA/RE events given that first row metals are better suited to one electron redox-processes.<sup>82</sup>

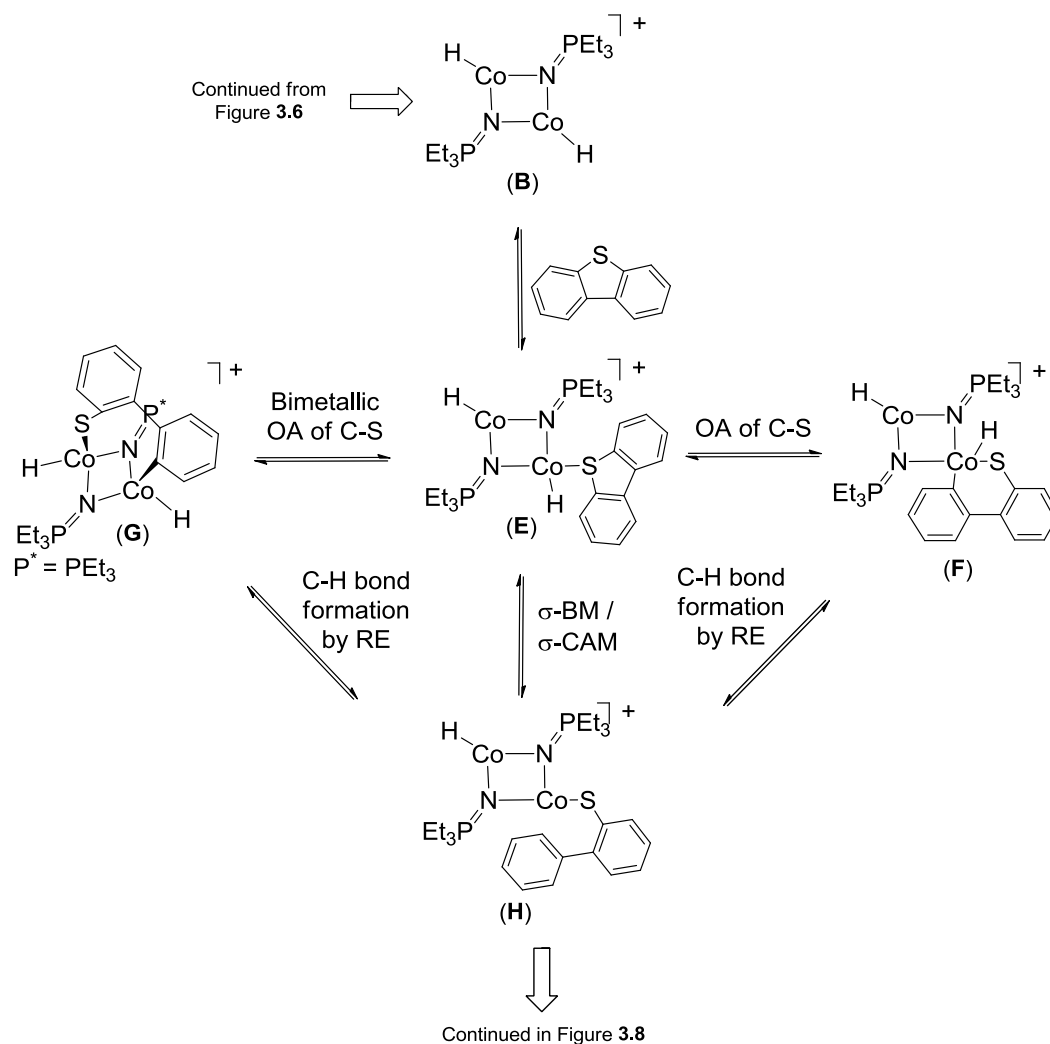


Figure 3.7: Mechanistic proposal for the first C–S bond cleavage and M–C hydrogenolysis events for the catalytic desulfurization of dibenzothiophene by **38**.

(4–6) *Second C–S bond activation, M–C bond hydrogenolysis, and catalyst regeneration.*

Figure 3.8 shows one of many potential mechanisms for the remaining steps in the cycle. Thiolate complex **H** is a branching point in the mechanism (pathways **iii** and **iv**). In pathway (**iii**) the substrate stays bound to the metal for the second C–S bond cleavage and Co–C bond hydrogenolysis events. In pathway (**iv**) the

organosulfur substrate does not remain coordinated throughout the cycle, releasing half-converted thiol into the reaction medium.

The first step in pathway (iii) is C–S bond activation by oxidative addition. This step is almost certainly bimetallic as a monometallic process affords a terminal sulfide; of the numerous reported homogenous metal sulfide complexes related to hydrodesulfurization, only one is terminally bound, requiring a specialized ligand framework to inhibit binuclear bridging.<sup>83</sup> In the oxidative addition product **I**, the sulfur atom is  $\mu_2$ -coordinated to two cobalt centres and the hydrocarbyl fragment – no longer bound to sulfur – coordinates  $\eta^1$ -C to one cobalt centre.

Hydrogenolysis of this bond releases biphenyl and sulfido complex **K**. This process could occur by a  $\sigma$ -BM/ $\sigma$ -CAM or RE/OA mechanism. In this case a  $\sigma$ -BM/ $\sigma$ -CAM type mechanism is likely more facile as the intermediate **J** from RE is likely prohibitively high energy. Complex **K** or related oligomer is the thermodynamic low-point of the cycle. Returning to complex **B** requires the reductive extrusion of the sulfur as  $\text{H}_2\text{S}$ . This part of the cycle is likely rate limiting, and is of highest priority for future mechanistic investigation. The formation of the first S–H bond could occur by heterolytic hydrogenolysis or by OA/RE: both processes lead to thiol **M** which converts to **B** by a final the reductive elimination of  $\text{H}_2\text{S}$ .

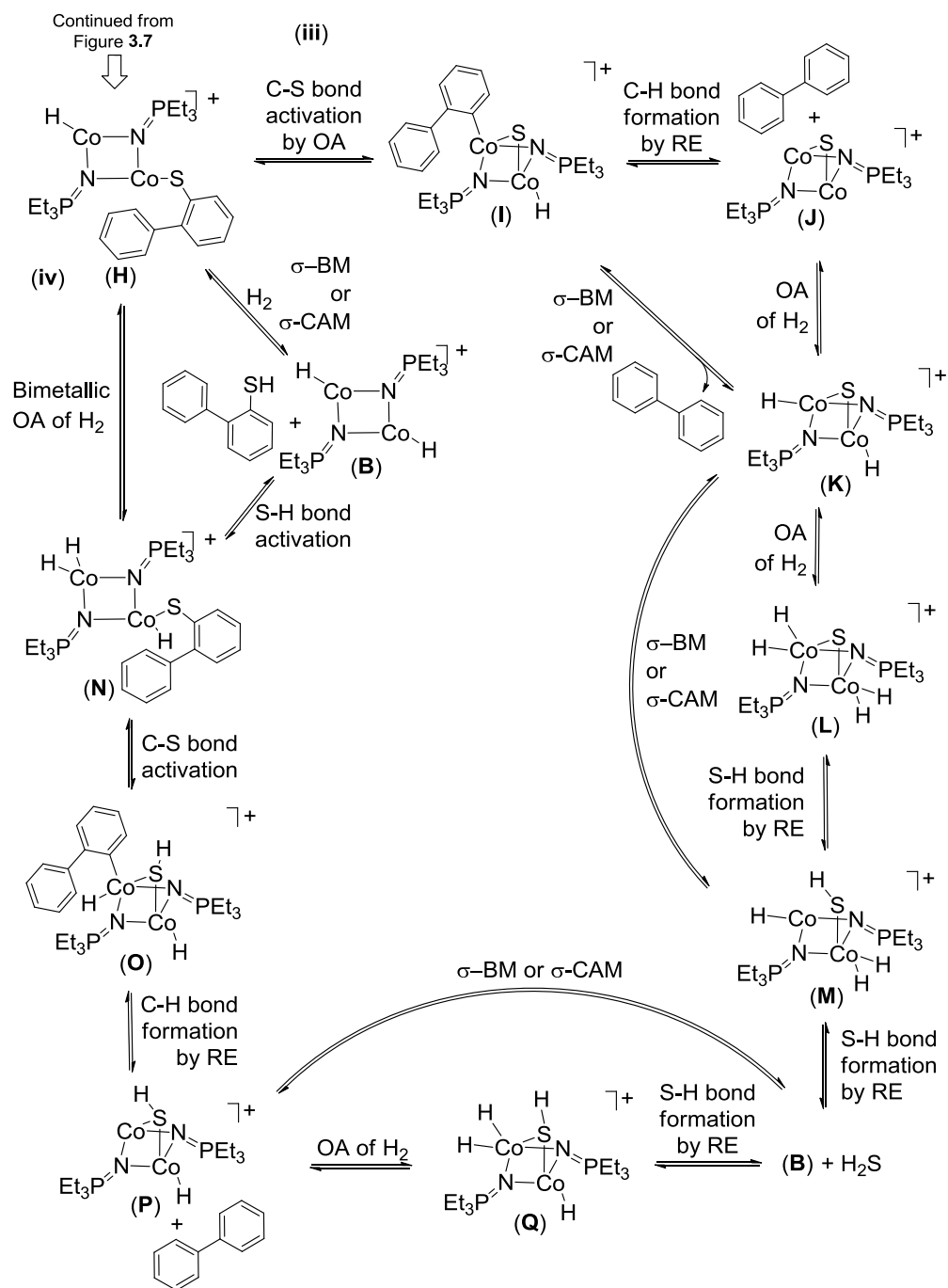


Figure 3.8: Mechanistic proposal for the C–S bond activation, Co–C bond hydrogenolysis, and catalyst regeneration steps of the catalytic desulfurization of dibenzothiophene by [CoMe(NPEt<sub>3</sub>)<sub>4</sub>PF<sub>6</sub>].

Pathway (iv) involves the release of the ‘partially desulfurized’ product biphenyl thiol from **H**. This process is similar to the heterolytic hydrogenolysis described above, occurring either in a single step ( $\sigma$ -CAM/BM) or through a two-step bimetallic or monometallic OA/RE; both processes lead to complex **B**. In order for the thiol to be converted to biphenyl it must be “reload” either by the reverse reaction to form **H**, or by S–H bond activation to give **N**. The second C–S bond activation gives the bridging  $\eta^1$ -S–H complex **O**. Reductive elimination of biphenyl from this complex gives **P**, a relatively stable complex interchangeable with complex **M** under hydrogen. Hydrogenolysis of the Co–S bond of **P/M** again forms H<sub>2</sub>S and **B**.

The mechanism outlined here is enormously simplified yet still highly complicated. Many alternative mechanisms can be proposed. In particular, the addition of dihydrogen to many of the clusters depicted may occur across Co–N bonds; transient H–N phosphoranimine complexes are almost certainly involved in the catalytic process. Issues of catalyst electronic state and nuclearity may require computational methods to resolve. The isolation and *in situ* study of catalytic intermediates, along with kinetic investigations, is expected to clarify the details of the true catalytic cycle.

### *3.2.1.3 Evaluating the catalytic activity of [CoMe(NPEt<sub>3</sub>)<sub>4</sub>]PF<sub>6</sub> at different temperatures*

Reaction temperature is an important variable in catalytic processes; subtle changes in temperatures often have major consequences on catalytic activity. For energy intensive processes like hydrodesulfurization, it is useful to determine the minimum temperature required to support catalytic activity. It is also useful to determine the thermal stability of a catalyst. A series of parallel experiments at different reaction temperatures provide insight into the relationship between TOF and temperature for the desulfurization of dibenzothiophene by precatalyst **38** (Table **3.2**). The experiments are not intended as a detailed kinetic investigation. Instead, they screen a range of temperatures for sustained turnover and provide a rough gauge of catalyst activity as a function of reaction temperature.

Catalytic trials at temperatures below 100 °C give only stoichiometric conversion under one atmosphere hydrogen (entry **1**). Stoichiometric conversion to biphenyl at 90 °C suggests that this temperature is sufficient to promote both C–S bond activation/hydrogenolysis events, but not enough to drive the turnover limiting step – the extrusion of coordinated sulfur from the catalyst. At 110 °C, the process is catalytic (entry **2**). Between 110 and 200 °C the TOF increases in a manner roughly consistent with the ‘rule-of-thumb’: rates increase by a factor of two for every temperature increase of 10 °C (entries **2–7**). The experiments at 180+ °C mark the upper temperature limit for the equipment readily available in our

laboratories – at these temperatures, no signs of catalyst decomposition are observed, although no effort was made to determine this rigorously. We also note that higher temperature reactions were run for progressively shorter reaction times, in order to avoid reactions going to completion. The mixed-valence cluster **38** was expected to be thermally robust – removing an electron from **30** serves to strengthen the already formidable N–Co bonding interactions – but the self-consistency of the temperature data is surprising. The stability of the supporting phosphoramidate ligands is less surprising: the phosphorus centres are formally phosphorus(V) and the nitrogen atoms are coordinatively saturated. True to form, the halide precursor  $[\text{CoCl}(\text{NPEt}_3)]_4$  can be prepared under melt conditions at temperatures above 200 °C.<sup>2</sup>

Table 3.2: Rate as a function of reaction temperature for the desulfurization of dibenzothiophene with  $[\text{CoMe}(\text{NPEt}_3)]_4\text{PF}_6$ .<sup>a</sup>

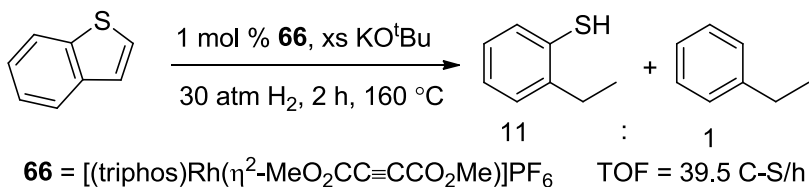
Entry	Temp (°C)	Time (min)	TOF <sup>b</sup> (h <sup>-1</sup> )
1	90	120	0
2	110	150	96.3
3	130	60	242.9
4	150	40	448.6
5	165	30	1109.1
6	182	12	3104.4
7	200	7	7685.3

<sup>a</sup>All experiments were conducted in sealable medium-walled glass vessels charged with 1 atm H<sub>2</sub> at 25 °C and excess KH, followed by immersion in a thermostat-regulated oil bath at the given temperature. TOF are single point determinations, taken at the end of the indicated reaction period.

<sup>b</sup>C–S bond cleavages per mol of cluster per hour, as determined from product distributions by GC-MS.

### 3.2.1.4 The role of scavengers in desulfurization reactions catalyzed by $[\text{CoMe}(\text{NPEt}_3)_4]\text{PF}_6$

Strong bases are used in laboratory scale homogeneous catalytic hydro-desulfurization experiments to facilitate the reductive conversion of low-energy sulfided intermediates back into high energy unsaturated intermediates capable of activating C–S bonds. One example is the conversion of benzothiophene into ethyl benzene thiol by  $[(\text{triphos})\text{Rh}(\eta^2\text{-MeO}_2\text{CC}\equiv\text{CCO}_2\text{Me})]\text{PF}_6$  (**66**) which proceeds catalytically in the presence of potassium tert-butoxide (Eqn. 3.7).<sup>84</sup>



Eqn. 3.7

Spectroscopic and kinetic evidence suggest that the reductive elimination of ethyl benzene thiol from  $[(\text{triphos})\text{Rh}(\eta^1\text{-S}(\text{C}_8\text{H}_9)\text{H}_2)]$  is the rate limiting step for this cycle. Under basic conditions, the product thiol is rapidly deprotonated to ethylbenzenethiolate, which shifts the product-forming equilibrium in favour of reductive elimination. A number of strong bases ( $\text{KO}^t\text{Bu}$ ,  $\text{NaOMe}$ ,  $\text{KOH}$ ) can be used as scavengers in this system with little effect on rates.

The desulfurization of dibenzothiophene by **38** is also facilitated by strongly basic agents. In the absence of basic agents, reactions between precatalyst **38** and dibenzothiophene under hydrogen are strictly stoichiometric – at least under the

mild conditions employed to date. Unlike the example above, the TOF for the desulfurization of dibenzothiophene catalyzed by **38** is affected by the type of base employed (Table **3.3**). Under the conditions evaluated, insoluble alkoxide bases do not induce catalytic dibenzothiophene desulfurization (entries **1** and **2**). Catalytic turnover is observed upon the inclusion of the secondary amide bases lithium/potassium diisopropylamide (LDA/KDA), which are also more soluble. In the presence of LDA the reaction proceeds slowly, but catalytically, at a rate of 0.71 C–S cleavages per hour over 16 h (entry **3**). In the presence of KDA, the reaction proceeds at 32.7 C–S cleavages per hour (entry **4**). A similar effect is noted for the sterically more imposing secondary 2,2,6,6-tetramethylpiperidide anions (LiTMP/KTMP). In the presence of LiTMP, the desulfurization occurs slowly, proceeding at less than one C–S cleavage per hour (entry **5**), while the presence of KTMP results in more than 75 C–S bond cleavages per hour (entry **6**). By far the fastest rate, however, is obtained using a suspension of potassium hydride (entry **8**). In the presence of sodium hydride, the reaction does not proceed catalytically (Entry **7**).

Table 3.3: Alternative scavengers for the catalytic desulfurization of dibenzothiophene by  $[\text{CoMe}(\text{NPEt}_3)]_4\text{PF}_6$ .

Entry	Scavenger	Time (h)	TOF <sup>b</sup> (h <sup>-1</sup> )
1	NaO <sup>t</sup> Bu	16	s
2	KO <sup>t</sup> Bu	16	s
3	LDA	16	0.71
4	KDA	16	32.73
5	LTMP	16	0.55
6	KTMP	16	75.5
7	NaH	16	s
8	KH	0.4	310 <sup>c</sup>

<sup>a</sup>All experiments were conducted in sealable medium-walled glass vessels charged with 1 atm H<sub>2</sub> at 25 °C and five equivalents of the appropriate scavenger, followed by immersion in a thermostat-regulated oil bath at the given temperature.

<sup>b</sup>C–S bond cleavages per mol of cluster per hour over the 16 h reaction period, as determined from product distributions by GC-MS. Single point TOF determination.

<sup>c</sup>Rxn proceed to completion, calculated TOF is considered a minimum.

Three trends are apparent from the experiments summarized in Table 3.3: [1] stronger bases result in greater catalytic activity, [2] potassium-based scavengers afford higher TOF's than obtained using a lighter alkali metal, and [3] potassium hydride is markedly more effective than any other scavenger evaluated. Given the current lack of mechanistic details, it is difficult to comment on how, exactly, the basic agents are effecting the catalytic desulfurization of dibenzothiophene by **38**, but the scavenger is clearly driving the hydrogenolysis of the sulfido-bridged intermediate.

The hydride reagents in this series are unique as none are soluble under the reaction conditions. The hydrides of group I metals possess NaCl-type crystal

structures and their reactions typically proceed at the crystal surface.<sup>85</sup> Enhanced reactivity with potassium hydride relative to the lighter primary hydrides has been observed in many applications, including acid-base reactions with protic nitrogen, sulfur, and oxygen species, which are of particular relevance here.<sup>86</sup> The effect is attributed to the decreasing trend in M–H crystal lattice energy moving down Group I: the ‘apparent hydride ion radius’ in the crystals increases from NaH to KH.<sup>87</sup> It is likely that some crystal lattice/surface effects cause the clear improvement in rates when potassium hydride is used as scavenger for the desulfurization of dibenzothiophene by **38**.

Among the soluble bases evaluated, basicity increases in the order:  $^-\text{O}^t\text{Bu} < ^-\text{N}(\text{iPr})_2 < ^-\text{TMP}$ . (In THF, the pKa’s of tertbutanol, diisopropylamine, and 2,2,6,6-tetramethylpiperidine are 17.3, 35.7, and 37.3, respectively<sup>88</sup>). The steric profile of the reagents increase in the same order. It is difficult to separate these effects, as well as those associated with the heightened reactivity of potassium analogs in this series. The solution phase chemistry of secondary amide bases is notoriously complex, primarily due to highly variable aggregation behaviour. Both LDA and LiTMP form aggregates ranging from monomers to hexamers in solution and aggregation equilibria often dictate reaction rates.<sup>89,88</sup> The aggregation of the potassium coordinated secondary amides is equally complex. In general, lithium and potassium amides show similar aggregation states in the same solvent systems, but much different affinities for solvent coordination.<sup>90</sup>

Overall, the complexities associated with scavenging – heterogeneous reaction sites and complex aggregation equilibria – are troublesome, and the necessity for inclusion limits the utility of complex **38** as a reductive catalyst. The development of ‘scavenger free’ conditions for catalytic desulfurization using **38** and related catalysts is the single most important pursuit for those currently working on this system. The thermally robust nature of mixed valence **38** is critical in this respect. The extrusion of sulfur from the catalyst as H<sub>2</sub>S will likely require more forcing reaction conditions, in terms of temperature and hydrogen concentration. The potential to customize more sophisticated reactor designs and authentically heterogeneous analogues, through collaborations with chemical/process engineers within the Centre for Oilsands Innovation, is very exciting.

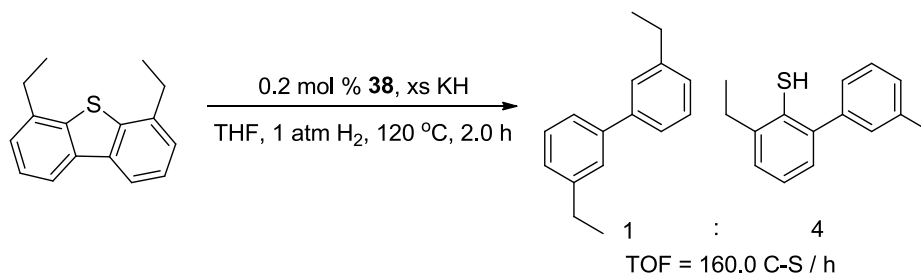
### *3.2.2 Substrate scope for catalytic desulfurization with [CoMe(NPEt<sub>3</sub>)<sub>4</sub>PF<sub>6</sub>]*

The cationic cluster **38** catalyzes the hydrodesulfurization of other organosulfur compounds that model structures prevalent in heavy crude oils. The results shown below are ‘semi-optimized’: reaction temperature and time were adjusted to allow single-point TOF’s to be determined, providing a qualitative assessment of relative reactivity under similar reactor conditions.

#### *3.2.2.1 “Ultra-deep” HDS: 4,6-diethyldibenzothiophene*

Alkylated dibenzothiophenes, especially those substituted in the 4,6-positions model the most recalcitrant organosulfur compounds present in crude oils.<sup>78</sup> For

this reason they are treated as ‘gold-standard substrates’ for HDS catalyst evaluations. To date, the catalytic hydrodesulfurization of a 4,6-dialkyldibenzothiophene substrate has not been reported in the literature. Indeed, even coordination complexes featuring 4,6-dialkyldibenzothiophenes are very rare.<sup>91</sup> Cluster **38**, however, catalyzes the desulfurization of 4,6-diethyldibenzothiophene under mild conditions. Heating a THF slurry of 4,6-diethyldibenzothiophene, precatalyst **38**, and excess potassium hydride under one atm of hydrogen at 120 °C affords a mixture of partially desulfurized and fully desulfurized products after two hours (Eqn. **3.8**). The TOF at this point is 160 C–S cleavages per hour, a remarkably rapid conversion just above the threshold temperature. Dibenzothiophene is desulfurized faster under equivalent conditions, as is expected, given the sterically encumbered “refractory” character of 4,6-diethyldibenzothiophene. The ratio of partially to fully desulfurized product is about 4 : 1. This is the reverse of the selectivity observed in the desulfurization of dibenzothiophene. This may be due to a catalytic pathway similar to (iii) in Figure **3.8**, where the substrate dissociates from the catalyst after the first C–S bond cleavage. Competitive scavenging of the half-reacted thiolate may be responsible for the slow subsequent hydrodesulfurization.

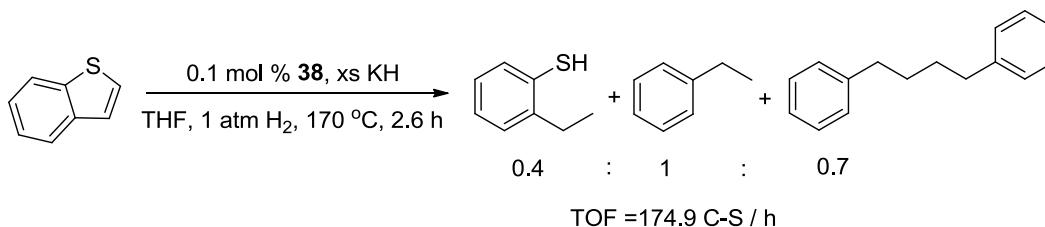


Eqn. **3.8**

### 3.2.2.2 HDS of benzothiophene

A handful of metal complexes are capable of activating the C–S bonds of benzothiophene, although homogeneous catalytic hydrodesulfurization is unknown.<sup>92</sup> Typically, insertion into the vinyl C–S bond is more facile than insertion into the aryl C–S bond, although some systems show reverse selectivity.<sup>93</sup> Molecular orbital calculations suggest that the selectivity is governed primarily by steric interactions between the metal complex and the heterocycle and the M–C bond strength of the resulting thiametallacycle, rather than the binding mode of the substrate.<sup>94</sup> A THF slurry of benzothiophene, precatalyst **38**, and KH under one atm of hydrogen at 170 °C affords a mixture of partially desulfurized and fully desulfurized products after 2.6 hours (Eqn. **3.9**). The TOF is 175 C–S cleavages per hour. At lower temperatures, catalytic desulfurization is not observed. This is more than a little surprising given that the desulfurization of more refractory organosulfur compounds proceeds readily at lower temperatures in this system. Higher reactivity towards dibenzothiophene than benzothiophene has been noted in other late-metal systems.<sup>81</sup> The presence of 2-ethylbenzenethiol as the only partially desulfurized product implies that activation of the vinyl C–S bond of benzothiophene is more facile than activation of the aryl C–S bond, in accord with the majority of examples. The presence of coupling product 1,4-diphenylbutane is curious, and the route to its formation is not yet known. Curtis has seen coupling products associated with homolytic C–S bond cleavage in the stoichiometric desulfurization of a number of alkyl and aryl thiols by the

Co<sub>2</sub>Mo<sub>2</sub>S<sub>3</sub> butterfly complex.<sup>95</sup> The coupling product could result from the reductive elimination, but this would require one cluster simultaneously executing the desulfurization of two substrates.

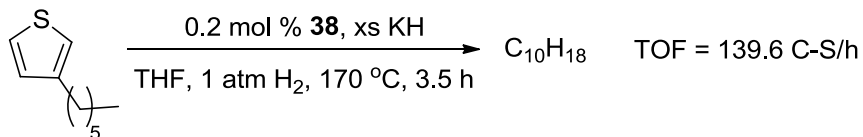


Eqn. 3.9

### 3.2.2.3 HDS of 3-hexylthiophene

Alkylated thiophene derivatives are often used in the place of thiophene as desulfurization substrates because the hydrocarbons that result from the desulfurization are not gaseous at room temperature. In the event, hydrodesulfurization of 3-hexylthiophene under standard conditions and 170 °C affords a single C<sub>10</sub>H<sub>18</sub> hydrocarbon product at a TOF of 139.6 C–S cleavages per hour after 3.5 h (Eqn. 3.10). The hydrocarbon is presumably 2-hexyl-1,3-butadiene. Trials at lower temperatures again show no desulfurization activity. The reason for the suppressed reactivity of **38** towards thiophene is also not well understood. One possibility is that η<sup>6</sup>-coordination to the face of an hydrocarbon aromatic ring is an important bonding motif for **38**, which would suggest

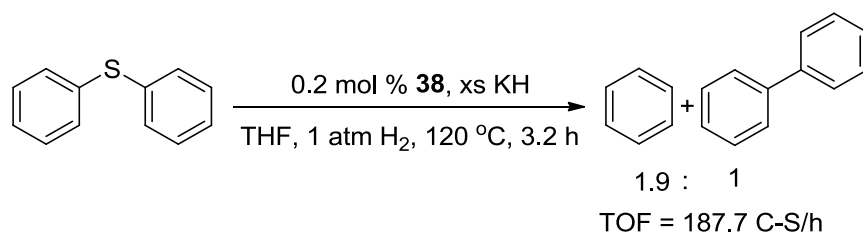
bimetallic cooperativity may be critical in this system. Another possibility is that the dative S–Co bond is stronger in this case, and inhibits the formation of any  $\pi$ -bound intermediates.



Eqn. **3.10**

#### 3.2.2.4 HDS of diphenyl sulfide

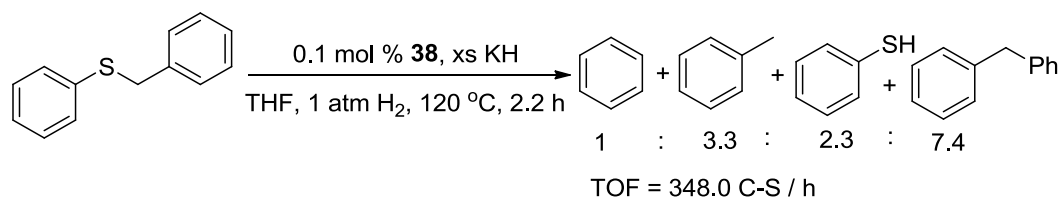
Non-thiophenic organosulfur compounds are not often used as hydrodesulfurization substrates for the evaluation of homogeneous catalytic systems, presumably because current catalyst technologies desulfurize nonaromatic organosulfides efficiently. Diphenyl sulfide is less refractory than the thiophenic derivatives discussed above. The HDS of diphenyl sulphide proceeds at 120 °C and affords a 1.9 : 1 mixture of benzene and, surprisingly, *biphenyl* after 3.2 hours (Eqn. **3.11**). The TOF at this point in the reaction is 188 C–S cleavages per hour. The formation of biphenyl suggests a mechanism where both C–S bond cleavages occur without dissociation of a thiol intermediate: two consecutive C–S bond activation reactions form a sulfided-metal cluster that reductively eliminates biphenyl.



Eqn. 3.11

### 3.2.2.5 HDS of benzyl phenyl sulfide

Benzyl phenyl sulfide is an interesting substrate for hydrodesulfurization trials because it has both an  $sp^2$  C–S bond and a resonance-weakened  $sp^3$  C–S bond. Hydrodesulfurization of benzyl phenyl sulfide at 120 °C affords a mixture of fully and partially desulfurized products after 2.2 hours (Eqn. 3.12). At this point in the reaction, the TOF is 348 C–S cleavages per hour. The presence of phenyl thiol as the only partial-desulfurization product implies that benzylic  $sp^3$  C–S bond cleavage is more facile than  $sp^2$  C–S bond cleavage in this system, as might be expected from standard bond enthalpies. The major product in the mixture, however, is diphenylmethane. This product – like that noted above – may result from a mechanism during which both C–S cleavage events occur prior to dissociation of either hydrocarbon fragment. The absence of the alternative coupling products, 1,2-diphenylethane and biphenyl suggest that coupling events are occurring on the cluster and not as organic radicals in solution, and that only one substrate at a time is processed by the cluster.

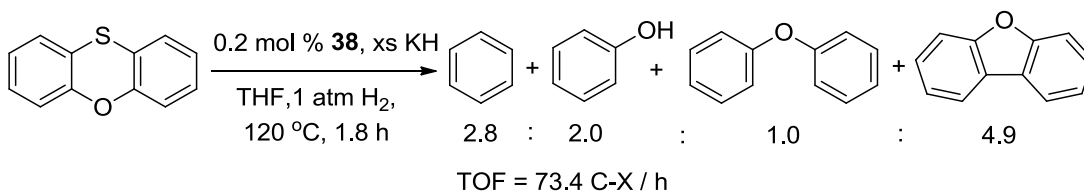


Eqn. **3.12**

### 3.2.2.6 C–O and C–S hydrogenolysis in phenoxathiin

Substrates that contain both oxygen and sulfur atoms in a single ring – like phenoxathiin – are not of direct relevance the hydrotreatment of crude petroleum. Nonetheless phenoxathiin is an interesting substrate for reductive catalysis because it provides insight into selectivity towards C–S/C–O bonds. Complex **38** catalyzes both C–S and C–O bond hydrogenolysis in phenoxathiin. The reaction of phenoxathiin and **38** affords a mixture of products – benzene, phenol, diphenyl ether and dibenzofuran – after 1.8 hours at 120 °C (Eqn. **3.13**). At that point the turnover frequency is 73.4 C–X / h. The products observed indicate a strong preference for C–S bond cleavage over C–O bond cleavage, in accord with relative bond strengths of aryl ethers and thioethers; the bond dissociation energy for the aromatic C–S bond of thioanisole is 76 kcal/mol,<sup>77</sup> and the bond dissociation energy of the C–O bond in anisole is 110 kcal/mol.<sup>96</sup> As is discussed in the preceding chapter, systems that mediate aromatic C–O bond hydrogenolysis are rare. This reaction is remarkable given that it is catalytic under mild conditions and at low catalyst loading. With the exception of dibenzofuran, all the products are anticipated. Dibenzofuran is presumably formed by two C–S bond

hydrogenolysis events followed by reductive coupling at the cluster centre. The reductive coupling observed with phenoxathiin, and other substrates, suggest that **38** may also find utility as a catalyst for coupling reactions.



Eqn. **3.13**

### 3.3 Conclusions

The mixed-valence complex **38** is a precatalyst for hydrodesulfurization under mild conditions. HDS reactions with **38** proceed at catalyst loadings below one mol %, and afford impressive turnover frequencies. The desulfurization of dibenzothiophene has been studied in some detail. Control experiments indicate that: KH and CoS are not active catalysts under the reaction conditions employed, hydrogen is the active reductant for the desulfurization of dibenzothiophene by **38**, and that the active catalyst for the process is homogenous.

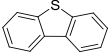
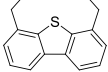
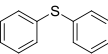
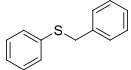
The mechanism(s) for the desulfurization of dibenzothiophene by **38** are complex and not well understood. A preliminary mechanistic proposal has been put forth to provide a ‘road map’ to guide future work. The desulfurization of dibenzothiophene by **38** has been screened over a range of temperatures. Reaction

temperatures below 100 °C afford no sustained catalytic activity. Single-point turn over frequencies increase between 110 °C and 180 °C. The upper limit for catalytic activity (*i.e.* catalyst thermal decomposition temperature) is above the temperature range accessible with the equipment in our laboratories.

A number of alternative scavengers have been evaluated for the desulfurization of dibenzothiophene by **38**. Among the scavengers tested, stronger bases induce higher catalytic rates. Potassium based scavengers are more effective than lithium/sodium based scavengers. The complexities associated with scavenging – heterogeneous reaction sites and complex aggregation equilibria are troublesome and the necessity for inclusion limits the utility of **38** as a reductive catalyst. The development of scavenger free conditions for catalytic desulfurization using **38** and related catalysts is the single most important pursuit for those currently working on this system.

A brief HDS substrate scope investigation has been completed with complex **38** (Table **3.4**). Refractory thiophenic derivatives (4,6-diethyldibenzothiophene, benzothiophene, 3-hexylthiophene) are all desulfurized by **38** under mild conditions. Less refractory organosulfur compounds (diphenyl thiol, benzyl phenyl thiol, and phenoxathiin) are also catalytically desulfurized by **38** under mild conditions. Experiments with phenoxathiin imply that compound **38** also catalyzes C–O bond hydrogenolysis. More detailed investigations of C–O bond hydrogenolysis with **38** are the topic of the next chapter.

Table 3.4. Summary of catalytic hydrodesulfurization of organosulfur moieties common in crude petroleum feedstocks by  $[\text{CoMe}(\text{NPEt}_3)]_4\text{PF}_6$ .<sup>a</sup>

Entry	Substrate	[Cat] (mol %)	Time (h)	Temp (°C)	Conversion (%)		TOF <sup>b</sup>
					C <sub>n</sub> H <sub>m</sub>	ArSH	
1		0.2	1.0	150	67.6	0.0	448.6
2		0.2	2.0	120	8.5	35.2	160.0
3		0.1	2.6	170	44.0	7.7	174.9
4		0.2	3.5	170	53.7	0.0	139.6
5		0.2	3.2	120	78.8	0.0	187.7
6		0.1	2.2	120	63.0	12.5	348.0

<sup>a</sup>All experiments were conducted in sealable medium-walled glass vessels charged with 1 atm H<sub>2</sub> at 25 °C and excess KH, followed by immersion in a thermostat-regulated oil bath at the given temperature.

<sup>b</sup>C–S bond cleavages per mol of cluster per hour, as determined from product distributions by GC-MS analysis

## ***4. Towards efficient catalysts for lignin-valorization: Mixed-valence cluster catalysts for C–O bond hydrogenolysis***

### *4.1 Introduction and background*

#### *4.1.1 Lignin valorization*

The need to replace fossil reserves as the primary source of transportation fuels, energy, and chemicals has never been greater. While multiple renewable resources – solar, wind, hydro, *ect.* – are poised to contribute to sustainable fuels and energy production, sustainable bulk chemical production hinges on a single resource: biomass.<sup>viii</sup> As the only terrestrial source of renewable carbon feedstock, biomass is rapidly gaining favor as a source for commodity chemicals.

Canada is well situated for a transition to renewable feedstocks for bulk chemical production. Forested and agricultural lands represent almost fifty percent of Canada's total land-area, more than 4.85 million km<sup>2</sup>.<sup>97</sup> This land supports agricultural and forestry industries that generate enormous amounts of waste; of the 66 million tonnes of biomass added yearly to residual (*i.e.* waste) stream, about 60 million tonnes may be considered available feedstock for Canada's nascent bio-economy.<sup>97</sup>

In both North America and Europe, governments are mandating increasing incorporation of renewable feedstocks into chemical production routes. For example, the Dutch Ministry of Economic Affairs intends to have as much as 45

---

<sup>viii</sup> The term “biomass” refers to any plant derived organic matter available on a renewable basis, including dedicated energy crops and trees, agricultural crops and residues, forestry products and residues, aquatic plants, animal wastes, municipal wastes, and other waste materials.<sup>147</sup>

% of fossil-based raw materials for chemical production substituted by biomass before 2040.<sup>98</sup> The U.S Department of Energy intends to derive upwards of 25% of U.S. chemical commodities from biomass by 2030.<sup>99</sup> Meeting these aggressive mandates will require the development of biomass-to-chemicals conversion processes that are both energy and cost efficient.

The conversion of lignin into value added products (lignin valorization) is a key component of biomass conversion enterprises. Lignin is a nearly ideal potential source of the ubiquitous bulk aromatic chemicals benzene, toluene, and xylenes (BTX). These commodity chemicals are used on industrial scale as solvents and bulk chemicals precursors; benzene, toluene, and xylenes are platform chemicals for a large portion of the petrochemical industry.<sup>ix</sup> Thus, lignin-to-BTX conversion processes potentially provide a means to unite well established petrochemical processes with renewable feedstocks.

Lignin is an amorphous three-dimensional organic resin that adds structural integrity to lignocellulose – an important component of plant cell-walls.<sup>100</sup> Lignin is the second most abundant naturally-derived polymer on the planet; because it does not play an intrinsic role in the food chain, its utilization as a renewable chemical feedstock does not threaten food security.<sup>101</sup> Indeed, lignin is widely treated as a waste product. Pulp and paper industries expend considerable capital removing lignin from product streams, only to burn it on-site as a low grade heating fuel. Only about two percent is used to source high value products.<sup>102</sup>

---

<sup>ix</sup> In 2005 the U.S. demand for BTX was  $45.3 \times 10^9$  lb.<sup>103</sup>

At the molecular level, lignin is a unique bio-polymer because of its highly aromatic nature. Lignin is composed of monomeric phenylpropenyl (C<sub>9</sub>) units, randomly connected through C–C and C–O bonds.<sup>103</sup> Although there is still considerable debate in the literature regarding specific pathways, lignin is widely believed to be produced by enzymatic dehydrogenative polymerization of three related alcohols – *p*-coumaryl, coniferyl, and sinapyl alcohols (Figure 4.1).<sup>102</sup> Thus, while lignin composition varies among and between woods/plants, the prominent polymer linkages are similar from source to source.

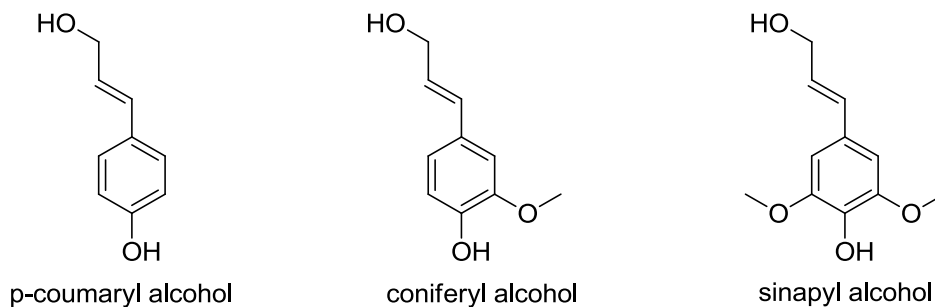


Figure 4.1: Three aromatic alcohols lignin that are used as precursors in naturally occurring lignin synthesis by enzymatic dehydrogenative polymerization.<sup>102</sup>

Valorizing lignin requires breaking the tethers that link the monomeric aromatics. There are seven common linkages:  $\beta$ -O-4, 5-5,  $\beta$ -5, 4-O-5,  $\beta$ -1,  $\beta$ - $\beta$ , and dibenzodioxocin.<sup>102</sup> Each linkage is highlighted in the schematic representation of a softwood lignin shown in Figure 4.2. Of the seven linkages, the  $\beta$ -O-4 linkage is the most abundant.<sup>104</sup> Often  $\beta$ -O-4 linkages are disrupted during pulping procedures, so processed lignins are typically lower molecular weight fragments with multiple phenolic components. Like the  $\beta$ -O-4 linkage, the dibenzodioxocin linkage features both aromatic and aliphatic C–O bonds. The 4-O-5 linkage is a

diaryl ether moiety that is typically involved in polymer cross-linking.<sup>105</sup> The 5-5,  $\beta$ -1,  $\beta$ - $\beta$  and  $\beta$ -5 linkages all involve C–C bonds. Relative to the carbon-oxygen based linkages, these linkages are much less abundant, and they are more difficult to cleave.<sup>102</sup>

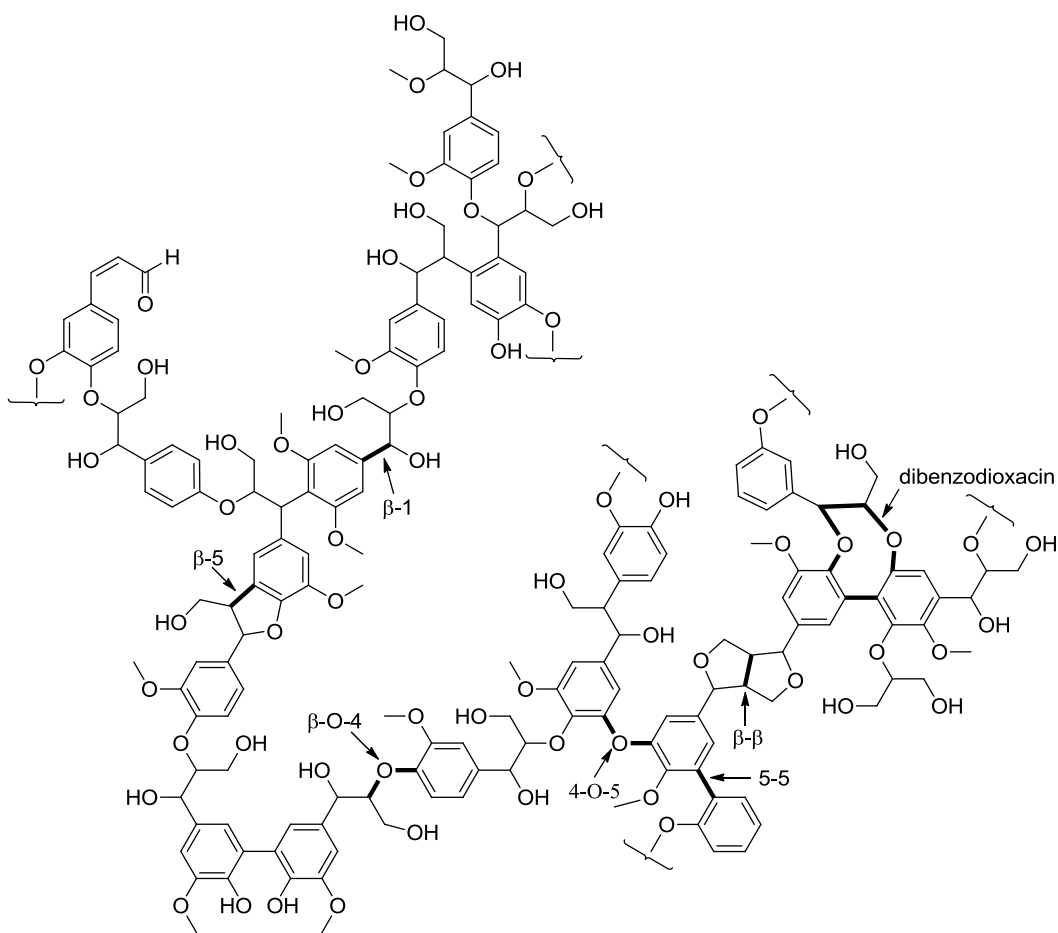


Figure 4.2: Schematic representation of a softwood lignin. Prominent linkages are bold-faced.<sup>105</sup>

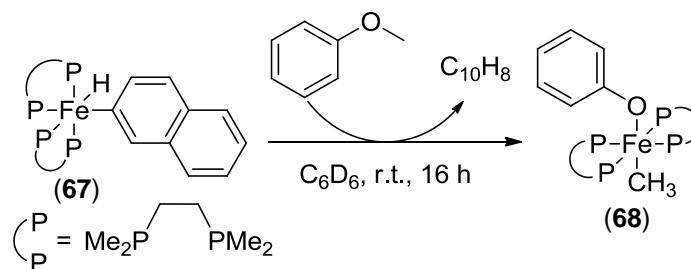
Catalysis is a key enabling technology for lignin valorization. Process for lignin-to-BTX conversion require catalysts that are simultaneously aggressive towards reductive hydrogenolysis yet inert towards aromatic hydrogenation. Current

lignin-refining catalysts are limited by their heterogeneous nature, requiring harsh reaction conditions ( $\geq 250$  °C, 35 atm H<sub>2</sub>) that result in char formation, low yields, and undesirable aromatic ring hydrogenations.<sup>106</sup> Optimal catalysts will afford high conversions to unfunctionalized bulk aromatics under mild conditions by reductive side-chain scission. Much progress has recently been made towards this end using homogeneous systems.

#### 4.1.2 C–O bond hydrogenolysis in homogeneous systems

Relative to the extensive literature related to HDS and C–S bond activation, the literature related to C–O bond activation chemistry is quite modest. Nonetheless, the progress towards catalytic systems for C–O bond hydrogenolysis under mild conditions is considerable; complexes of both early and late metals have been reported to activate unstrained C–O bonds, stoichiometric C–O hydrogenolysis reactions with late 2<sup>nd</sup> and 3<sup>rd</sup> row metals are well precedented, and at least two systems have been reported to effect catalytic C–O bond hydrogenolysis, albeit with limited success. Interestingly, trends are starting to emerge related to selectivity between sp<sup>2</sup> and sp<sup>3</sup> C–O bond cleavage, but systems that cleave both linkages are elusive. More promiscuous catalytic systems for C–O bond hydrogenolysis are critical for applications to lignin valorization where both types of bond cleavages are essential to affect *tandem* depolymerization and upgrading to BTX.

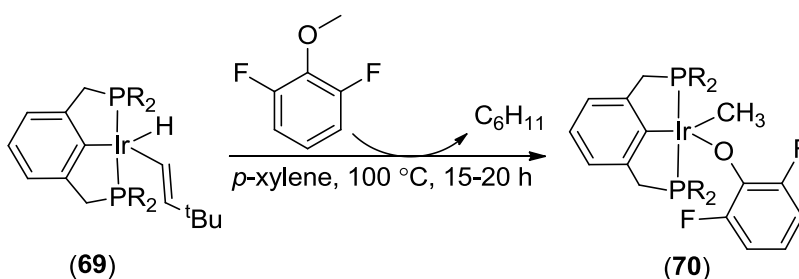
One early C–O bond activation report involves the *in situ* formation and reaction of the electron-rich iron(0) intermediate  $\text{Fe}(\text{dmpe})_2$  ( $\text{dmpe} = \text{Me}_2\text{PCH}_2\text{CH}_2\text{PMe}_2$ ) (Eqn. 4.1).<sup>107</sup> The reaction of the iron(II) complex **67** with anisole proceeds at room temperature, leading to exclusive formation of methyliron phenoxide complex **68**, presumably via reductive elimination/oxidative scission pathway. The phenoxy and methyl ligands were identified by NMR spectroscopy but the product was not isolated or fully characterized. Although the authors do not speculate on the process, the reaction probably proceeds by an  $\text{S}_{\text{N}}2$ -type nucleophilic attack of the electron rich  $\text{Fe}(0)$  centre on the weakly electrophilic anisole methyl group.<sup>108</sup> Precoordination to oxygen or aromatic system could assist this process, although no evidence for this was obtained.



Eqn. 4.1

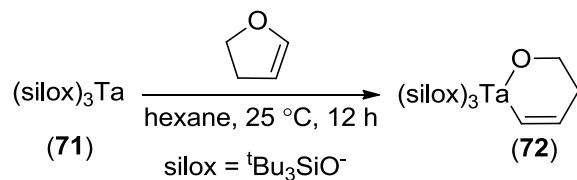
The iridium pincer complex **69** exhibits a similar preference for  $\text{sp}^3$  C–O bond cleavage; the complex activates a variety of fluorine-substituted aryl alkyl ethers exclusively at the alkyl carbon-oxygen linkage, although no reactivity is observed towards anisole derivatives that lack electron withdrawing fluoride substituents (Eqn. 4.2).<sup>108</sup> For example, prolonged heating of complex **69** and 2,6-

difluoroanisole affords methyliridium(III) phenoxide complex **70**. DFT computations and mechanistic studies indicate that the reaction does not proceed by direct C–O bond activation. Instead, the iridium centre inserts into a methyl C–H bond, followed by  $\alpha$ -aryloxy migration and subsequent hydride migration give the observed product. This system has been studied in greater detail than the others discussed here; it is possible that C–H activation events are involved in other C–O bond activation processes.



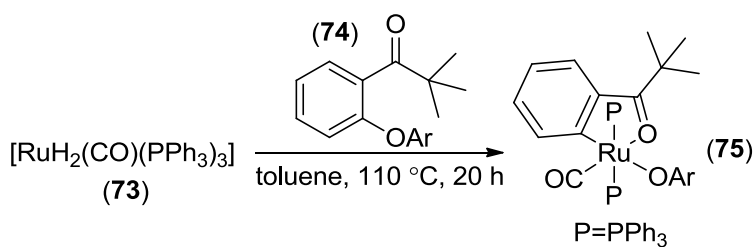
Eqn. 4.2

In contrast to the two examples above, the early metal complex  $\text{Ta}(\text{silox})_3$  (silox =  ${}^t\text{Bu}_3\text{SiO}$ ) **71** selectively activates the  $\text{sp}^2$  C–O bonds in aryl ethers (Eqn. 4.3).<sup>109</sup> The reaction of **71** with excess 1,2-dihydrofuran at room temperature affords the oxo-metallacycle **72** in 52 % yield. The position of the C=C double bond – as determined by NMR spectroscopy – is indicative of a nucleophilic attack at the LUMO of the vinyl ether, rather than the saturated O–CH<sub>2</sub>R linkage. This is almost certainly assisted by coordination of the metal to the oxygen of the ring.



Eqn. 4.3

The ruthenium(II) complex **73** is also capable of  $sp^2$  C–O bond cleavage (Eqn. 4.4).<sup>110</sup> Thermolysis of dihydride **73** and the acylated diaryl ether **74** results in selective insertion of the ruthenium centre into the acylated aryl C–O bond to give a chelated  $\sigma$ -aryl complex **75**. The X-ray structure of complex **75** shows that the aryloxy fragment is situated *trans* to the aryl carbon of the pivalophenone moiety. The authors suggest the *trans*-relationship is derived from the weaker *trans* influence of the aryloxy ligand compared to the CO ligand, driving the rearrangement of a kinetically-formed *cis*-adduct.

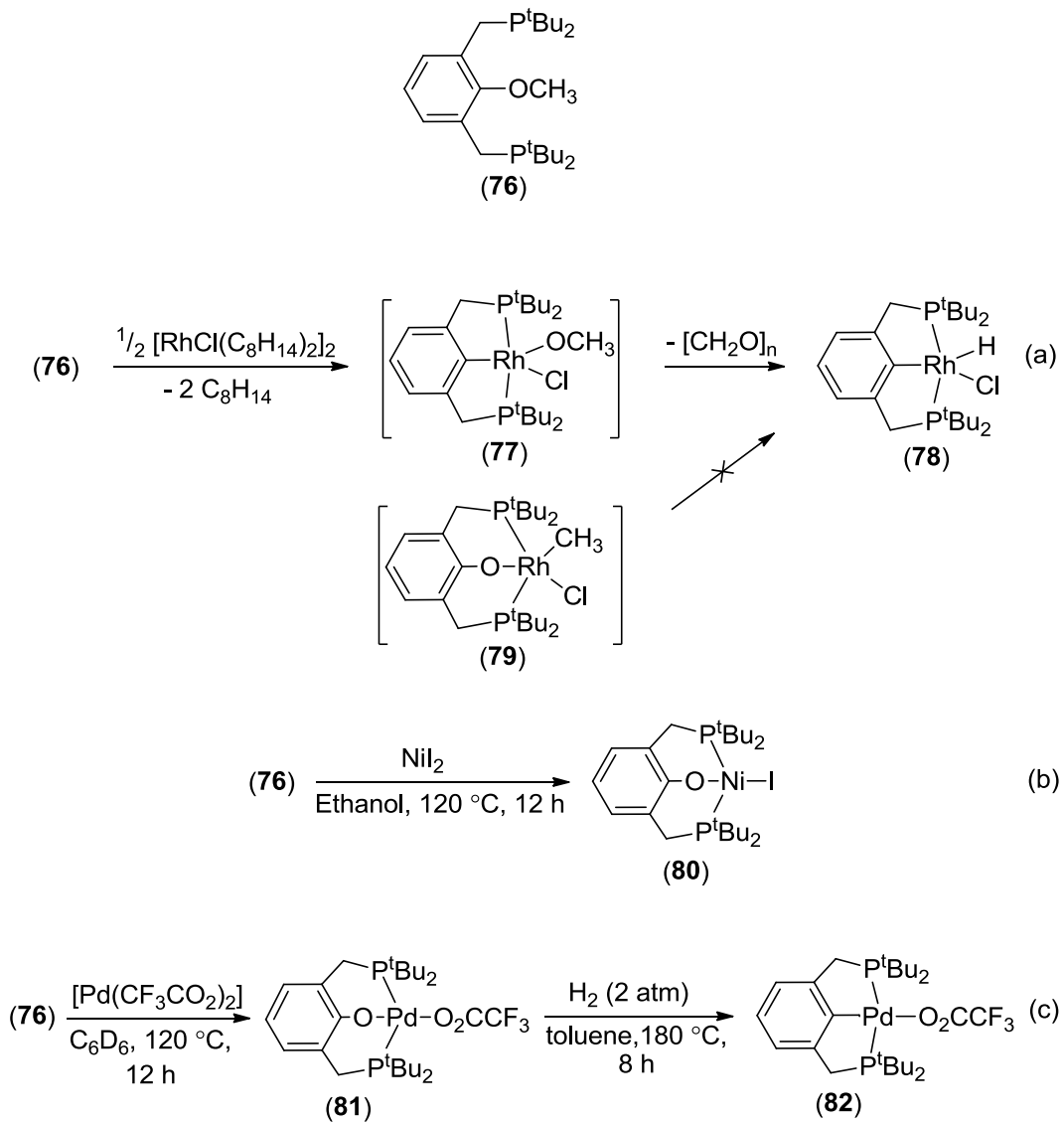


Eqn. 4.4

A series of experiments featuring the bisphosphine pincer-decorated alkyl aryl ether **76** highlights the influence of the metal precursor on the regioselectivity of C–O bond activation (Scheme 4.1).<sup>111</sup> Heating the ligand and the rhodium(I)

precursor  $[\text{RhCl}(\text{C}_8\text{H}_{14})_2]_2$  results in quantitative formation of the known Rh(III) hydrido halide complex **78** (Scheme. **4.1a**). The authors propose that the transformation proceeds from an intermediate Rh(III)–OCH<sub>3</sub> complex **77**, which readily undergoes  $\beta$ -hydride elimination to give **78** and formaldehyde. The authors independently prepared the related phenoxy complex **79** to confirm that ArO–CH<sub>3</sub> bond activation is not involved in the transformation.

In contrast to the  $\text{sp}^2$  C–O selectivity observed with rhodium(I), nickel(II) selectively cleaves the  $\text{sp}^3$  C–O bond of ligand **76**, affording the phenoxy nickel halide complex **80** and, presumably, undetected methyl iodide (Scheme **4.1b**). Palladium(II) bis(trifluoroacetate) shows similar selectivity, exclusively giving phenoxypalladium complex **81**. Interestingly, the reaction between  $[\text{Pd}(\text{CF}_3\text{CO}_2)_2]$  and the ethoxy analog of **76** gives a mixture of products resulting from both  $\text{sp}^2$  and  $\text{sp}^3$  C–O bond cleavage: this complex has the potential to effect at least stoichiometric deoxygenation of alkyl aryl ethers. Indeed, heating the  $\text{sp}^3$  C–O activation product **81** at 180 °C under H<sub>2</sub>, results in a second C–O bond cleavage and the formation of **82** within 8 hours. The authors suggest that the hydrogenolysis of the Pd–O  $\sigma$ -bond in **81** affords a palladium hydride intermediate and proximal phenol functionality, which undergoes  $\text{sp}^2$  C–OH bond activation. The implication of the results with palladium is that a system with the right balance of electrophilicity and nucleophilicity can promote the cleavage of both types of C–O bonds.



**Scheme 4.1**

A tandem system, consisting of homogeneous lanthanide triflate and a supported metal(0) nanoparticle, is capable of mediating *catalytic*  $\text{sp}^3$  C–O cleavage (Figure 4.3).<sup>112</sup> Lanthanide triflates are efficient Lewis acidic catalysts for C–O bond formation;<sup>113</sup> this involves the microscopic reverse of C–O bond scission. Coupling the endothermic C–O bond scission ( $\Delta H \approx +14$  kcal/mol) with

exothermic C=C bond hydrogenation ( $\Delta H \approx -25$  kcal/mol) makes the overall transformation of aliphatic ethers to alcohols thermodynamically favourable; the hydrodealkoxylation event is catalyzed by the electrophilic lanthanide, while the electron rich palladium nanoparticles hydrogenate the resulting intermediate alkenols to afford saturated alkanols with high overall selectivity. The reactions are executed in ionic liquids which aid in product recovery and catalyst recyclability. The scope of the process, evaluated over the range 110–185 °C and 3–18 atm of H<sub>2</sub> pressure, includes a series of cyclic and linear substrates; conversions proceed cleanly to the anticipated products. For example, a solution of 2-methyl-2,3-dihydrobenzofuran and 10 mol % ytterbium(III) triflate in the presence of alumina-supported palladium nanoparticles under 18 atm of hydrogen provides 2-propylphenol with a turnover frequency of 0.55 h<sup>-1</sup>. Under the conditions evaluated, this system is limited to substrates that contain CH<sub>3</sub> substituents  $\beta$  to the ether oxygen atom; substrates such as di-*n*-octylether and tetrahydropyran are not activated by this catalytic system. This system strongly resists sp<sup>2</sup> C–O bond cleavage.

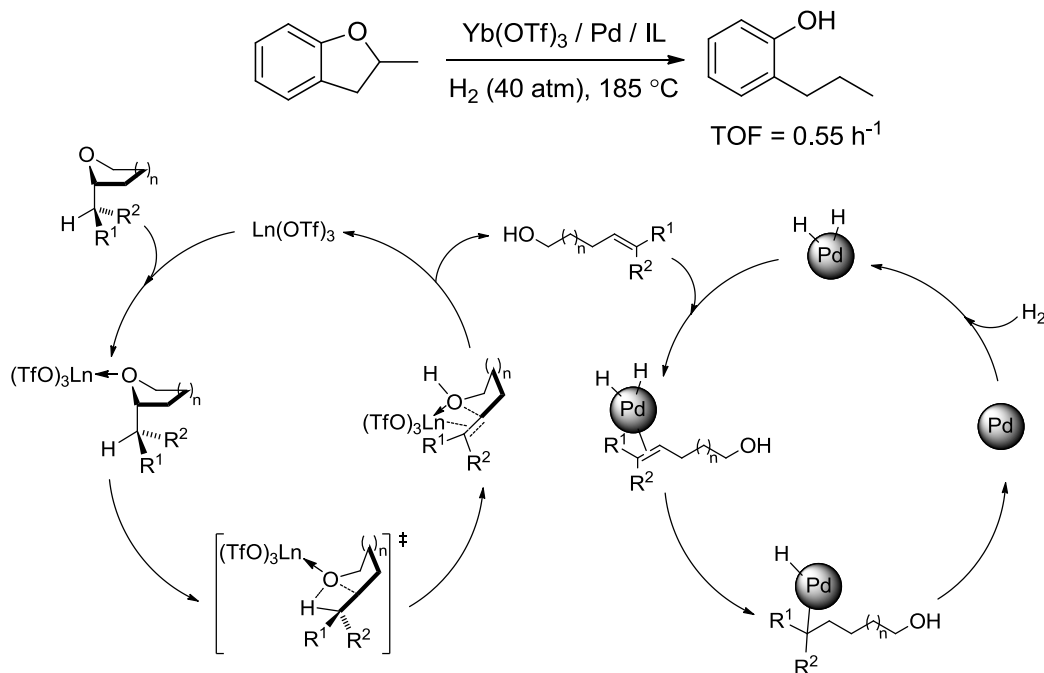
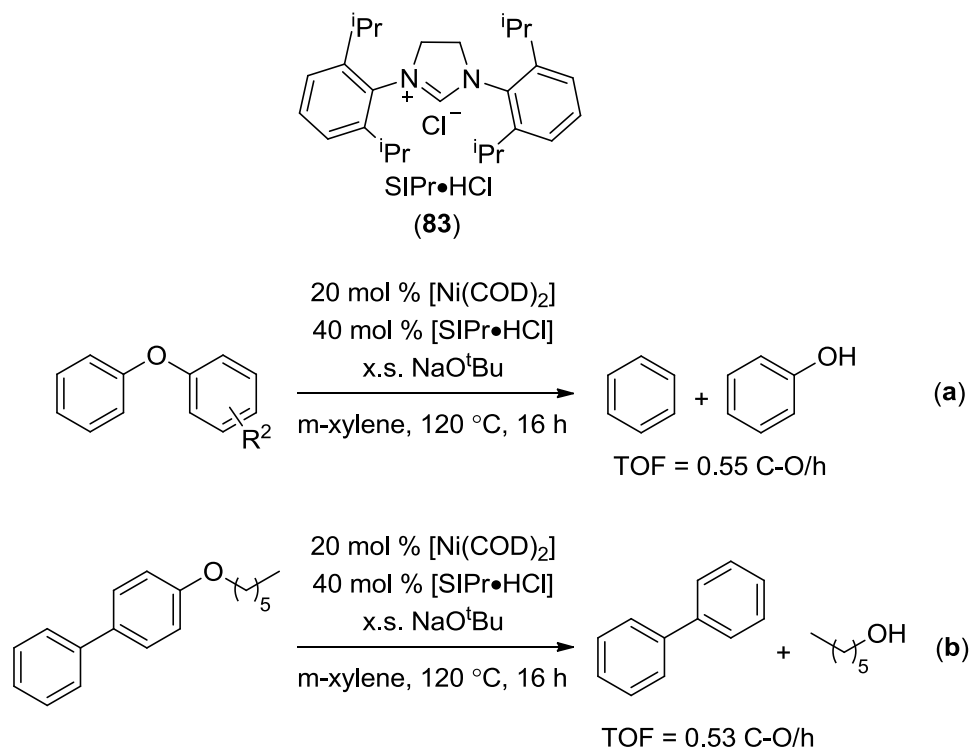


Figure: **4.3**: Ether C–O bond hydrogenolysis by a tandem catalyst system consisting of a lanthanide triflate species and supported palladium nanoparticles.<sup>112</sup>

To date, the most promising system for catalytic C–O bond scission under mild conditions features an electron-rich nickel complex. The catalyst is formed *in situ* by deprotonation of an N-heterocyclic carbene precursor **83** in the presence of [Ni(COD)<sub>2</sub>] (Scheme. **4.2**).<sup>114</sup> While the exact structure of the catalyst is not known, the authors speculate that it is likely an anionic nickelate, a nickel(0) NHC complex, or a nickel hydride complex (Ni-**83** ≡ *in situ* formed catalyst). In the presence of excess base and under one atm of hydrogen, Ni-**83** effects the hydrogenolysis of a range of diaryl ethers, including substrates with electron-withdrawing and electron donating substituents. For example, a 2 : 1 mixture of SIPr•HCl, and [Ni(COD)<sub>2</sub>] in the presence of excess strong base transforms

diphenyl ether in to a 1 : 1 mixture of phenol and benzene at 120 °C under one atm of hydrogen (Scheme **4.2b**). The same reaction, run for 32 hours at 10 mol % nickel loading yields a turnover frequency of 13.0 C–O bond cleavages/day. The *in situ* catalyst also cleaves C–O bonds in alkyl aryl ethers, with a strong preference for sp<sup>2</sup> C–O bonds over sp<sup>3</sup> C–O bonds. 4-Hexyloxybiphenyl, for example, affords an 85% conversion (TOF = 0.53 C–O cleavages/h) to a 1 : 1 mixture of biphenyl and 1-hexanol under similar conditions (Scheme **4.2b**). The absence of hexane in the product mixture implies that no sp<sup>3</sup> C–O bond hydrogenolysis occurs. In both examples, the catalyst does not activate the second C–O of the substrates; the alcohols formed in the reactions are not further deoxygenated to provide base hydrocarbons. Catalysts capable of complete deoxygenation are highly desirable for lignin-to-BTX conversion.



Scheme. 4.2

## 4.2 Results and Discussion

### 4.2.1 C–O bond hydrogenolysis in lignin model compounds

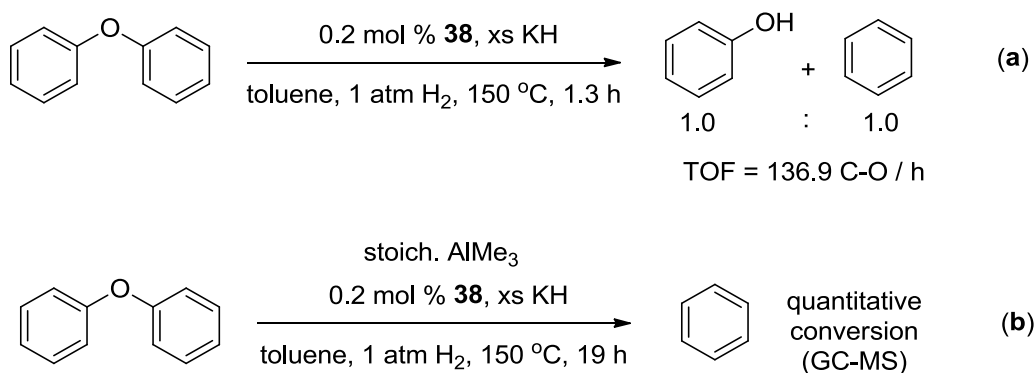
The mixed-valence complex **38** catalyzes C–O bond hydrogenolysis in unstrained ethers. The reactions proceed under extremely mild conditions and at low catalyst loadings. A diverse set of ether functionalities have been used as substrates, including models of the 4-O-5 and  $\beta$ -O-5 linkages in lignin. Complex **38** also “depolymerizes” aromatic polyether model compounds by C–O bond hydrogenolysis, an important demonstration of potential utility in lignin-to-BTX conversion. Importantly, the cleavage of strong aromatic ether linkages does not proceed by prior ring hydrogenation. Aromatic ring hydrogenation wastes

hydrogen and is unproductive in the pursuit of aromatic platform chemicals. The results obtained are preliminary; reaction temperatures and times have been adjusted to allow single-point catalytic rates to be determined, but the effects of differing solvents, scavengers, pressures, *etc.* have not yet been fully established. Follow up investigations from our laboratories will provide insight into this as yet under-developed type of reductive catalysis.

#### *4.2.1.1 Catalytic C–O bond hydrogenolysis of diphenyl ether*

The aromatic C–O–C linkage in diphenyl ether models the 4-O-5 lignin linkage.<sup>102</sup> Precatalyst **38** mediates the hydrogenolysis of this linkage under mild conditions. The reaction affords a 1 : 1 mixture of benzene and phenol (Scheme **4.3a**) under one atmosphere hydrogen and 150 °C. At 1.3 hours, the turnover frequency is 136.9 C–O cleavages per hour. The 1 : 1 product ratio implies that the second C–O bond cleavage – to give a second equivalent of benzene – does not occur. Indeed, even under harsher reaction conditions (170 °C) and longer reaction times (14 h), the reaction affords the same mixture of phenol and benzene. While phenolic C–O bonds are stronger than aromatic ether C–O bonds by ~ 11 kcal/mol (the C–O BDE in phenol is 110 kcal/mol),<sup>96</sup> this difference does not directly account for the absence of the second C–O bond cleavage event. The addition of phenol to a catalytic intermediate would occur by a presumably low-energy O–H activation, not by direct C–O bond activation, which is likely to be a higher energy process. Instead, we attribute the observed reactivity to the strongly

basic reaction conditions. In the presence of the scavenger, any phenol formed is quickly deprotonated to the phenolate anion. Solubility equilibria are likely competing here as the potassium phenolate is only partially soluble in toluene. Deprotonation also increases the C–O bond strength. The anionic phenolate is more nucleophilic than the ether or the phenol, and is more likely to strongly coordinate to the catalyst  $\eta^1$ -via the oxygen atom. If  $\eta^6$ -coordination is necessary for facile catalytic activity in this system, the increased nucleophilicity of the phenolate may be prohibiting the second C–O activation. It is essential to determine conditions for scavenger-free catalytic C–O bond hydrogenolysis to drive HDO to completion.



Scheme. 4.3

The Ni-NHC system Ni-**83** discussed above is the only published example to provide a point of comparison for this reactivity.<sup>114</sup> Much like **38**, Ni-**83** cleaves the C–O bond of diphenyl ether to afford a 1:1 mixture of benzene and phenol, but does not catalyze the second C–O bond hydrogenolysis. The Ni-NHC system also uses a strongly basic reaction medium, so the origins of the effects may be

similar. Both **38** and Ni-**83** function under exceptionally mild conditions. While the two systems are similar, mixed-valence precatalyst **38** has a number of advantages over Ni-**83**: precatalyst **38** is rigorously characterized, thermally robust, and does not require high catalyst loadings (~0.2 vs. 20 mol %).

The Ni-NHC system affords higher catalytic rates in the presence of a stoichiometric quantity of the Lewis acid AlMe<sub>3</sub>.<sup>114</sup> A similar effect has been noted for precatalyst **38**. Not only does stoichiometric AlMe<sub>3</sub> increase the rate of hydrogenolysis, it facilitates the second C–O bond hydrogenolysis, converting diphenyl ether exclusively to benzene (Scheme **4.3b**). Sub-stoichiometric trialkylaluminum and other Lewis acid promoters remain under active investigation. This is an important focal point for follow up experimentation, as the exact role of AlMe<sub>3</sub> in the process is not understood. Presumably, the Lewis acidic centre reduces the C–O bond strength of the ether or phenolate ion by coordinating to the electron rich oxygen atom. This same effect may promote productive binding modes ( $\eta^6$ ) by reducing the nucleophilicity of the phenolate ligand thereby destabilizing the  $\eta^1$ -O bonding mode.

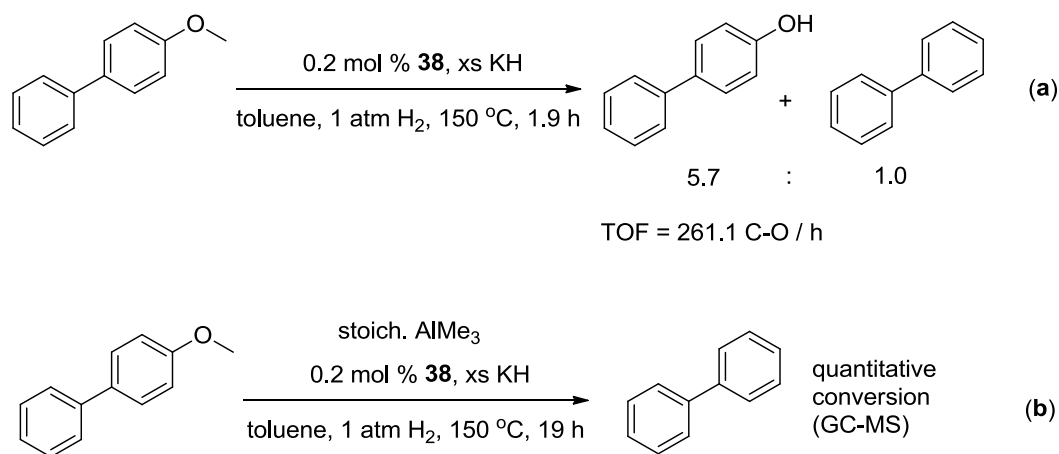
The Lewis acid could also play a role in reducing the activation energy required in the turnover-limiting step of the cycle. In analogy to the catalytic cycle for desulfurization, the turnover-limiting step for complete HDO likely involves the conversion of a  $\mu$ -oxide intermediate back into a reactive hydride-ligated cluster. If this process involves reductive elimination, the Lewis acid may be facilitating

the process by coordinating the metal-bound heteroatom and making it a better leaving group (stabilizing the conjugate base). Reductive eliminations have been shown more facile in the presence of Lewis acids in a number of systems.<sup>115,116</sup> The regeneration step may also involve a  $\sigma$ -BM/ $\sigma$ -CAM process instead of a reductive elimination. In this case the Lewis acid may be acting as a scavenging agent. Trimethyl aluminum could react with the metal bound hydroxide unit to give methane and PhOAlMe<sub>2</sub>. This reaction would likely be irreversible. If this is the case the basic scavenger is not required for catalysis to proceed.

#### *4.2.1.2 Catalytic C–O bond hydrogenolysis of 4-methoxybiphenyl*

4-Methoxybiphenyl is used as a lignin model substrate because it has both sp<sup>2</sup>- and sp<sup>3</sup>-hybridized C–O bonds. The  $\beta$ -O-4 and dibenzodioxacin lignin linkages both feature similar structural motifs.<sup>102</sup> Complex **38** catalyzes the hydrogenolysis of both the aromatic and aliphatic C–O bonds in 4-methoxybiphenyl under mild conditions. As sampled at termination, the reaction proceeds at a rate of 261 C–O cleavages per hour, affording a 1 : 6 mixture of biphenyl and 4-hydroxy biphenyl (Scheme. **4.4a**). The product ratio indicates moderate regioselectivity for sp<sup>3</sup> C–O bond cleavage over sp<sup>2</sup> C–O bond cleavage, although both occur. The selectivity is in accord with standard bond enthalpies; alkyl C–O bond are weaker than aryl C–O bonds by ~ 20 kcal/mol.<sup>96</sup> Similar selectivity for sp<sup>3</sup> C–O bond activation is observed in the stoichiometric transformations of iridium pincer compound **69**. Under harsher reaction conditions and longer reaction times the product ratio

obtained does not change. As in the reaction with diphenyl ether, the first C–O bond hydrogenolysis event forms an aromatic alcohol that is quickly deprotonated and not further defunctionalized. The same factors are likely at play here: stronger C–O bonds, increased nucleophilicity resulting in predominantly  $\eta^1$ -coordination and energetic barriers to reductive elimination. In accord with this hypothesis, the second C–O cleavage in this system is again facilitated by the presence of a Lewis acid. Complex **38** converts 4-methoxy biphenyl exclusively to biphenyl in the presence of stoichiometric  $\text{AlMe}_3$  (Scheme **4.4b**). The exclusive formation of biphenyl could also result from the Lewis acid altering the regioselectivity of the reaction. Catalytic trials with authentic 4-hydroxy biphenyl will provide more insight.

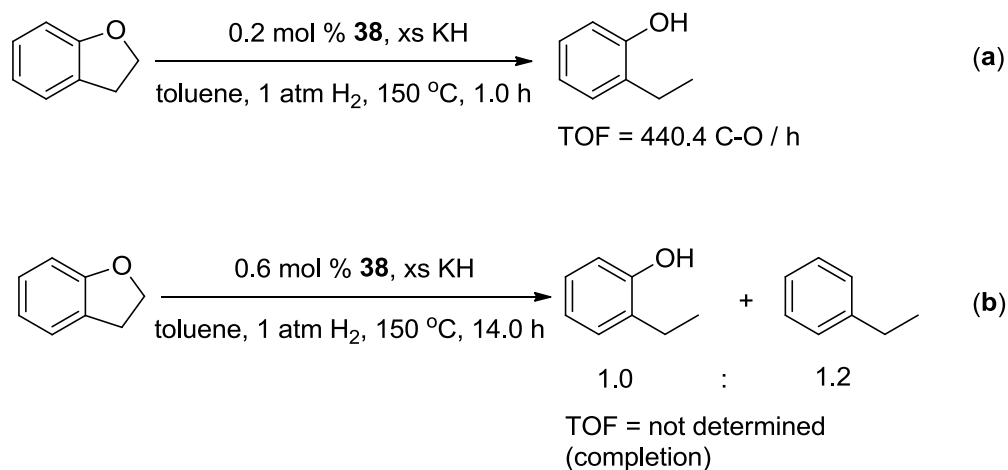


Scheme. 4.4

#### 4.2.1.3 Catalytic C–O bond hydrogenolysis of 2,3-dihydrobenzofuran

Furan moieties are an integral part of the  $\beta$ - $\beta$  lignin linkage. Dihydrobenzofuran is a useful lignin model compound because it has both  $sp^2$  and  $sp^3$  C–O bonds.

Because both linkages are part of a ring, the entropic driving force for C–O bond cleavage is limited. Compound **38** catalyzes the cleavage of the  $sp^3$  C–O bond of 2,3-dihydrobenzofuran under mild conditions. The reaction affords 1-ethylphenol as the exclusive product after one hour (TOF = 440 C–O cleavages per hour, Scheme **4.5a**). In contrast to the trends with the previous two substrates, longer reaction times result in complete hydrodeoxygenation of 2,3-dihydrobenzofuran. Over 14 hours, complex **38** converts 2,3-dihydrobenzofuran into a 1.2 : 1.0 ratio of ethylbenzene to 1-ethylphenol (Scheme **4.5b**). The average turnover frequency was not calculated for this reaction because it proceeded to completion. Why the second C–O bond cleavage occurs with this substrate but not with diphenyl ether or 4-methoxybiphenyl is not well understood. Evaluating the reactivity of **38** towards other cyclic ethers will provide more insight. The catalytic hydrodeoxygenation of an unstrained heterocyclic ether to hydrocarbon is an important demonstration, especially under such mild conditions.

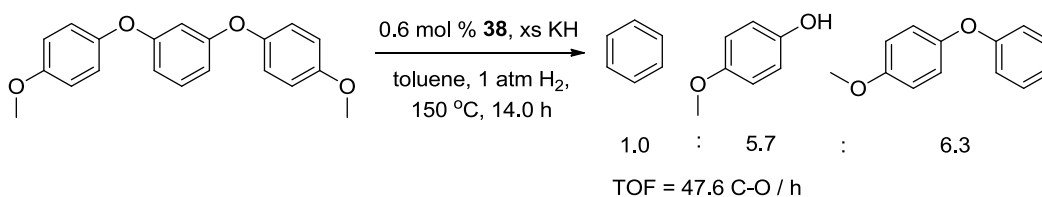


Scheme 4.5

#### 4.2.1.4 1,3-Bis(4-methoxyphenoxy)benzene

1,3-Bis(4-methoxyphenoxy)benzene (**84**) is one of the most complex lignin model compounds commercially available.<sup>102</sup> The three phenyl rings in **84** are mutually tethered by 4-O-5-like sp<sup>2</sup> C–O linkages, and there are two sp<sup>3</sup> C–O bonds in the form of *para*-methoxy aromatic substituents. The relatively large number of C–O linkages in **84** makes it useful for evaluating catalytic depolymerization by C–O bond reduction. Complex **38** catalyzes the “depolymerisation” of **84**; the reaction affords a mixture of fully and partially deoxygenated products (Eqn. 4.5). At 14.0 hours, the turnover frequency is 47.6 C–O bond cleavages/h. The product mixture is comprised of a small amount of benzene, along with 4-methoxyphenol and 1-methoxy-4-phenoxybenzene. It is most likely that the latter two products form from a single interior C–O bond cleavage in **84**. The presence of benzene in the reaction mixture implies two aryl C–O bond hydrogenolysis events occur on the

same phenyl ring, and demonstrates the potential for this system to depolymerize polymeric aryl ethers to base aromatic molecules. The presence of methanol and methane in the reaction mixture was not determined, so there is insufficient data to interpret the selectivity for  $sp^3$  vs.  $sp^2$  C–O bond hydrogenolysis in this system. Nonetheless, the preliminary results are promising, complex **38** is a homogeneous “model catalyst” for lignin-to-BTX conversion under mild conditions.



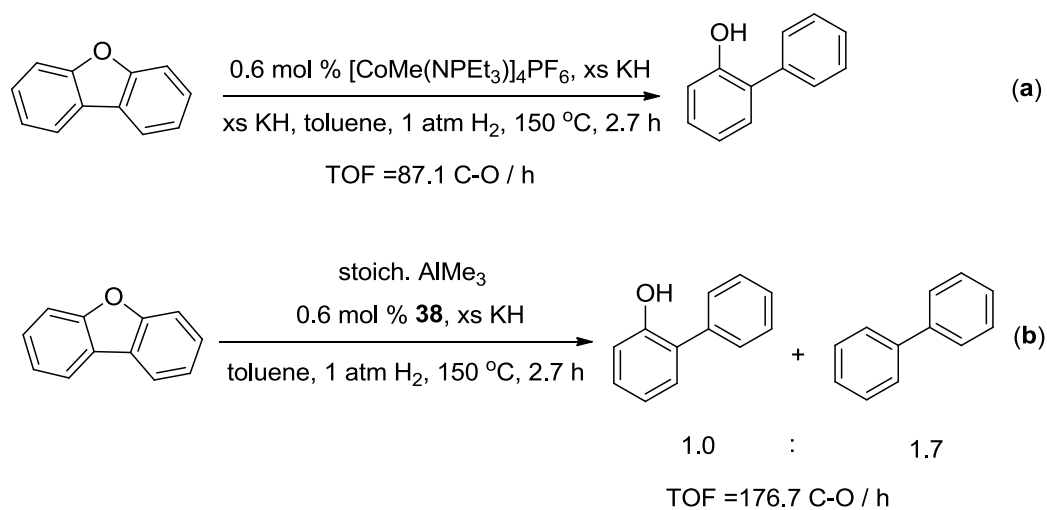
Eqn. 4.5

#### 4.2.2 C–O bond hydrogenolysis related to crude oil hydroprocessing

The results related to catalytic lignin-to-BTX conversion prompted us to push this system towards more refractory substrates related to deoxygenative hydroprocessing. The removal of oxygen and nitrogen from heteroaromatic compounds is of great interest in crude oil hydrotreatment.<sup>106</sup> HDO and HDN are thus of prime importance for the production of high quality fuels.<sup>117</sup> As detailed herein, complex **38** is a catalyst for C–O/C–N hydrogenolysis of refractory heterocycles under mild conditions. Importantly, none of the reactions produce compounds arising from aromatic ring hydrogenation, which wastes hydrogen and reduces fuel quality by lowering the octane rating.<sup>57</sup>

#### 4.2.2.1 Catalytic C–O bond hydrogenolysis of dibenzofuran

Dibenzofurans are the most refractory class of oxygen-containing compounds present in crude petroleum feedstocks.<sup>106</sup> The C–O bonds in dibenzofuran are stronger than the C–S bonds in dibenzothiophene (BDE  $\approx$  115 kcal/mol and 92 kcal/mol respectively).<sup>106,77</sup> Complex **38** nonetheless catalyzes the cleavage of one dibenzofuran C–O bond under mild conditions (Scheme **4.6a**). The reaction affords 2-hydroxybiphenyl as the exclusive product after 2.7 hours (TOF = 87.1 C–O cleavages/hour). Applying harsher reaction conditions and longer reaction times does not promote the second C–O bond hydrogenolysis to give biphenyl, but the addition of a Lewis acid promoter does. In the presence of stoichiometric AlMe<sub>3</sub> complex **38** converts dibenzofuran to a 1.0 : 1.7 mixture of 2-hydroxybiphenyl and biphenyl at an improved rate (TOF = 176.7 C–O cleavages/hour, Scheme **4.6b**).



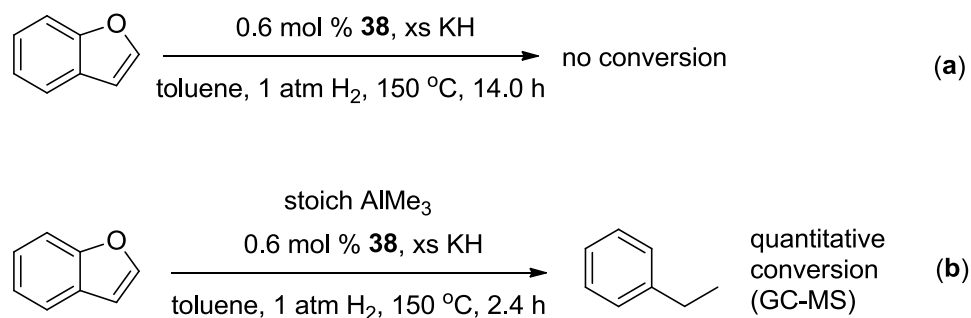
Scheme. 4.6

#### 4.2.2.2 Catalytic C–O bond hydrogenolysis of benzofuran

Benzofurans are the second most refractory class of oxygen-containing compounds present in crude oils. Under the relatively mild conditions accessible in our laboratory, complex **38** does not activate the C–O bond of benzofuran: stirring a slurry of benzofuran, precatalyst **38**, and KH in toluene under 1 atm of hydrogen at 180 °C affords no reaction products over 14 hours (Scheme **4.7a**). The lack of reactivity towards benzofuran might be anticipated, given the slower rate of desulfurization of benzothiophene relative to dibenzothiophene and the modestly increased strength of C–O bonds relative to C–S bonds. We tentatively ascribe the lack of reactivity to a combination of very strong C–O bonds and the muted potential for  $\eta^6$ -coordination – benzofuran has only one benzene aromatic relative to two in dibenzofuran.

The presence of Lewis acid again promotes the C–O bond hydrogenolysis of benzofuran. In fact, benzofuran is *deoxygenated* by precatalyst **38** in the presence of a stoichiometric amount of AlMe<sub>3</sub>. The reaction affords exclusively ethylbenzene after 2.4 hours (Scheme **4.7b**). Comparing this reactivity with that of 2,3-dihydrobenzofuran provides some mechanistic insight. The first C–O bond cleavage event of benzofuran could occur before or after hydrogenation of the isolated double bond. The lack of reactivity noted in the absence of a Lewis acid implies that either the catalyst cannot hydrogenate the double bond, or that the

double bond is hydrogenated after cleavage. The latter seems more likely here given that the reaction does occur in the presence of a Lewis acid.



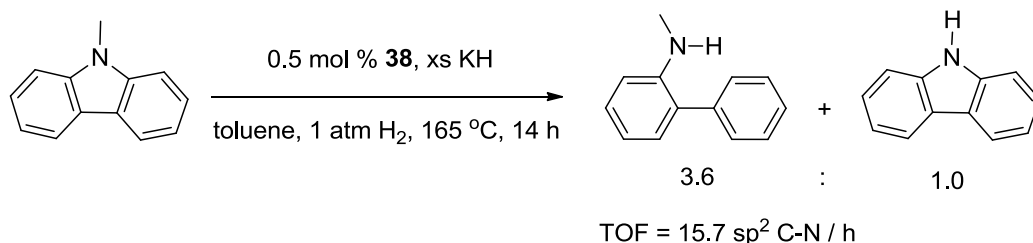
Scheme. 4.7

#### 4.2.2.3 C–N bond activation of N-methylcarbazole.

Current catalyst technologies struggle to denitrogenate refractory nitrogen heterocycles like N-methylcarbazole.<sup>57</sup> Catalytic hydrodenitrogenation of carbazole derivatives is widely believed to be possible only after aromatic ring hydrogenation.<sup>57</sup> The addition of hydrogen to the ring reduces the enthalpic barrier to C–N bond hydrogenolysis –  $\text{sp}^3$  C–N bonds are weaker than  $\text{sp}^2$  C–N bonds.

Complex **38** nonetheless catalyzes both  $\text{sp}^2$  and  $\text{sp}^3$  C–N bond hydrogenolysis of N-methylcarbazole under mild conditions *without prior ring hydrogenation*. The reaction affords a 1.0 : 3.6 mixture of N-dealkylated carbazole and N-methyl-2-biphenylamine after 14 hours at high temperature (TOF = 15.7 C–N cleavages/hour at 165 °C, Eqn. 4.6). The product ratio implies a surprising

preference for the activation of the  $sp^2$  C–N bond, given the previously noted preference for  $sp^3$  C–O bond cleavage over  $sp^2$  C–O bond cleavage. The observed regioselectivity may result from  $\eta^6$ -coordination to the cluster, providing electronic (reduction in C–N bond strength) and entropic (proximity to an adjacent metal centre) activation. To the best of our knowledge, there are no previous accounts of homogeneous catalytic C–N bond hydrogenolysis of refractory nitrogenous heterocycles in the literature.<sup>x</sup> The continuation of this work is a high priority in the group as nitrogen heterocycles are the ultimate challenge and the most environmentally damaging components in heavy oils.



Eqn. 4.6

### 4.3 Conclusions

The mixed-valence cobalt cluster **38** is a precatalyst for C–O and C–N bond hydrogenolysis under low hydrogen pressure and at reasonable temperatures. Precatalyst **38** facilitates the cleavage of both alkyl and aryl carbon-oxygen bonds in a series of compounds that model key linkages in lignin. Complex **38** also

<sup>x</sup> Relative to HDS, HDN chemistry has received very little attention. For leading references on homogeneous HDN see reference 57.

facilitates the cleavage of some of the strong C–O and C–N bonds in heteroaromatic compounds commonly found in crude petroleum. The catalytic transformations proceed under relatively mild conditions and without competitive aromatic hydrogenation, and without char (coke) formation. In some cases, there are no literature systems to provide comparisons to the reported catalytic transformations. Importantly, complete hydrodeoxygenation has been demonstrated with a number of substrates, although a powerful promotor, AlMe<sub>3</sub>, is often required to afford complete HDO. Efficient lignin-to-BTX conversion technologies need to effect complete hydrodeoxygenation, without the use of internal scavenger bases. The results obtained are only ‘semi-optimized’: reaction temperatures and times have been manipulated to allow the determination and comparison of catalytic rates over a range of relevant substrates, rather than optimal turnover for any specific case. While the results reported here are promising, they are only preliminary demonstrations. There is much work to be done to flesh-out the critical components of this system.

In order to establish the applicability of this system to lignin conversion, more complex lignin model compounds need to be evaluated. There are a number of structurally complex lignin-model compounds and pre-treated lignateous feedstocks that are now commercially available.<sup>102</sup> These substrates could act as a step along the path to authentic lignin samples. Catalytic trials involving authentic lignin samples involve an extra level of complexity due to solubility constraints. Commercially-available lignin formulations are not soluble in traditional organic

solvents. Interestingly, however, some types of lignin are soluble in ionic liquids.<sup>118</sup> Finding an ionic liquid that is a suitable solvent for catalysis using complex **38** could allow convenient catalyst recycling and product isolation, and could become an important component of ‘scavenger free’ reactor design.

A number of C–O hydrogenolysis experiments highlight the potential for Lewis acid-assisted reactivity using catalysts derived from **38**. A greater understanding of the role(s) of the promoters would be useful for guiding catalysis design.

Recently, a number of late metal catalyst systems bearing pendant Lewis acid functionality have appeared in the literature.<sup>119</sup> Future work directed towards modifying cluster catalysts such as **38** with pendant Lewis acid functionalities may afford high reactivity catalysts capable of the hydrogenolysis of strong C–O bonds in the absence of additives.

## *5: Conclusions and future work*

The synthetic contributions of this work builds on pioneering work from the groups of Dehnicke and Stephan. Dehnicke and coworkers established that phosphoranimido ligands can nucleate polymetallic clusters of the first-row metals. One of their late-metal clusters,  $[\text{CoCl}(\text{NPEt}_3)]_4$ , is a useful starting material for the preparation of cluster-based reductive catalysts. However, the high temperature fluoro-desilylation preparation of this cluster lacks scalability. A new route to this cluster has been developed by utilizing the phosphoranimide salt metathesis methods developed by Stephan and coworkers. The new method affords analytically pure  $[\text{CoCl}(\text{NPEt}_3)]_4$  in high yield, without the need for organo-azide reagents or energy intensive ‘melt conditions’.

Previous attempts to prepare alkyl substituted late-metal phosphoranimide clusters were unsuccessful. Using a halide-free transmetallation reagent and a solvent system that forces the reaction equilibrium towards products, we have demonstrated that this class of clusters is accessible. Analytically pure  $[\text{CoMe}(\text{NPEt}_3)]_4$  can be prepared from  $[\text{CoCl}(\text{NPEt}_3)]_4$  in high yield, and on gram scale, by transmetallation with dimethylmagnesium in dioxane solution. The methylated cluster has been rigorously characterized, and this and other alkylated clusters are the subjects of ongoing computational and electrochemical studies.

While  $[\text{CoMe}(\text{NPEt}_3)_4]$  is a formidable reductive catalyst on its own, it has been established that single-electron oxidation dramatically increases the reactivity of the cluster. The cationic cluster,  $[\text{CoMe}(\text{NPEt}_3)_4\text{PF}_6]$ , can be prepared from  $[\text{CoMe}(\text{NPEt}_3)_4]$  by outer-sphere electron transfer with  $\text{Cp}_2\text{FePF}_6$ . Structural comparisons indicate that single-electron oxidation results in a contraction and other distortion of the heterocubane framework.

The cationic cluster,  $[\text{CoMe}(\text{NPEt}_3)_4\text{PF}_6]$ , has been evaluated as a precatalyst for homogeneous hydrodesulfurization. Our experimental results suggest that  $[\text{CoMe}(\text{NPEt}_3)_4\text{PF}_6]$  catalyzes the desulfurization of a wide range of organosulfur compounds under mild conditions; highly refractory thiophenic derivatives (dibenzothiophenes, benzothiophenes, and thiophenes) and more reactive thioethers (diaryl sulfides, alkyl aryl ethers, dialkyl sulfides) are all desulfurized under one atmosphere of hydrogen at temperatures between 100 at 180 °C, in the presence of strongly basic agents that act presumably, as proton scavengers to remove the acidic byproducts of the hydrogenolyses. Under similar conditions,  $[\text{CoMe}(\text{NPEt}_3)_4\text{PF}_6]$  catalyzes C–O bond hydrogenolysis. Diaryl ethers, alkyl aryl ethers, and furan derivatives all undergo C–O bond hydrogenolysis. These compounds model important linkages in lignin – an underutilized component of lignocellulosic biomass that is a potential source of aromatic platform chemicals.

There are many exciting extensions of this work– both synthetic and catalytic – that will be pursued in the near future. On the topic of cluster synthesis, the

clusters  $[\text{CoMe}(\text{NPEt}_3)_4]$  and  $[\text{CoMe}(\text{NPEt}_3)_4]\text{PF}_6$  are two examples from a library of potentially useful catalysts that are encapsulated by the general formula:



where  $\text{R}'$  is  $\sigma$ -bonded alkyl ligand;  $\text{M}$  is a late first-row metal;  $\text{R}_3\text{PN}$  is an anionic phosphoranimide ligand;  $n$  equals 2 to 4;  $m$  equals 0, 1, 2, 3, 4 (up to a maximum of  $n$ ); and  $\text{Y}$  is a weakly-coordinating counter-ion, of formal negative charge ' $d$ ', and with stoichiometry ' $e$ ' such that  $d \cdot e = m$ . Future work towards the synthesis of other members of this series will provide insight into the relationships between catalytic activity and a number of variables: metal type, phosphoranimide substituents, capping-alkyl ligand, base-cluster charge, and counter ion. The type-III mixed-valence of  $[\text{CoMe}(\text{NPEt}_3)_4]\text{PF}_6$  is of particular interest here as a series of complexes with different base charges (values of  $m$ ) are potentially available, each one with metal centres of fractionally unique oxidation states.

The preliminary catalytic developments detailed here seed diverse avenues for future work. First and foremost, 'scavenger free' reaction conditions must be identified and optimized. It is likely that 'scavenger free' reaction conditions will require harsher reaction conditions and more sophisticated reactor design(s).

Towards this end,  $[\text{CoMe}(\text{NPEt}_3)_4]\text{PF}_6$  should be evaluated as a catalyst for C-S and C-O bond hydrogenolysis at higher temperature, preferably in an ionic liquid medium. Sparging hydrogen through the solution may facilitate  $\text{H}_2\text{S}$  dissolution and volatilization into the gas phase; passing the gaseous product mixture through

a scaled-down amine scrubber could allow the gas flow to be cycled. Due to the negligible volatility of the ionic liquid medium, product separation and catalyst recycling could be effected under reduced pressure.

Mechanistic studies related to reductive catalysis with  $[\text{CoMe}(\text{NPEt}_3)_4\text{PF}_6]$  are of fundamental interest and will prompt improved catalyst design. Isolation of reaction intermediates, kinetic investigations and stoichiometric transformations should be studied concurrently. These studies can be guided by computations using recently developed and validated computational methodologies.

The isolation/preparation of sulfided form(s) of  $[\text{CoMe}(\text{NPEt}_3)_4\text{PF}_6]$  and related catalysts are important areas for future work. Sulfided forms of the catalyst are more likely to be air stable. Treating  $[\text{CoMe}(\text{NPEt}_3)_4\text{PF}_6]$  with a sulfur transfer reagent ( $\text{S}_8$ ,  $\text{SPPH}_3$ , Lawesson's reagent) or reacting  $[\text{CoMe}(\text{NPEt}_3)_4\text{PF}_6]$  with  $\text{H}_2\text{S}$ —essentially stepping backwards along the catalytic cycle drawn in Figure 3.6—are good places to start this project.

The preparation and characterization of supported heterogeneous catalysts based on the  $[\text{CoMe}(\text{NPEt}_3)_4\text{PF}_6]$  framework is another important area of future work. In addition to the traditional methods for supporting molecular catalysts,<sup>120</sup> there are a number of potentially viable options that exploit the cationic nature of the heterocubane core. Polyanionic solids are ideal in this respect; charge attractions between localized negatively charged sites and cationic clusters provide a means

to ‘support’ discrete clusters without physically tethering them. Anionic supports can be broadly varied in molecular weight, morphology, charge-density, and solubility, as required for catalyst dispersion, activity and recovery.<sup>121</sup>

The suggested areas for future work span synthetic coordination/organometallic chemistry, computational and mechanistic studies, reactor engineering, and surface/heterogeneous sciences. It will be exciting to see where these roads lead.

## 6: *Experimental*

### 6.1 *General procedures* (adapted from previous Stryker group theses)<sup>23,7.</sup>

All manipulations were performed using standard Schlenk techniques on a vacuum/N<sub>2</sub> (or Ar) double manifold or using a Labmaster sp MBraun glovebox under a N<sub>2</sub> atmosphere. Glovebox experiments were performed when the O<sub>2</sub> level was <5 ppm as measured by a Pb-based fuel cell Teledyne O<sub>2</sub> sensor. Solvents were distilled from Na (toluene), Na/benzophenone (THF, benzene), K/benzophenone (hexane, pentane, ether, dioxane) under nitrogen when dark blue or purple, or from CaH<sub>2</sub> (MeCN, CH<sub>2</sub>Cl<sub>2</sub>) under air. Glovebox solvents were tested with a Na/benzophenone solution in THF to ensure they were dry and degassed. Liquid reagents were either distilled under N<sub>2</sub> (or Ar) and stored in a glass “bomb” (a medium walled glass tube with a 14/20 sidearm that seals with a Teflon high vacuum valve) or passed through Activity I neutral alumina into a bomb and subsequently freeze-thaw-degassed three times. Hygroscopic solids were dried overnight in a vacuum oven to remove water before bringing them into the glovebox while hot. Non-hygroscopic solids were brought into the glovebox in vials covered with a kimwipe. Volatile solids were pumped into the Glovebox inside of argon-filled Schlenk flasks. All glassware was flame-dried or dried for at least 30 min in a 150 °C oven before use. Low temperature crystallizations were done at -35 °C in the glovebox freezer. Sample preparation for air sensitive IR spectroscopy was done in the glovebox. Solution IR cells were sealed with Teflon stoppers and parafilm prior to data collection. For elemental analysis of air

sensitive compounds, the samples were prepared in the glovebox using two pre-weighed tin boats. Approximately one mg of sample was placed in one boat and the other boat inserted into the first, then both boats were folded several times into a small cube. The cube was then sealed in a one-dram vial and immediately submitted for analysis. Duplicate samples were run whenever possible. NMR spectroscopy was done in standard NMR tubes sealed with either plastic caps or NMR-tube sized septa. Magnetic susceptibility measurements were obtained via the Evans method<sup>33</sup> in standard NMR tubes. For controlled heating of reaction mixtures, Ika stir plates with digital temperature control were used along with heavy mineral oil (<110 °C) or silicone oil (>110 °C) baths. For reactions requiring sustained low temperature, an immersion cooler (Neslab Cryotrol cc-100) equipped with a temperature controller was used. A high vacuum line, equipped with a three-stage diffusion pump, was used to dry materials for elemental analysis (<10<sup>-5</sup> Torr).

### *6.2 Method for determining magnetic susceptibility (adapted from previous Stryker group theses)<sup>23</sup>*

The Evans method<sup>33</sup> was used to determine magnetic susceptibilities, deriving the room temperature magnetic moment and an estimate of the number of unpaired electrons for [CoMe(NPEt<sub>3</sub>)<sub>4</sub>] and [CoMe(NPEt<sub>3</sub>)<sub>4</sub>]PF<sub>6</sub>. A reference solution of 95/5 v/v C<sub>6</sub>D<sub>6</sub>/cyclohexane was prepared. The solid sample (~5 mg) was dissolved in 2 mL of the reference solution. For each determination, measurements of three separate sample solutions were made. The sample solution

was placed in a melting point capillary tube using a syringe with a 10 cm long 22-gauge needle. This capillary was then placed into a standard NMR tube containing the reference solution and the tube was capped. The  $^1\text{H}$  NMR spectrum was then obtained at room temperature for each sample.

### 6.3 Instrumentation (adapted from previous Stryker group theses)<sup>23,7</sup>

X-ray crystallography was performed using either a Bruker DB diffractometer or a Bruker PLATFORM diffractometer, both equipped with a SMART APEX II CCD area detectors. Diffraction data collection and crystal structures determinations were done by Dr. Robert McDonald and Dr. Michael Ferguson of the University of Alberta Department of Chemistry X-ray Crystallography Laboratory. CHNS elemental analyses were performed on a Carlo Erba EA1108 Elemental Analyzer. Gas chromatography-mass spectrometry was performed using a Hewlett Packard GCD series G1800A GC-MS. The mass detectors used were either HP 5870 or 5971 MSD. The column used was an Agilent DB-5 MS 25m x 0.25 mm x 0.25 micron film thickness. The MS library was the NIST/EPA/NIH 2011 Mass Spectral Library and Software package was NIST11. IR spectroscopic analyses were performed using a Nicolet Magna 750 FT-IR Spectrometer, or a Nicolet 8700 FT-IR Spectrometer operating by OMNIC Spectra Software. All elemental analyses, GC-MS and FT-IR data were obtained by staff at the University of Alberta Department of Chemistry Analytical and Instrumentation Laboratory.  $^1\text{H}$  and  $^{31}\text{P}$  NMR spectra were obtained using either

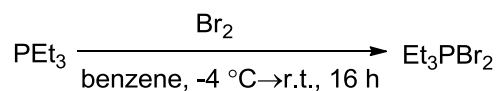
an Agilent/Varian Inova 300 MHz spectrometer or an Agilent/Varian Inova 400 MHz spectrometer at 27 °C. Chemical shifts for  $^1\text{H}$  NMR spectra are reported in ppm and referenced against the residual protium signals of the NMR solvent.  $^{31}\text{P}$  NMR chemical shifts are reported in ppm, referenced to 85% phosphoric acid which is assigned a value of 0 ppm.

#### 6.4 Chemical materials (adapted from previous Stryker group theses)<sup>23,7</sup>.

All commercial reagents were purchased from Strem or Sigma-Aldrich chemical companies were used as received. Where necessary, reagent purifications were accomplished using standard methods. Potassium hydride (KH) required rigorous purification to remove traces of potassium metal and was thus heated overnight at reflux in THF containing 20 mol% naphthalene, then washed three times with anhydrous THF, three times with dried hexanes and dried under vacuum before use. Materials prepared by literature methods or modifications of such methods are noted in the appropriate experimental sections.

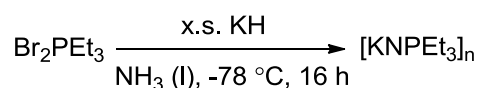
#### 6.5 Synthetic Procedures

##### 6.5.1 Synthesis of dibromotriethyl-phosphorane ( $\text{Et}_3\text{PBr}_2$ )<sup>122</sup>



This procedure was adapted from the literature.<sup>122</sup> An argon-purged 1L Schlenk flask was charged with PEt<sub>3</sub> (30.94 g, 193.6 mmol), 60 mL of benzene and a large bar-shaped stirbar. The flask was fitted with an addition funnel charged with Br<sub>2</sub> (25.42 g, 215.1 mmol) in 40 mL of benzene. The apparatus was placed in an ice-water bath. Drop-wise addition of the bromine solution over the course of two hours yielded an orange slurry which slowly decolourized as the mixture warmed to room temperature and continued stirring overnight. The off-white reaction solids were isolated by filtration and washed with ether (3 x 20 mL). After drying under high vacuum, the product PEt<sub>3</sub>Br<sub>2</sub> (43.05 g, 154.9 mmol, 80 %) was found to be spectroscopically consistent with that reported in the literature and pure by elemental analysis: C: 26.25 (25.93), H: 5.49 (5.44).

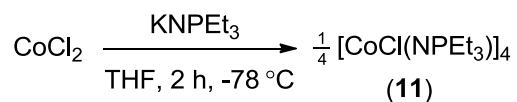
### 6.5.2 Synthesis of potassium triethylphosphoranimide [KNPEt<sub>3</sub>]<sub>n</sub><sup>10</sup>



This procedure was adapted from the literature.<sup>10</sup> Dry ammonia (~ 300 mL) was condensed into an argon-purged, stirbar-equipped, 1 L three-neck flask cooled to -78 °C in a dry ice/isopropanol bath. Potassium hydride (7.61 g, 189.7 mmol) was added to the flask in ~1 g increments over two hours, yielding an off-white slurry. After stirring for three hours, PEt<sub>3</sub>Br<sub>2</sub> (15.52 g, 55.8 mmol) was added in ~2 g increments over two hours. The slurry darkened from off-white to brown. Approximately 200 mL of hexanes was added to the flask, and the reaction

mixture was left to warm to room temperature overnight, venting the ammonia. In the morning, the dark brown solution was filtered and the solvent was removed under reduced pressure leaving a waxy brown solid. The product  $[\text{KNPEt}_3]_n$  (7.61 g, 154.9 mmol, 79 %), was found to be pure by elemental analysis after drying under high vacuum. The elemental analysis data obtained represents an improvement over that originally published: C: 42.02 (42.08), H: 8.82 (8.83), N: 7.82 (8.18).

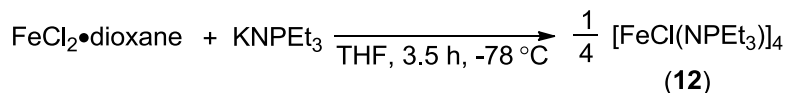
### 6.5.3 Synthesis of $[\text{CoCl}(\text{NPEt}_3)]_4$ (**11**) by salt metathesis



The cobalt cluster **11** has been reported in the literature;<sup>17</sup> this procedure provides an alternate fully reproducible method of synthesis. An argon-purged 1L Schlenk flask was charged with  $\text{CoCl}_2$  (14.83 g, 114.2 mmol), approximately 600 mL of THF and a large bar-shaped stirbar. After 30 minutes of stirring at room temperature, the flask was fitted with an addition funnel charged with a solution of  $\text{KNPEt}_3$  (19.56 g, 114.2 mmol) in approximately 150 mL of THF. The apparatus was placed in an isopropanol/dry ice bath. After cooling, the  $\text{KNPEt}_3$  solution was introduced to the reaction drop-wise, with vigorous stirring, yielding a homogeneous dark green solution. The reaction was left to stir at  $-78^\circ\text{C}$  for one hour before the solvent was removed under reduced pressure, leaving mixture of

green and white solids. Trituration with CH<sub>2</sub>Cl<sub>2</sub> (3 x 50 mL) gave a dark green solution, which was filtered through a glass frit before the CH<sub>2</sub>Cl<sub>2</sub> was evaporated. The dark green solids were washed with hexanes (3 x 40 mL), then recrystallized from cold THF. The product **11** (18.92 g, 20.8 mmol, 73 %) was determined to be pure by elemental analysis: C: 32.00 (31.81) H: 6.59 (6.67) N:6.31 (6.18). Single crystals were grown by slow diffusion of pentane into a solution of **11** in toluene. X-ray diffraction confirmed the material to be identical to that reported in the literature. The isolated yield of **11** from this procedure was 33 % higher than the literature yield.

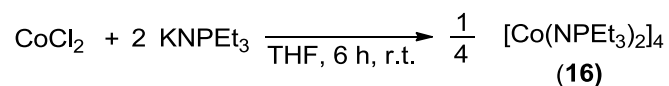
#### 6.5.4 Synthesis of [FeCl(NPEt<sub>3</sub>)]<sub>4</sub> **12** by salt metathesis



The iron cluster **12** has been reported in the literature;<sup>18</sup> this procedure provides an alternate method of synthesis. FeCl<sub>2</sub>•dioxane was prepared by Soxhlet-extraction of FeCl<sub>2</sub> with 1,4-dioxane. An argon-purged 500 mL Schlenk flask was charged with FeCl<sub>2</sub>•dioxane (3.00 g, 14.0 mmol), approximately 300 mL of THF and a large bar-shaped stirbar. After two hours of stirring at room temperature, the flask was fitted with an addition funnel charged with a solution of KNPEt<sub>3</sub> (2.51 g, 14.7 mmol) in approximately 150 mL of THF. The apparatus was placed in an isopropanol/dry ice bath. The KNPEt<sub>3</sub> solution was introduced to the reaction

drop-wise yielding a dark brown solution. The reaction was left to stir at  $-78\text{ }^{\circ}\text{C}$  for one hour, then the solvent was removed under reduced pressure, leaving a mixture of brown and grey solids. Trituration with  $\text{CH}_2\text{Cl}_2$  (3 x 30 mL) gave a brown solution which was filtered through a glass frit before the  $\text{CH}_2\text{Cl}_2$  was removed under reduced pressure. After washing with pentane (3 x 20 mL), the black crystalline solid was recrystallized from cold THF. The product **12** (1.68 g, 1.9 mmol, 54 %) was found to be pure by elemental analysis. C: 32.64 (32.25) H: 6.68 (6.77) N: 5.99 (6.27). Single crystals of **12** were grown from cold THF. X-ray diffraction confirmed the material to be identical to that reported in the literature. The isolated yield of **12** from this procedure was 27 % lower than the literature yield.

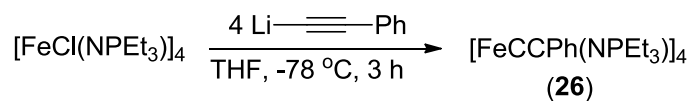
#### 6.5.5 Synthesis of $[\text{Co}(\text{NPEt}_3)_2]_4$ (**16**) by salt metathesis



Inside the drybox,  $\text{CoCl}_2$  (18.95 mg, 0.15 mmol) was suspended in approximately 10 mL of THF in a 5-dram vial. A small stir bar was added to the vial. A solution of  $\text{KNPEt}_3$  (50.0 mg, 0.29 mmol) in approximately 7 mL of THF was introduced drop-wise over 15 minutes forming a dark blue solution. The mixture was stirred at room temperature for six hours. Filtration through a Celite plug separated an

off-white solid that was discarded. The filtrate was pumped dry leaving a dark blue solid. Trituration with pentane (2 x 5 ml) gave a blue solution, which was passed through a Celite plug. The pentane was removed under reduced pressure. The product **16** (32 mg,  $5.0 \times 10^{-2}$  mmol, 68 %) was submitted for elemental analysis after drying under high vacuum: C: 44.41 (44.59) H: 9.43 (9.35) N: 8.07 (8.67). Single crystals of **16** were grown from cold hexane and submitted for X-ray diffraction experiments. This procedure has been scaled to gram scale.<sup>23</sup>

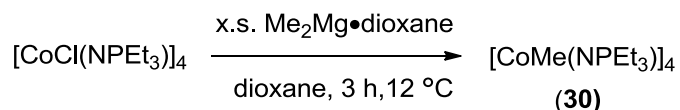
#### 6.5.6 Synthesis of $[Fe(CCPH)(NPEt_3)]_4$ (**26**) by salt metathesis



An argon-purged 300 mL Schlenk flask was charged with  $[FeCl(NPEt_3)]_4$  (1.40 g, 1.57 mmol), approximately 100 mL of THF and a small bar-shaped stirbar. After 30 minutes of stirring at room temperature, the flask was fitted with an addition funnel and charged with 1.0 M lithium phenylacetylide in THF (66.0 mL, 6.60 mmol). The apparatus was placed in an isopropanol/dry ice bath. After cooling, the lithium phenylacetylide solution was introduced drop-wise over 30 minutes, resulting in a darkening of the brown solution. The reaction was left to stir and warm to room temperature for two hours before the solvent was removed under reduced pressure leaving mixture of black and grey solids. Trituration with

benzene (3 x 20 mL) yielded a dark brown solution, which was filtered through a glass frit before the benzene was removed under reduced pressure. The black solids were washed with hexanes (3 x 40 mL) and recrystallized from cold benzene. The product **26** (1.27 g, 1.10 mmol, 70 %) was submitted for elemental analysis: C: 58.46 (58.16) H: 5.76 (6.97) N:2.60 (4.84). Single crystals were grown by vapour-diffusion of pentane into a solution of **26** in benzene and submitted for X-ray crystallography.

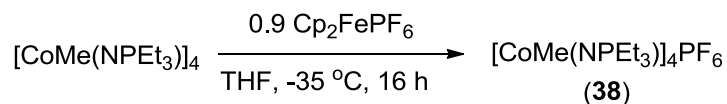
#### 6.5.7 Synthesis of $[\text{CoMe}(\text{NPEt}_3)]_4$ (**30**) by salt metathesis



Inside the drybox,  $[\text{CoCl}(\text{NPEt}_3)]_4$  (453 mg, 0.55 mmol) and  $\text{Me}_2\text{Mg}\cdot\text{dioxane}$  (313 mg, 2.20 mmol)<sup>123</sup> were separately dissolved in eight mL portions of dioxane in 5-dram vials. Stir bars were added to both vials and both were cooled to 12 °C in the drybox freezer. The  $[\text{CoCl}(\text{NPEt}_3)]_4$  solution was stirred rapidly while the  $\text{Me}_2\text{Mg}\cdot\text{dioxane}$  solution was added drop-wise over five minutes, resulting in a darkening of the green solution. The reaction was left to stir for two hours before the dioxane was removed under reduced pressure leaving a mixture of green and white solids. Trituration with hexanes (3 x 20 mL) gave a green solution that was passed through two Celite plugs before the solvent was removed under reduced pressure, leaving a highly crystalline green solid. After drying under high

vacuum, the product **30** (412.6 mg, 0.50 mmol, 91 %) was found to be pure by elemental analysis without further purification: C: 44.68 (40.69) H: 8.64 (8.80) N: 6.70 (6.68). Single crystals of **30** were grown from cold THF and submitted for X-ray crystallography. Solution magnetic susceptibility experiments found **30** to be a 4.90-electron paramagnet ( $\mu_{eff} = 5.82 \mu_{Bo}$ ) at room temperature. IR:  $\nu/\text{cm}^{-1}$  in  $\text{CDCl}_3$  solution = 463 m, 488 m, 571 w, 501 w, 775 m, 1067 s, 1382 m, 2078-2094 w.

#### 6.5.8 Synthesis of $[\text{CoMe}(\text{NPEt}_3)]_4\text{PF}_6$ (**38**) by outer-sphere oxidation



Inside the drybox,  $[\text{CoMe}(\text{NPEt}_3)]_4$  (256 mg, 0.31 mmol) and  $\text{Cp}_2\text{FePF}_6$  (92.3 mg, 0.28 mmol) were dissolved/suspended in 10 mL portions of THF in separate 5-dram vials. Both vials were equipped with small stirbars before being cooled to  $-35 \text{ }^\circ\text{C}$ . The  $[\text{CoMe}(\text{NPEt}_3)]_4$  solution was stirred rapidly while the  $\text{Cp}_2\text{FePF}_6$  slurry was introduced drop-wise. The solution color changed from green to black as the reaction was warmed to room temperature and stirred for 16 hours. The solution was transferred to a 500 mL round bottom flask and diluted with approximately 300 mL of hexanes causing a black solid to precipitate from solution. The solids were isolated by filtration and washed with hexanes (3 x 10 mL), then recrystallized from cold THF. After drying under high vacuum, the

product **38** (201 mg, 0.21 mmol, 67 %) was found to be pure by elemental analysis C: 34.74 (34.69) H: 7.41 (7.49) N: 5.54 (5.78). Single crystals of **38** were grown from cold THF and submitted for X-ray diffraction experiments. IR:  $\nu/\text{cm}^{-1}$  in  $\text{CDCl}_3$  solution= 496 m, 557 m, 776 w, 846 s, 1060 s, 1382 w, 1452 w, 2077-2090 w.

#### *6.4 Catalytic Procedures*

The catalytic experimental procedures detailed below report percent conversions and turnover frequencies (TOF's). Percent conversions were determined by integrating starting material/product peaks in the GC-MS spectra. GC-MS experiments were completed by Staff at the University of Alberta Analytical Services Laboratory using the following method: Injections were performed using Agilent 7673 Automatic Liquid Sampler for 1 microliter aliquots. Run times were 35 minutes including 3.5 minutes of solvent delay (or no delay depending on reaction mixture). The initial temperature was 50 °C (hold time of two minutes) and the final temperature was 280 °C (hold time of five minutes). The temperature was ramped at a rate of 10 °C/min. TOF's were calculated based on starting material/product peak integration from GC-MS; one catalytic turnover was calculated as one mole of C-S bond activated product per mole of cluster per hour. In order to directly compare TOF's, determinations must be obtained under 'saturation-kinetics', where rate is not limited by substrate concentration. The TOF's determined here are 'single-point determinations' and some are clearly limited by substrate concentration. In this preliminary investigation, no effort was

made to determine if or how the turnover frequency changes as a function of conversion, other than to confirm that no induction period is observed. In these instances, the reported TOF's are un-normalized for time course. Isolated yields are also reported for catalytic trials run to completion using substrates that afford non-volatile product(s). Isolated yields were determined by weighing the recovered products, as determined by  $^1\text{H}$  NMR spectroscopy from reactions that proceeded to completion, as determined by GC-MS analysis.

#### *6.4.1 [CoMe(NPEt<sub>3</sub>)<sub>4</sub>] and [CoMe(NPEt<sub>3</sub>)<sub>4</sub>]PF<sub>6</sub> as precatalysts for hydrodesulfurization*

Procedure 6.4.1 was used for catalytic trials at both high and low pressure. High pressure trials employed a Teflon-sealed stainless steel Parr reactor, fitted with a glass insert, a Swagelok® Quick Connect hydrogen inlet, and a pressure gauge ranging from 100 to 2000 psi. Low pressure trials employed a medium-walled glass reactor fitted with a Teflon stopcock. These vessels are informally referred to as “glass bombs”. Table **6.1** lists the independent and dependant variables for each trial.

Procedure 6.4.1: Inside a nitrogen-filled dry box, the steel reactor/glass bomb was charged with dibenzothiophene (134 mg, 0.73 mmol), a weighed quantity of either [CoMe(NPEt<sub>3</sub>)<sub>4</sub>] or [CoMe(NPEt<sub>3</sub>)<sub>4</sub>]PF<sub>6</sub> (0.5 mol %), KH (200 mg, 4.99 mmol), 15 mL toluene, and a magnetic stir bar. The reactor/bomb was sealed before it was removed from the dry box, connected to a hydrogen manifold, and charged with H<sub>2</sub> to the pressure indicated. The reactor/bomb was then placed in a

thermostat-regulated bath at 110 °C and stirred magnetically at a consistent rate of 1200 rpm. After the time period indicated, the reactor was cooled to room temperature and the reaction mixture was quenched with a 10% HCl solution. A portion of the organic layer was dried with powdered anhydrous Na<sub>2</sub>SO<sub>4</sub>, pressed through a short Florisil<sup>TM</sup> column, and then submitted for GC-MS analysis. Dibenzothiophene<sup>124</sup>, 2-thiobiphenyl<sup>125</sup>, and biphenyl<sup>126</sup> were detected in the analysis.

**Table 6.1:** Catalytic hydrodesulfurization of dibenzothiophene by [CoMe(NPEt<sub>3</sub>)<sub>4</sub>] (30) and [CoMe(NPEt<sub>3</sub>)<sub>4</sub>]PF<sub>6</sub> (38).<sup>a</sup>

Entry	[Cat]	H <sub>2</sub> Pressure (atm)	Time (h)	TOF <sup>b</sup> (h <sup>-1</sup> )
1	30	34	17	4.62
2	30	1	17	0.0
3	30	34	2.0	4.12
4	30	34	1.2	0.0
5	38	1	0.5	95.00

- a. Experiments under 1 atm H<sub>2</sub> pressure were conducted in sealable medium-walled glass vessels charged with one atm H<sub>2</sub> at 25°C and excess KH, followed by immersion in a thermostat-regulated oil bath at the given temperature. High pressure experiments were conducted a similar manner using a stainless steel autoclave. In all trials the substrate concentration was 50 mmol/L and the precatalyst concentration was 0.25 mmol/L.
- b. Moles of C–S bonds cleaved per mol of cluster per hour.

## 6.4.2 Control Experiments

### 6.4.2.1 Differentiating heterogeneous and homogeneous processes in the catalytic desulfurization of dibenzothiophene by $[\text{CoMe}(\text{NPEt}_3)]_4\text{PF}_6$

To evaluate the effects of excess  $\text{Hg}(0)$ <sup>80</sup> on the catalytic desulfurization of dibenzothiophene by **38**, two trials were conducted under otherwise identical conditions, following procedure 6.4.2.1: one in the presence of excess  $\text{Hg}(0)$  and one in the absence of  $\text{Hg}(0)$ .<sup>xi</sup> Table **6.2** lists the reagent quantities and the isolated yields for both trials.

Procedure 6.4.2.1: Inside a nitrogen-filled dry box, a medium-walled glass bomb was charged with the quantity of dibenzothiophene indicated, the quantity of  $\text{Hg}(0)$  indicated, precatalyst **38** (0.001 g,  $1 \times 10^{-3}$  mmol), KH (200 mg, 4.99 mmol), 10 mL THF, and a stir bar. The bomb was sealed with a Teflon-coated vacuum stopcock before it was removed from the dry box, connected to a hydrogen manifold, and charged with  $\text{H}_2$  (1 atm). The reactor was then placed in a thermostat regulated bath at 150 °C and stirred at 1200 rpm. After two hours, the reactor was cooled to room temperature and the reaction mixture was quenched with a 10% HCl solution. The organic fraction was isolated and the aqueous fraction was extracted thrice with 10 ml portions of diethyl ether. The organic fractions were pooled, dried with anhydrous  $\text{Na}_2\text{SO}_4$  and filtered through a small column of Florisil<sup>TM</sup>. The solvent was removed under reduced pressure and the

---

<sup>xi</sup> Cobalt is one of a number of transition metals that is passivated in heterogeneous form due to its solubility in mercury as opposed to its tendency to form an amalgam.<sup>79</sup>

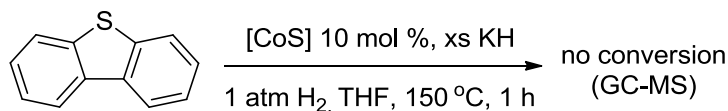
residue was weighed and then dissolved in approximately 10 ml THF for GC-MS analyses.

Table 6.2: Differentiating heterogeneous and homogeneous processes in the catalytic desulfurization of dibenzothiophene by  $[\text{CoMe}(\text{NPEt}_3)_4]\text{PF}_6$  (**38**).<sup>a</sup>

Entry	DBT mg, (mmol)	Hg(0) g (mmol)	Isolated BP <sup>b</sup> g (mmol)	Isolated % yield
1	134.1 (0.72)	2.2 (10.8)	105.8 (0.69)	95.3
2	134.9 (0.73)	0.0 (0.0)	107.9 (0.70)	95.5

- a. Experiment in the absence/presence of Hg(0) was conducted in sealable medium-walled glass vessels charged with a THF solution of DBT and **38**, excess KH was added before the addition of 1 atm H<sub>2</sub> at 25 °C followed by immersion in a thermostat-regulated oil bath at 150 °C for two hours.
- b. Product identified by GC-MS<sup>126</sup>.

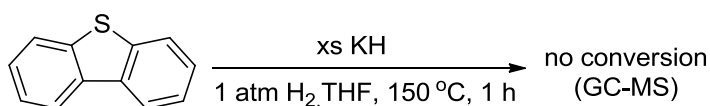
#### 6.4.2.2 Cobalt sulfide as (heterogeneous) catalyst for the desulfurization of dibenzothiophene



Inside a nitrogen-filled dry box, a medium-walled glass bomb was charged with dibenzothiophene (134 mg, 0.73 mmol), bulk CoS (200 mesh) (9 mg,  $7 \times 10^{-2}$  mmol), KH (200 mg, 4.99 mmol), 10 mL THF, and a stir bar. The bomb was sealed before it was removed from the dry box, connected to a hydrogen manifold, and charged with H<sub>2</sub> (1 atm). The reactor was then placed in a thermostat-regulated oil bath at 150 °C and stirred at 1200 rpm. After one hour, the reactor was cooled to room temperature and the reaction mixture quenched

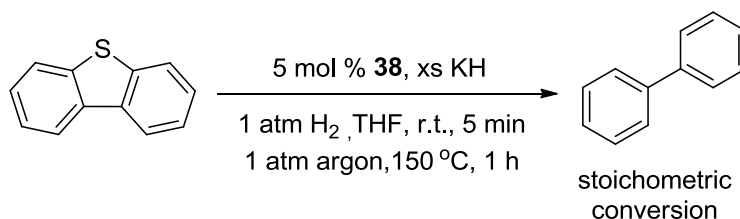
with a 10% HCl solution. A fraction of the organic layer was dried with anhydrous Na<sub>2</sub>SO<sub>4</sub>, pressed through a short Florisil™ column, and then submitted for GC-MS analysis. No conversion of dibenzothiophene<sup>124</sup> to biphenyl<sup>126</sup> or 2-thiobiphenyl<sup>125</sup> was detected.

#### 6.4.2.3 Potassium hydride as catalyst or reagent for the catalytic desulfurization of dibenzothiophene



Inside a nitrogen-filled dry box, a medium-walled glass bomb was charged with dibenzothiophene (134 mg, 0.73 mmol), KH (200 mg, 4.99 mmol), 10 mL THF, and a stir bar. The bomb was sealed with a Teflon-coated stopcock before it was removed from the dry box, connected to a hydrogen manifold, and charged with H<sub>2</sub> (1 atm). The reactor was then placed in a thermostat regulated bath at 150 °C, and stirred at 1200 rpm. After one hour, the reactor was cooled to room temperature and the reaction mixture was quenched with a 10% HCl solution. A fraction of the organic layer was dried with anhydrous Na<sub>2</sub>SO<sub>4</sub>, pressed through a short Florisil™ column, then submitted for GC-MS analysis. No conversion of dibenzothiophene<sup>124</sup> to biphenyl<sup>126</sup> or 2-thiobiphenyl<sup>125</sup> was detected.

#### 6.4.2.4 Potassium hydride as the reductant in the catalytic hydrodesulfurization of dibenzothiophene



Inside a nitrogen-filled dry box, a medium-walled glass bomb was charged with dibenzothiophene (134 mg, 0.73 mmol), precatalyst **38** (35 mg,  $3.7 \times 10^{-2}$  mmol,) KH (200 mg, 4.99 mmol), 10 mL THF, and a stir bar. The bomb was sealed with a Teflon-coated stopcock before it was removed from the dry box, connected to a hydrogen manifold, and charged with H<sub>2</sub> (1 atm). The reaction was stirred at 1200 rpm for 5 minutes, then depleted of hydrogen and charged with argon on an Ar-manifold (1 atm). The reactor was then placed in a thermostat-regulated bath at 150 °C, and stirred at 1200 rpm. After one hour, the reactor was cooled to room temperature and the reaction mixture was quenched with a 10% HCl solution. A fraction of the organic layer was dried with anhydrous Na<sub>2</sub>SO<sub>4</sub>, pressed through a short Florisil<sup>TM</sup> column, then submitted for GC-MS analysis. The process as described afforded 4.2% conversion of dibenzothiophene<sup>124</sup> to biphenyl<sup>126</sup>.

#### 6.4.3 Preliminary evaluation of the relationship between rate and external temperature for dibenzothiophene hydrodesulfurization by [CoMe(NPEt<sub>3</sub>)<sub>4</sub>PF<sub>6</sub>]

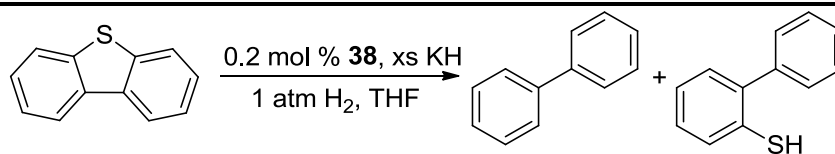
General procedure 6.4.3 was used to investigate the relationship between external temperature and the rate of catalytic hydrodesulfurization of dibenzothiophene

using precatalyst **38**. Table **6.3** lists the dependent and independent variables for each trial.

Procedure 6.4.3: Inside a nitrogen-filled dry box, a medium-walled glass bomb was charged with dibenzothiophene (134 mg, 0.73 mmol), **38** (1 mg,  $1 \times 10^{-3}$  mmol), KH (200 mg, 4.99 mmol), 10 mL THF, and a stir bar. The bomb was sealed with a Teflon high vacuum stopcock before it was removed from the dry box, connected to a hydrogen manifold, and charged with H<sub>2</sub> (1 atm). The reactor was then placed in a thermostat-regulated bath at the temperature indicated and stirred at 1200 rpm. After the reaction time indicated, the reactor was cooled to room temperature and the reaction mixture was quenched with a 10% HCl solution. A fraction of the organic layer was dried with anhydrous Na<sub>2</sub>SO<sub>4</sub>, pressed through a short Florisil™ column, then submitted for GC-MS analysis.

Table **6.3**: Catalytic rate as a function of external reaction for the hydrodesulfurization of dibenzothiophene with [CoMe(NPEt<sub>3</sub>)<sub>4</sub>PF<sub>6</sub>]<sup>a</sup>

Entry	Temp (°C)	Time (min)	TOF <sup>b</sup> (h <sup>-1</sup> )
1	90	120	0
2	110	150	96.3
3	130	60	242.9
4	150	40	448.6
5	165	30	1109.1
6	182	12	3104.4
7	200	7	7685.3



<sup>a</sup>All experiments were conducted in sealable medium-walled glass vessels charged with 1 atm H<sub>2</sub> at 25 °C and excess KH, followed by immersion in a thermostat-regulated oil bath at the given temperature.

<sup>b</sup>C–S bond cleavages per mol of cluster per hour, as determined from distributions of dibenzothiophene<sup>124</sup>, 2-thiobiphenyl<sup>125</sup> and biphenyl<sup>126</sup> by GC-MS.

#### *6.4.4 Alternative scavengers for the catalytic desulfurization of dibenzothiophene by [CoMe(NPEt<sub>3</sub>)<sub>4</sub>PF<sub>6</sub>]*

Procedure 6.4.4 was used for catalytic trials featuring alternative scavengers for the catalytic desulfurization of dibenzothiophene by compound **38**. Table **6.4** lists the independent and dependant variables for each trial.

Procedure 6.4.4: Inside a nitrogen-filled dry box, a medium-walled glass bomb was charged with dibenzothiophene (134 mg, 0.73 mmol), **38** (1 mg, 1.1 x 10<sup>-3</sup> mmol), five molar equivalents of the scavenger indicated, 10 mL THF, and a stir bar. The bomb was sealed with a Teflon-coated stopcock before it was removed from the dry box, connected to a hydrogen manifold, and charged with H<sub>2</sub> (1 atm). The reactor was then placed in a thermostat regulated bath at the temperature indicated, and stirred at 1200 rpm. After the time indicated, the reactor was cooled to room temperature and the reaction mixture was quenched with a 10% HCl solution. A fraction of the organic layer was dried with anhydrous Na<sub>2</sub>SO<sub>4</sub>, pressed through a short Florisil<sup>TM</sup> column, then submitted for GC-MS analysis.

Table 6.4: Alternative scavengers for the catalytic desulfurization of dibenzothiophene by  $[\text{CoMe}(\text{NPEt}_3)]_4\text{PF}_6$

Entry	Scavenger <sup>d</sup>	Time (h)	TOF <sup>b</sup> (h <sup>-1</sup> )
1	NaO <sup>t</sup> Bu	16	s <sup>e</sup>
2	KO <sup>t</sup> Bu	16	s
3	LDA	16	0.71
4	KDA	16	32.73
5	LiTMP	16	0.55
6	KTMP	16	75.5
7	NaH	16	s
8	KH	0.4	310 <sup>c</sup>

<sup>a</sup>All experiments were conducted in sealable medium-walled glass vessels charged with 1 atm H<sub>2</sub> at 25 °C and five equivalents of the appropriate scavenger, followed by immersion in a thermostat-regulated oil bath at the given temperature.

<sup>b</sup>C–S bond cleavages per mol of cluster per hour, as determined from distributions of dibenzothiophene<sup>124</sup>, 2-thiobiphenyl<sup>125</sup>, and biphenyl<sup>126</sup> by GC-MS analysis.

<sup>c</sup>Rxn proceed to completion, calculated TOF is considered a minimum.

<sup>d</sup>LDA = lithium diisopropylamide; KDA = potassium diisopropylamide; LiTMP = lithium 2,2,6,6-tetramethylpiperidide; KTMP = potassium 2,2,6,6-tetramethylpiperidide

<sup>e</sup>s = stoichiometric conversion.

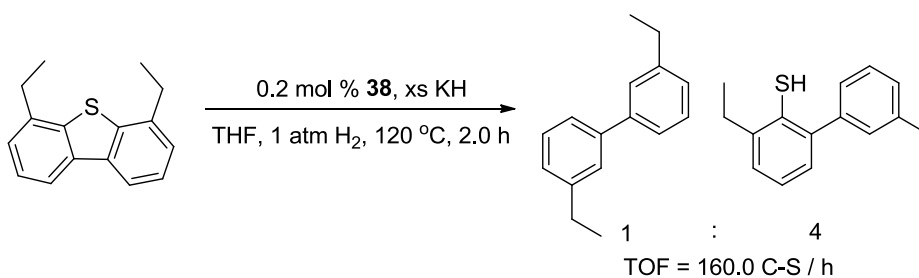
#### 6.4.5 Substrate scope for catalytic desulfurization with $[\text{CoMe}(\text{NPEt}_3)]_4\text{PF}_6$

Procedure 6.4.5 was used to investigate the hydrodesulfurization substrate scope for precatalyst **38**. Specifics for each substrate are listed under their appropriate headings.

Procedure 6.4.5: Inside a nitrogen-filled dry box, a medium-walled glass bomb was charged with **38** (1 mg,  $1.11 \times 10^{-3}$  mmol), KH (117 mg, 2.92 mmol), 10 mL THF, a stir bar, and the quantity of organosulfur substrate indicated below. The bomb was sealed with a Teflon-coated stopcock before it was removed from the dry box, connected to a hydrogen manifold, and charged with H<sub>2</sub> (1 atm). The

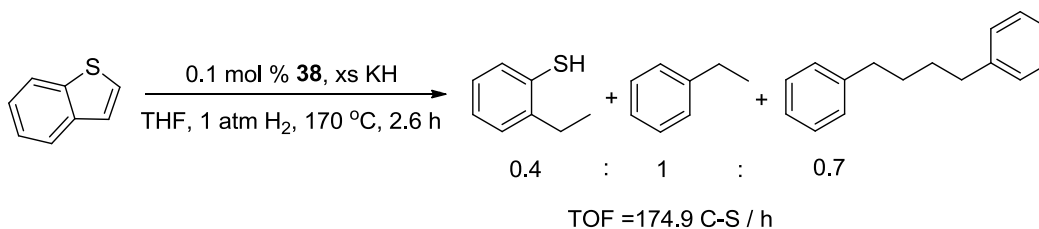
reactor was then placed in a thermostat regulated bath at the temperature indicated, and stirred at 1200 rpm. After the reaction time indicated, the reactor was cooled to room temperature and the reaction mixture was quenched with a 10% HCl solution. A fraction of the organic layer was dried with anhydrous Na<sub>2</sub>SO<sub>4</sub>, pressed through a short Florisil<sup>TM</sup> column, then submitted for GC-MS analysis.

#### 6.4.5.1 4,6-Diethyldibenzothiophene



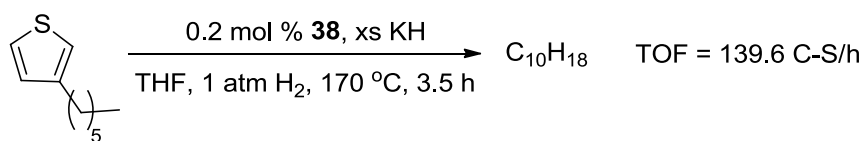
General procedure 6.4.5, using 4,6-diethyldibenzothiophene (151.4 mg, 0.63 mmol), a temperature of 120 °C, and a reaction time of 2.0 h. The process as described afforded conversion of 4,6-diethyldibenzothiophene<sup>127</sup> to 8.3% 3,3'-diethylbiphenyl<sup>128</sup> and 35.24% 2-thiol-3,3'-diethylbiphenyl<sup>129</sup> as determined by GC-MS analysis.

#### 6.4.5.2 Benzothiophene



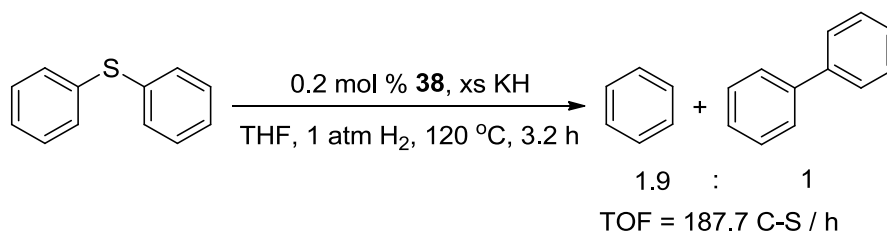
General procedure 6.4.5, using benzothiophene (99 mg, 0.74 mmol), a reaction temperature of 170 °C, and reaction time of 2.6 h. The process as described afforded conversion of benzothiophene<sup>130</sup> to 18.4% ethyl benzene<sup>131</sup>, 7.7% 2-ethylbenzenethiol<sup>132</sup>, and 12.8% 1,4-diphenyl butane<sup>133</sup>, as determined by GC-MS analysis.

#### 6.4.5.2 3-Hexylthiophene



General procedure 6.4.5, using 3-hexylthiophene (85 mg, 0.51 mmol) a reaction temperature of 170 °C, and reaction time of 3.5 h. The process as described afforded 53.7% conversion of 3-hexylthiophene<sup>134</sup> to a C<sub>10</sub>H<sub>18</sub> hydrocarbon as determined by GC-MS analysis.

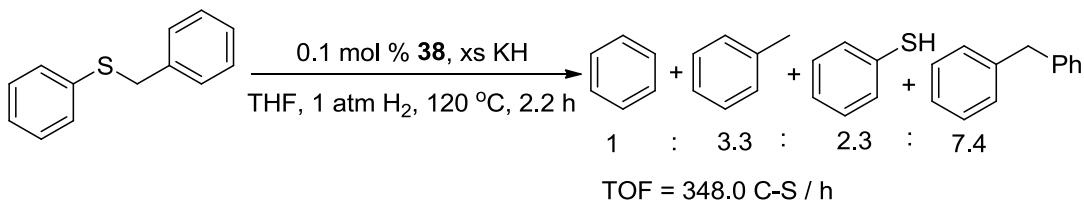
#### 6.4.5.3 Diphenyl sulfide



General procedure 6.4.5, using diphenyl sulfide (120 mg, 0.64 mmol), a reaction temperature of 120 °C, and reaction time of 3.2 h. The process as described

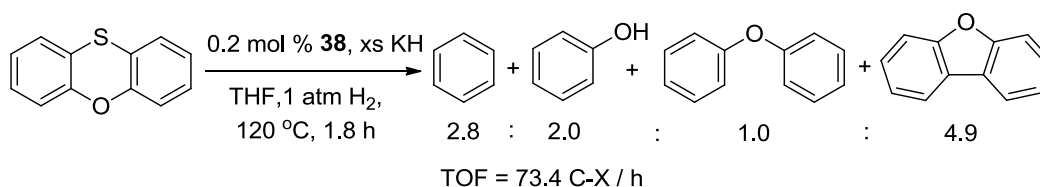
afforded conversion of diphenyl sulfide<sup>132</sup> to 52.5% benzene<sup>135</sup> and 26.3% biphenyl<sup>126</sup>, as determined by GC-MS analysis.

#### 6.4.5.4 Benzyl phenyl sulfide



General procedure 6.4.5, using benzyl phenyl sulfide (120 mg, 0.64 mmol), a reaction temperature of 120 °C, and reaction time of 2.2 h. The process as described afforded conversions of benzyl phenyl sulfide<sup>129</sup> to 5.4% benzene,<sup>135</sup> 17.9% toluene,<sup>135</sup> 12.5% phenyl thiol,<sup>129</sup> and 39.7% diphenylmethane,<sup>133</sup> as determined by GC-MS analysis.

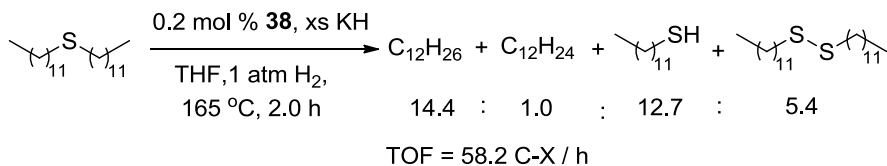
#### 6.4.5.5 Phenoxathiin



General procedure 6.4.5, using phenoxathiin (108 mg, 0.54 mmol), a reaction temperature of 120 °C, and reaction time of 1.8 h. The process as described afforded conversions of phenoxathiin<sup>136</sup> to 9.1% benzene,<sup>135</sup> 6.5% phenol,<sup>137</sup>

3.23% diphenyl ether,<sup>138</sup> and 16.1% dibenzofuran,<sup>124</sup> as determined by GC-MS analysis.

#### 6.4.5.6 *n*-dodecyl sulfide



General procedure 6.4.5, using *n*-dodecylsulfide (192 mg, 0.52 mmol), a reaction temperature of 165 °C, and reaction time of 2.0 h. The process as described afforded conversions *n*-dodecylsulfide to 35.0% dodecane, 2.4% dodecene, 31.0% dodecanethiol, and 13.2% dodecanedisulfide, as determined by GC-MS analysis.

#### 6.4.6 *Substrate scope for catalytic C–O bond hydrogenolysis with [CoMe(NPEt<sub>3</sub>)<sub>4</sub>]PF<sub>6</sub>*

General procedure 6.4.6 was used to investigate the substrate scope for C–O bond hydrogenolysis by precatalyst **38**. Reactions run in the presence of stoichiometric quantities of AlMe<sub>3</sub> followed procedure 6.4.6 with the exception that the noted quantity of AlMe<sub>3</sub> was added to the reactor prior to sealing with a Teflon high vacuum stopcock. Specifics for each substrate are listed under their appropriate headings.

Procedure 6.4.6: Inside a nitrogen-filled dry box, a medium-walled glass bomb was charged with **38** (1 mg, 1.11 x 10<sup>-3</sup> mmol), KH (~117 mg, 2.92 mmol), 10 mL toluene, a stir bar, and the quantity of substrate indicated. The bomb was sealed

with a Teflon vacuum stopcock before it was removed from the dry box, connected to a hydrogen manifold, and charged with H<sub>2</sub> (1 atm). The reactor was then placed in a thermostat-regulated bath at the temperature indicated and stirred at 1200 rpm. After the reaction time indicated, the reactor was cooled to room temperature and the reaction mixture was quenched with a 10% HCl solution. A fraction of the organic layer was dried with anhydrous Na<sub>2</sub>SO<sub>4</sub>, pressed through a short Florisil<sup>TM</sup> column, then submitted for GC-MS analysis.

#### 6.4.6.1 Diphenyl ether

Experiments with diphenyl ether were conducted in the absence and presence of AlMe<sub>3</sub> following procedure 6.4.6 (labeled **A** and **B**, respectively). **A**: Diphenyl ether (85.0 mg, 0.50 mmol) and the other reagents were added to the reactor. The reaction temperature was 150 °C and the reaction time was 1.3 h. The process as described afforded conversion of diphenyl ether<sup>138</sup> to 48.2% benzene<sup>135</sup> and 47.0% phenol<sup>137</sup> as determined by GC-MS analysis. **B**: Diphenyl ether (85.1 mg, 0.50 mmol), AlMe<sub>3</sub> (35.6 mg, 0.49 mmol) and the other reagents were added to the reactor. The reaction temperature was 150 °C and the reaction time was 19.0 h. The process as described afforded quantitative conversion of diphenyl ether<sup>138</sup> to benzene<sup>135</sup> as determined by GC-MS analysis.

#### 6.4.6.2 4-Methoxybiphenyl

Experiments with 4-methoxybiphenyl were conducted in the absence and presence of  $\text{AlMe}_3$  following procedure 6.4.6 (labeled **A** and **B**, respectively). **A**: 4-methoxybiphenyl (93.3 mg, 0.51 mmol) and the other reagents were added to the reactor. The reaction temperature was 150 °C and the reaction time was 1.9 h. The process as described afforded conversion of 4-methoxybiphenyl<sup>139</sup> to 14.9% biphenyl<sup>126</sup> and 85.1% 4-hydroxybiphenyl<sup>139</sup> as determined by GC-MS analysis. **B**: 4-methoxybiphenyl (91.6 mg, 0.50 mmol),  $\text{AlMe}_3$  (36.0 mg, 0.50 mmol) and the other reagents were added to the reactor. The reaction temperature was 150 °C and the reaction time was 19.0 h. The process as described afforded quantitative conversion of 4-methoxybiphenyl<sup>139</sup> to biphenyl<sup>126</sup> as determined by GC-MS analysis.

#### 6.4.6.3 2,3-Dihydrobenzofuran

Experiments with 2,3-dihydrobenzofuran were conducted following procedure 6.4.6 at both short and long reaction times (experiments **A** and **B**, respectively). **A**: 2,3-dihydrobenzofuran (63.8 mg, 0.53 mmol) and the other reagents were added to the reactor. The reaction temperature was 150 °C and the reaction time was 1.0 h. The process as described afforded conversion of 2,3-dihydrobenzofuran<sup>140</sup> to 3.9% 2-ethylphenol<sup>128</sup> as determined by GC-MS analysis. **B**: 2,3-dihydrobenzofuran (56.2 mg, 0.47 mmol), and the other reagents were

added to the reactor. The reaction temperature was 150 °C and the reaction time was 14 h. The process as described afforded conversion of 2,3-dihydrobenzofuran<sup>140</sup> to 54.2% 2-ethylphenol<sup>128</sup> and 46.6% ethyl benzene<sup>131</sup>, as determined by GC-MS analysis.

#### 6.4.6.4 *1,3-Bis(4-methoxyphenoxy)benzene*

Experiments with 1,3-bis(4-methoxyphenoxy)benzene were conducted following general procedure 6.4.6. 1,3-bis(4-methoxyphenoxy)benzene (161.5 mg, 0.50 mmol) and the other reagents were added to the reactor. The reaction temperature was 150 °C and the reaction time was 3.3 h. The process as described afforded conversion of 1,3-Bis(4-methoxyphenoxy)benzene<sup>141</sup> to 3.5% benzene,<sup>135</sup> 22.1% 4-methoxyphenol,<sup>128</sup> and 18.1% 2-ethylphenol,<sup>128</sup> as determined by GC-MS analysis.

#### 6.4.6.5 *Dibenzofuran*

Experiments using dibenzofuran were conducted in the absence and presence of AlMe<sub>3</sub> following general procedure 6.4.6 (**A** and **B**, respectively). **A**: dibenzofuran (106.8 mg, 0.63 mmol) and the other reagents were added to the reactor. The reaction temperature was 150 °C and the reaction time was 2.7 h. The process as described afforded conversion of dibenzofuran<sup>124</sup> to 80.8% 2-hydroxybiphenyl<sup>142</sup> as determined by GC-MS analysis. **B**: Dibenzothiophene

(106.1 mg, 0.63 mmol),  $\text{AlMe}_3$  (45.1 mg, 0.63 mmol) and the other reagents were added to the reactor. The reaction temperature was 150 °C and the reaction time was 2.7 h. The process as described afforded conversion of dibenzofuran<sup>124</sup> to 35.7% 2-hydroxybiphenyl<sup>142</sup> and 60.9% biphenyl<sup>126</sup> as determined by GC-MS analysis.

#### 6.4.6.6 *Benzofuran*

Experiments with benzofuran were conducted in the absence and presence of  $\text{AlMe}_3$  following general procedure 6.4.6 (**A** and **B**, respectively). **A**: benzofuran (63.1 mg, 0.53 mmol) and the other reagents were added to the reactor. The reaction temperature was 150 °C and the reaction time was 3.0 h. The process as described resulted in no hydrogenolysis reactivity; benzofuran<sup>143</sup> was the only species detected by GC-MS analysis. **B**: Benzofuran (56.6 mg, 0.50 mmol),  $\text{AlMe}_3$  (36.1 mg, 0.50 mmol) and the other reagents were added to the reactor. The reaction temperature was 150 °C and the reaction time was 2.7 h. The process as described results in no hydrogenolysis reactivity; benzofuran<sup>143</sup> was the only species detected by GC-MS analysis.

#### 6.4.6.7 *N-methylcarbazole*

The experiment with N-methylcarbazole was conducted following general procedure 6.4.6. N-methylcarbazole (141.6 mg, 0.78 mmol) and the other reagents

were added to the reactor. The reaction temperature was 165 °C and the reaction time was 14 h. The process as described afforded conversion of N-methylcarbazole<sup>144</sup> to 26.1% N-methyl-2-biphenylamine<sup>145</sup> and 7.36% carbazole<sup>144</sup> as determined by GC-MS analysis.

## Bibliography:

- (1) Gladysz, J. A.; Ball, Z. T.; Bertrand, G.; Blum, S. A.; Dong, V. M.; Dorta, R.; Hahn, F. E.; Humphrey, M. G.; Jones, W. D.; Klosin, J.; Manners, I.; Marks, T. J.; Mayer, J. M.; Rieger, B.; Ritter, J. C.; Sattelberger, A. P.; Schomaker, J. M.; Yam, V.W. *Organometallics* **2012**, 1–18.
- (2) Dehnicke, K.; Krieger, M.; Massa, W. *Coord. Chem. Rev.* **1999**, 182, 19–65.
- (3) Sundermann, A.; Schoeller, W. W. *J. Am. Chem. Soc.* **2000**, 122, 4729–4734.
- (4) Hartwig, J. F. *Organotransition Metal Chemistry: From Bonding to Catalysis*; University Science Books: Sausalito, CA, 2010; pp. 15–17.
- (5) Stephan, D. W.; Stewart, J. C.; Courtenay, S.; Kickham, J.; Hollink, E.; Beddie, C.; Hoskin, A.; Graham, T.; Wei, P.; Spence, R. E.; Xu, W.; Koch, L.; Gao, X.; Harrison, D. G. *Organometallics* **2003**, 22, 1937–1947.
- (6) Tolman, C. A. *J. Am. Chem. Soc.* **1970**, 92, 2956–2965.
- (7) Gauthier, J. Titanacyclobutene and Cobalt(II) phoshinimide Complexes. Ph.D. Thesis, University of Alberta, 2012, pp. 73–74, 179–236.
- (8) Birkofer, L.; Sung, M. K. *Chem. Ber.* **1964**, 97, 2100–2101.
- (9) *Trimethylsilylazide*; MSDS No. 92753; Sigma Aldrich: St. Louis, MO, June 2012.
- (10) Dehnicke, K.; Grob, T.; Harms, K. *Z. Anorg. Chemie.* **2000**, 625, 1065–1072.
- (11) Hamilton, R.; Hebert, D.; Reaugh, D.; Zhao, T.; Yu, S.; Stryker, J. M. Unpublished work, University of Alberta, **2012**.
- (12) Dehnicke, K.; Weller, F. *Coord. Chem. Rev.* **1997**, 158, 103–169.
- (13) Honeyman, C. H.; Lough, A. J.; Manners, I. *Inorganic Chemistry* **1994**, 33, 2988–2993.
- (14) Lepichon, L.; Stephan, D. W.; Gao, X.; Wang, Q. *Organometallics* **2002**, 21, 1362–1366.

- (15) Krieger, M.; Gould, R. O.; Dehnicke, K. *Z. Anorg. Allg. Chem.* **1998**, *624*, 781–786.
- (16) Riese, U. Phosphaniminato-Komplexe Elektronenreicher Übergangsmetalle Ph.D. Thesis, Philipps-Universität Marburg, Dec. 1998.
- (17) Mai, H.; Kocker, R. M.; Wocadlo, S.; Massa, W.; Dehnicke, K. *Angew. Chem., Int. Ed.* **1995**, *34*, 1235–1236.
- (18) Riese, U.; Harms K.; Pebler, J.; Dehnicke, K. *Z. Anorg. Allg. Chem.* **1999**, *625*, 746–754.
- (19) Bunquin, J.; Hebert, D.; Stryker, J. M. Unpublished work, University of Alberta, **2012**.
- (20) Li, L.; Zhou, W.; Zhang, G.; Pang, Z. *J. Organomet. Chem.* **2010**, *695*, 588–594.
- (21) Murray, B. D.; Power, P. P. *Inorganic Chemistry.* **1984**, *23*, 4584–4588.
- (22) Camacho-Bunquin, J.; Hebert, D.; Brown, H.; Hamilton, R. J.; Stryker, J. M. Unpublished work, University of Alberta, 2012.
- (23) Hebert, D. Bis(phosphoranimido) Clusters of Iron and Cobalt. Ph.D. Thesis, University of Alberta, 2013.
- (24) Lichtenberger, L.; Renshaw, S. K.; Bullock, M. *J. Am. Chem. Soc.* **1993**, *113*, 3276–3285.
- (25) McGrady, J. E.; Lovell, T.; Stranger, R.; Humphrey, M. G. *Organometallics* **1997**, *16*, 4004–4011.
- (26) Danopoulos, A. A.; Braunstein, P.; Wesolek, M.; Monakhov, K. Y.; Rabu, P.; Robert, V. *Organometallics* **2012**, *31*, 4102–4105.
- (27) Siegbahn, P. E. *J. Phys. Chem.* **1995**, *99*, 12723–12729.
- (28) Bradley, D. C.; Harding, I. S. *Eur. J. Solid. State Inorg. Chem.* **1993**, *30*, 659–671.
- (29) Harms, K.; Merle, J.; Massa, W.; Krieger, M. *Inorganic chemistry* **1998**, *37*, 1099–1104.
- (30) Appleton, T. G.; Clark, H. C.; Manzer, L. E. *Coord. Chem. Rev.* **1973**, *10*, 335–422.

- (31) Hay-Motherwell, R. S.; Hursthouse, B.; Wilkinson, G.; Hussain, B. *Polyhedron* **1990**, *9*, 931–937.
- (32) Riese, U.; Harms, K.; Neumu, B.; Dehnicke, K.; *Z. Anorg. Chemie.* **1998**, *624*, 5–10.
- (33) Evans, D. F. *J. Chem. Soc.* **1959**, 2003–2005.
- (34) Saouma, C.T.; Peters, J.C. *Coord. Chem. Rev.* **2011**, *255*, 920–937.
- (35) Jenkins, D. M.; Peters, J. C. *J. Am. Chem. Soc.* **2003**, *125*, 11162–3.
- (36) Pujari, B.; Stoyanov, S.; Kovalenko, A. National Institute for Nanotechnology.
- (37) Bunting, P.; Long, J. University of California Berkeley.
- (38) Zanello, P. *Inorganic Electrochemistry: Theory, Practice and Application*; Royal Society of Chemistry: Cambridge, 2003; pp. 57–66, 164.
- (39) Cotton, F. A.; Dikarev, E. V.; Petrukhina, M. A. *J. Am. Chem. Soc.* **1997**, *119*, 12541–12549.
- (40) Lucas, C. R.; Liang, W.; Miller, D. O.; Bridson, J. N. *Inorganic Chemistry* **1997**, *36*, 4508–4513.
- (41) Likar, M. D.; Pladziewicz, J. R. *J. Am. Chem. Soc.* **1984**, *106*, 2565–2569.
- (42) Kochi, J. K. *Organometallic Mechanisms and Catalysis*; Academic Press Inc.: New York, 1978; pp. 12.
- (43) Brunshwig, B. S.; Creutz, C.; Sutin, N. *Chem. Soc. Rev.* **2002**, *31*, 168–184.
- (44) Day, P.; Hush, N. S.; Clark, R. J. *Phil. Trans. A: Math. Phys. Eng. Sci.* **2008**, *366*, 5–14.
- (45) Crabtree, R. H. *The Organometallic Chemistry of the Transition Metals*, 5<sup>th</sup> Ed.; John Wiley and Sons: Hoboken, NJ, 2005; p. 381.
- (46) Pauling, L. *Proc. Natl. Acad. Sci.* **1976**, *73*, 4290–4293.
- (47) Dias, A. R.; Diogo, H. P.; Griller, M. E.; Piedada, M. E.; Martinho-Simoes, J. A. *Metal–Carbon and Metal–Hydrogen Bond Dissociation Enthalpies from Classical and Nonclassical Calorimetric Studies*. In *Bonding*

*Energetics in Organometallic Compounds*; Marks, T. J.; ACS Symposium Series, 1990; pp. 205–217.

- (48) Weller, A. S.; McIndoe, J. S. *Eur. J. Inorg. Chem* **2007**, 4411–4423.
- (49) Perutz, R. N.; Sabo-Etienne, S. *Angew. Chem., Int. Ed. Engl.* **2007**, *46*, 2578–2592.
- (50) Lin, Z. *Coord. Chem. Rev.* **2007**, *251*, 2280–2291.
- (51) Quisenberry, K. T.; Hanusa, T. P. *Cobalt: Organometallic Chemistry*. In *Encyclopedia of Inorganic and Bioinorganic Chemistry*; John Wiley & Sons, Hoboken, NJ, 2011; pp. 1–37.
- (52) Bower, B. K.; Tennent, H. G. *J. Am. Chem. Soc.* **1972**, *94*, 2512–2514.
- (53) Byrne, E. K.; Theopold, K. H. *J. Am. Chem. Soc.* **1989**, 3887–3896.
- (54) Campos, J.; Kundu, S.; Pahls, D. R.; Brookhart, M.; Carmona, E.; Cundari, T. R. *J. Am. Chem. Soc.* **2013**, *135*, 1217–20.
- (55) Trinquier, G.; Hoffmann, R. *Organometallics* **1984**, 370–380.
- (56) Gray, T. G.; Veige, A. S.; Nocera, D. G. *J. Am. Chem. Soc.* **2004**, *126*, 9760–8.
- (57) Sanchez-Delgado, R. A. In *Organometallic Modelling of the Hydrodesulfurization and Hydrodenitrogenation Reactions*; Kluwer Academic Publisher: Dordrecht, NL, 2006; pp. 1–24, 36, 95–129.
- (58) Gray, M.; Masliyah, J. H. *Extraction and Upgrading of Oilsands Bitumen: An Intensive Short Course*; Department of Chemical and Materials Engineering, University of Alberta: Edmonton, AB, 2008; pp. A6–A7.
- (59) Shafi, R.; Hutchings, G. J. *Catal. Today* **2000**, *59*, 423–442.
- (60) Wivel, C.; Candia, R.; Clausen, B.; Steen, M.; Topsoe, H. *J. Catal.* **1981**, *68*, 453–463.
- (61) Topsoe, H.; Clausen, B.; Candia, R.; Wivel, C.; Morup, S. *J. Catal.* **1981**, *68*, 433–452.
- (62) Angelici, R. J. *Coord. Chem. Rev.* **1990**, *105*, 61–76.

- (63) Rincon, L.; Terra, J.; Guenzburger, D.; Sanchez-Delgado, R. A. *Organometallics* **1995**, *14*, 1292–1296.
- (64) Spera, M. L.; Harman, W. D. *J. Am. Chem. Soc.* **1997**, *119*, 8843–8851.
- (65) Bianchini, C.; Meli, J. A.; Peruzzini, M.; Vizza, F.; Moneti, S.; Herrera, V.; Sanchez-Delgado, R. A. *J. Am. Chem. Soc.* **1994**, *116*, 4730–4381.
- (66) Ateşin, T. A.; Jones, W. D. *Organometallics* **2008**, *27*, 3666–3670.
- (67) Dullaghan, C. A.; Zhang, X.; Greene, D. L.; Carpenter, G. B.; Sweigart, D. A.; Camiletti, C.; Rajaseelan, E. *Organometallics* **1998**, *17*, 3316–3322.
- (68) Jones, W. D.; Dong, L. *J. Am. Chem. Soc.* **1991**, *113*, 559–564.
- (69) Jones, W. D.; Chin, R. M. *Organometallics* **1992**, *11*, 2698–2700.
- (70) Matsubara, K.; Okamura, R.; Tanaka, M.; Suzuki, H. *J. Am. Chem. Soc.* **1998**, *120*, 1108–1109.
- (71) Vicic, D. A.; Jones, W. D. *J. Am. Chem. Soc.* **1997**, *119*, 10855–10856.
- (72) Torres-Nieto, J.; Arevalo, A.; Garcia-Gutierrez, P.; Acosta-Ramirez, A.; Garcia, J. J. *Organometallics* **2004**, *23*, 4534–4536.
- (73) Bianchini, C.; Meli, A.; Moneti, S.; Vizza, F. *Organometallics* **1998**, *17*, 2636–2645.
- (74) Bianchini, C.; Jimenez, J. M.; Meli, A.; Moneti, S.; Vizza, F.; Herrera, V.; Sanchez-Delgado, R. A. *Organometallics* **1995**, 2342–2352.
- (75) Riaz, U.; Cumow, O. J.; Curtis, M. D. *J. Am. Chem. Soc.* **1994**, *116*, 4357–4363.
- (76) Topsoe, H.; Causen, B. S. *Catal. Rev. Sci. Eng.* **1984**, *26*, 395–419.
- (77) Bai, J.; Li, X.; Wang, A.; Prins, R.; Wang, Y. *J. Catal.* **2013**, *300*, 197–200.
- (78) Simanzhenkov, V.; Idem, R. *Crude Oil Chemistry*; Marcel Dekker, Inc: New York, 2005; pp. 14–20.
- (79) Whitesides, G. M.; Hackett, M.; Brainard, R. L.; Lavalleye, J. P.; Sowinski, A. F.; Izumi, A. N.; Moore, S. S.; Brown, D. W.; Staudt, E. M. *Organometallics* **1985**, *4*, 1819–1830.

- (80) Widegren, J. A.; Finke, R. G. *J. Mol. Catal. A: Chemical* **2003**, *198*, 317–341.
- (81) Vicic, D. A.; Jones, W. D. *J. Am. Chem. Soc.* **1999**, *121*, 7606–7617.
- (82) McCollum, D. G.; Bosnich, B. *Inorg. Chim. Acta* **1998**, *270*, 13–19.
- (83) Vicic, D. A.; Jones, W. D. *J. Am. Chem. Soc.* **1999**, *121*, 4070–4071.
- (84) Bianchini, C.; Casares, J. A.; Meli, A.; Sernau, V.; Vizza, F.; Sánchez-Delgado, R. A. *Polyhedron* **1997**, *16*, 3099–3114.
- (85) Brown, C. A. *J. Chem. Soc., Chem. Commun.* **1974**, 680–682.
- (86) Brown, C. A. *J. Org. Chem.* **1974**, *39*, 3913–3918.
- (87) Leroy, W. D.; Gunn, L. G. *J. Chem. Phys.* **1958**, *80*, 4782–4786.
- (88) Wiedemann, S. H.; Ramı, A.; Collum, D. B. *J. Am. Chem. Soc.* **2003**, *125*, 15893–15901.
- (89) Lucht, B. L.; Collum, D. B. *J. Am. Chem. Soc.* **1994**, *116*, 7949–7950.
- (90) Walther, D. S. Solvent Effects on Alkali Metal Amide Aggregates. Ph.D. Thesis, Brown University, Dec. 1998, pp. 21–50.
- (91) Vecchi, P. A.; Ellern, A.; Angelici, R. J. *J. Am. Chem. Soc.* **2006**, *125*, 2064–2065.
- (92) Bianchini, C.; Herrera, J. V.; Jimenez, M. V.; Meli, A.; Sanchez-Delgado, R. A.; Vimala, F. *J. Am. Chem. Soc.* **1995**, *117*, 8567–8575.
- (93) Sun, S.; Sweigart, D. A.; Dullaghan, C. A. *J. Chem. Soc., Dalton Trans.* **1996**, 4493–4495.
- (94) Palmer, M. S.; Rowe, S.; Harris, S. *Organometallics* **1998**, *17*, 3798–3808.
- (95) Curtis, M. D.; Druker, S. H. *J. Am. Chem. Soc.* **1997**, *119*, 1027–1036.
- (96) He, Z.; Wang, X. *Catal. Sustainable Energy* **2013**, 28–52.
- (97) Cunningham, J. *Innovation Roadmap on Bio-based Feedstocks, Fuels and Industrial Products*; Technical Report for Industry Canada: Ottawa, ON, September 2012; pp. 10–15.

- (98) Background Biorefinery Policy & Legislation 2009 Home Page.  
<http://www.biorefinery.nl/background-biorefinery/policy-legislation/>  
(accessed July 20, 2013).
- (99) Perlack, R. D.; Wright, L. L.; Turhollow, A. F.; Graham, R. L.; Stokes, B. J.; Erbach, D. C. *Biomass as Feedstock for a Bioenergy and Bioproducts Industry: the Technical Feasibility of a Billion-Ton Annual Supply*; U.S. Department of Energy: Washington, DC, 2005; pp. 4–21.
- (100) Lange, H.; Decina, S.; Crestini, C. *Eur. Polym. J.* **2013**, *49*, 1151–1173.
- (101) Mabee, W. E.; Saddler, J. N. *Bioresour. Technol.* **2010**, *101*, 4806–13.
- (102) Zakzeski, J.; Bruijninx, P. C.; Jongerius, A. L.; Weckhuysen, B. M. *Chem. Rev.* **2010**, *110*, 3552–99.
- (103) Holladay, J. E.; White, J. F.; Bozell, J. J.; Johnson, D. *Top Value-Added Chemicals from Biomass Volume II — Results of Screening for Potential Candidates from Biorefinery Lignin*; U. S. Department of Energy: Pacific Northwest National laboratory, Richland, WA, 2007; pp. 1–18.
- (104) Chakar, F. S.; Ragauskas, A. J. *Ind. Crops. Prod.* **2004**, *20*, 131.
- (105) Ritter, S. K. *Chem. Eng. News* **2008**, *46*, 415.
- (106) Furimsky, E. *Appl. Catal., A* **2000**, *199*, 147–190.
- (107) Ittel, S. D.; Tolman, C. A.; English, A. D.; Jesson, J. P. *J. Am. Chem. Soc.* **1978**, *100*, 7577–7585.
- (108) Kundu, S.; Choi, J.; Wang, D. Y.; Choliy, Y.; Emge, T. J.; Krogh-Jespersen, K.; Goldman, A. S. *J. Am. Chem. Soc.* **2013**, *135*, 5127–5143.
- (109) Bonanno, J. B.; Henry, T. P.; Neithamer, D. R.; Wolczanski, P. T.; Lobkovsky, E. B. *J. Am. Chem. Soc.* **1996**, *118*, 5132–5133.
- (110) Ueno, S.; Mizushima, E.; Chatani, N.; Kakiuchi, F. *J. Am. Chem. Soc.* **2006**, *128*, 16516–7.
- (111) van der Boom, M. E.; Liou, S.; Ben-David, Y.; Shimon, L. J.; Milstein, D. *J. Am. Chem. Soc.* **1998**, *120*, 6531–6541.
- (112) Atesin, A. C.; Ray, N. A.; Stair, P. C.; Marks, T. J. *J. Am. Chem. Soc.* **2012**, *134*, 14682–5.

- (113) Dzudza, A.; Marks, T. J. *Org. Lett.* **2009**, *11*, 1523–1526.
- (114) Sergeev, A. G.; Hartwig, J.F. *Science* **2011**, *332*, 439–43.
- (115) Covell, D. J.; White, M. C. *Angew. Chem., Int. Ed. Engl.* **2008**, *47*, 6448–51.
- (116) Shen, Q.; Hartwig, J. F. *J. Am. Chem. Soc.* **2007**, *129*, 7734–5.
- (117) Ali, S. A. *Petrol. Sci. Technol.* **2007**, *25*, 841–852.
- (118) Ji, W.; Ding, Z.; Liu, J.; Song, Q.; Xia, X.; Gao, H.; Wang, H.; Gu, W. *Energy Fuels* **2012**, *26*, 6393–6403.
- (119) Ostapowicz, T. G.; Merkens, C.; Hölscher, M.; Klankermayer, J.; Leitner, W. *J. Am. Chem. Soc.* **2013**, *135*, 2104–7.
- (120) Ward, A. J.; Masters, A. F.; Maschmeyer, T. Transition Metal Single Site Catalysts – From Homogeneous to Immobilized Systems. In *Modern Surface Organometallic Chemistry*; Basset, J.; Psaro, R.; Roberto, D.; Wiley-VCH Verlag GmbH & Co. KGaA, Weinheim, 2009; pp. 167–237.
- (121) Thunnemann, A. F.; Dautzenberg, H.; Joanny, J. F.; Lowen, H. *Adv. Polym. Sci.* **2004**, *166*, 113–171.
- (122) Issleib, V. K.; Seidel, W. Z. *Anorg. Allg. Chem.* **1956**, *6*, 201–215.
- (123) Cope, A. C. *J. Am. Chem. Soc.* **1957**, *57*, 2238–2240.
- (124) Zhang, M. J.; Shen, S. D.; Chen, S. Y.; Sun, Y. H. *Chin. J. Chromatogr.* **2000**, *18*, 241–246.
- (125) Klemm, L. H.; Karchesy, J. J. *Heterocyc. Chem.* **1977**, *15*, 281–284.
- (126) Sun, G.; Stremple, P. Retention Index Characterization of Flavor, Fragrance and Many Other Compounds on DB-1 and DB-XLB [Online]; J&W Scientific: Folsom, CA, 2003; pp. 1–8.
- (127) Lu, X.; Wu, J.; Kong, H.; Hua, R.; Tao, W.; Gu, J.; Xu, G. *Chin. J. Chromatogr.* **2004**, *22*, 5–11.
- (128) Gautzsch, R.; Zinn, P. *Chromatographia* **1996**, *43*, 163–176.
- (129) Garbuzov, V. G.; Misharina, T. A.; Aerov, A. F.; Golovnya, R. V. *J. Anal. Chem. USSR* **1985**, *40*, 576–586.

- (130) Oda, J.; Ichikawa, S.; Mori, T. *Bunseki Kagaku* **1996**, *45*, 825–835.
- (131) Vendeuvre, C.; Bertoncini, F.; Thiebaut, D.; Martin, M.; Hennion, M. *J. Sep. Sci.* **2005**, *28*, 1129–1136.
- (132) Rochat, S.; de Saint Laumer, J. Y.; Cahintreau, A. *J. Chromatogr., A* **2007**, *1147*, 85–94.
- (133) Helmig, D.; Bocquet, F.; Pollmann, J.; Revermann, T. *Atmos. Environ.* **2004**, *38*, 557–572.
- (134) Golovnya, V. G.; Garbuzov, R. V.; Aerov, A. *Izv. Akad. Nauk SSSR, Ser. Khim.* **1978**, *11*, 2271–2274.
- (135) Censullo, A. C.; Jones, D. R.; Wills, M. T. *J. Coat. Technol.* **2003**, *75*, 47–53.
- (136) Zenkevich, I. G. *Zh. Ecol. Khim.* **1994**, *3*, 111–119.
- (137) Place, R. B.; Imhof, M.; Teuber, M.; Olivier-Bosset, J. *Mitt. Lebensmittelunters. Hyg.* **2003**, *94*, 192–211.
- (138) Chang, L. P.; Sheng, L. S.; Yang, M. Z.; An, D. K. *Acta Pharm. Sin.* **1989**, *24*, 847–852.
- (139) Dufek, P.; Pacakova, V.; Zivny, K. *J. Chromatogr.* **1981**, *211*, 150–154.
- (140) Wong, K. C.; Tie, D. Y. *J. Essent. Oil. Res.* **1993**, *5*, 371–374.
- (141) Japan AIST/NIMC Database- Spectrum MS-IW-5490 **2000**.
- (142) Tokuda, H.; Saitoh, E.; Kimura, Y.; Takano, S. *J. Chromatogr.* **1988**, *454*, 109–120.
- (143) Zhang, M. J.; Li, S. D.; Chen, B. J. *Chromatographia* **1992**, *33*, 138–146.
- (144) Zhang, M.; Shen, S. D.; Chen, S. Y.; Sun, Y. H. *Chin. J. Chromatogr.* **2000**, *18*, 241–246.
- (145) Okumura, T. *J. Environ. Chem. Japan* **1991**, *1*, 333–358.
- (146) Pecoraro, T. A.; Chianelli, R. R. *J. Catal.* **1981**, *67*, 430–432.
- (147) Bradley, D. *Canada Report on Bioenergy 2010*; Ottawa, 2010; pp. 1–52.

- (148) Xie, X.; Goodell, B.; Zhang, D.; Nagle, D. C.; Qian, Y.; Peterson, M. L.; Jeillison, J. *Bioresour. Technol.* **2009**, *100*, 1797–1801.
- (149) Crestini, C.; D’Auria, M. *Tetrahedron* **1997**, *53*, 7877–7888.
- (150) Parkas, J.; Brunow, G.; Lundquist, K. *Phytochem. Rev.* **2007**, *3*, 29–60.
- (151) Beste, A.; Buchanan, A. C. *J. Org. Chem.* **2009**, *74*, 2837–41.

## Appendix 1 Select X-Ray Crystallography Data

### A1.1 [FeCCPh(NPEt<sub>3</sub>)<sub>4</sub>]<sub>4</sub>

#### STRUCTURE REPORT

**XCL Code:** JMS1007  
2010

**Date:** 24 February

**Compound:** [Fe<sub>4</sub>(NPEt<sub>3</sub>)<sub>4</sub>(C≡CPh)<sub>4</sub>]

**Formula:** C<sub>56</sub>H<sub>80</sub>Fe<sub>4</sub>N<sub>4</sub>P<sub>4</sub>

**Supervisor:** J. M. Stryker

**Crystallographer:**

R. McDonald

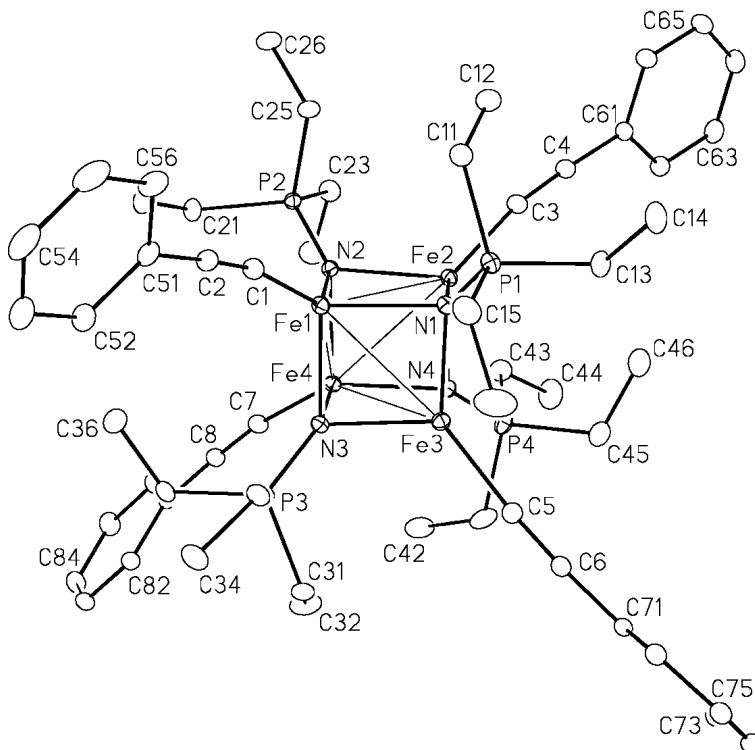


**Figure 1.** Perspective view of the  $[\text{Fe}_4(\text{NPEt}_3)_4(\text{C}\equiv\text{CPh})_4]$  molecule showing the atom labelling scheme. Non-hydrogen atoms are represented by Gaussian ellipsoids at the 20% probability level. Hydrogen atoms are not shown.

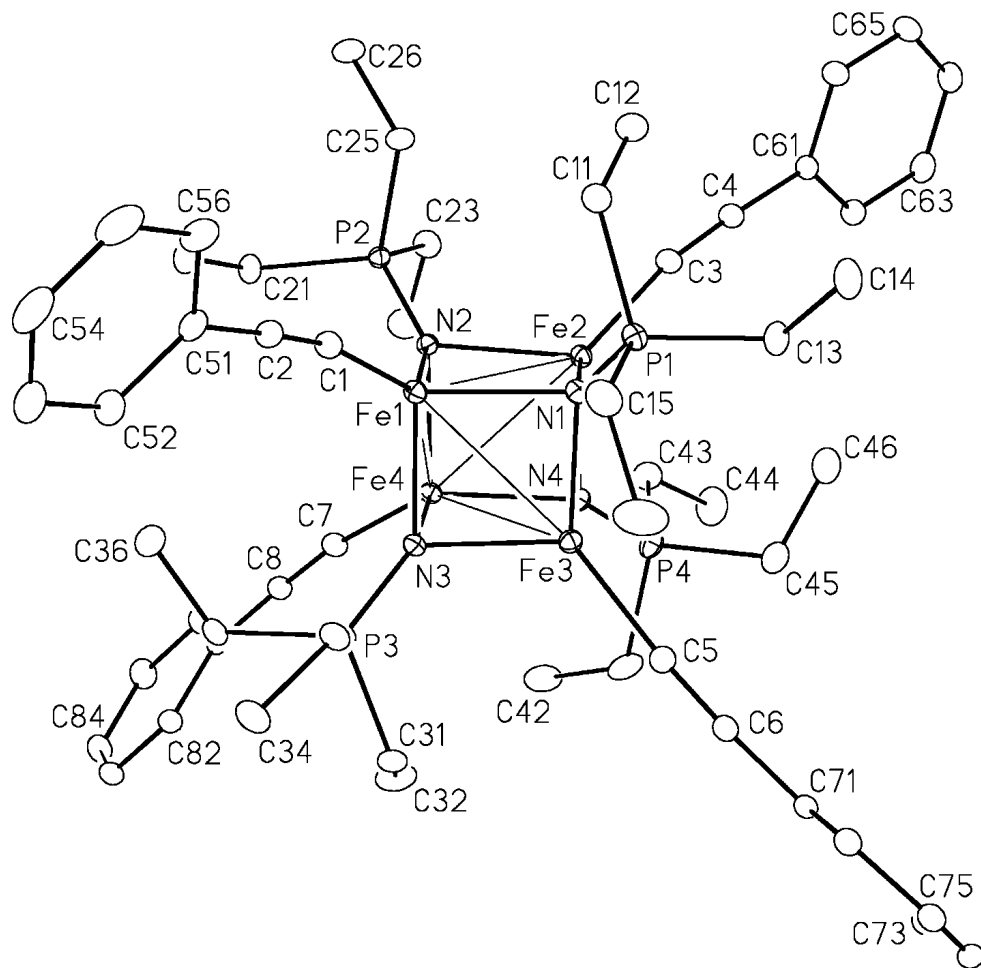


**Figure 2.** Alternate view of the molecule.

**Table 1.** Crystallographic Experimental Details*A. Crystal Data*

formula	$C_{56}H_{80}Fe_4N_4P_4$
formula weight	1156.52
crystal dimensions (mm)	$0.32 \times 0.32 \times 0.17$
crystal system	triclinic
space group	$P \bar{1}$ (No. 2)
unit cell parameters <sup>a</sup>	
<i>a</i> (Å)	10.8125 (3)
<i>b</i> (Å)	14.4086 (4)
<i>c</i> (Å)	19.2354 (6)
$\alpha$ (deg)	85.3928 (4)
$\beta$ (deg)	78.2745 (3)
$\gamma$ (deg)	84.2387 (4)
<i>V</i> (Å <sup>3</sup> )	2913.86 (15)
<i>Z</i>	2
$\rho_{\text{calcd}}$ (g cm <sup>-3</sup> )	1.318
$\mu$ (mm <sup>-1</sup> )	1.124

*B. Data Collection and Refinement Conditions*

diffractometer	Bruker D8/APEX II CCD <sup>b</sup>
radiation ( $\lambda$ [Å]) (0.71073)	graphite-monochromated Mo K $\alpha$
temperature (°C)	-100
scan type	$\omega$ scans (0.3°) (20 s exposures)
data collection $2\theta$ limit (deg)	55.00
total data collected $24 \leq l \leq 24$ )	25881 ( $-14 \leq h \leq 13$ , $-18 \leq k \leq 18$ , -
independent reflections	13260 ( $R_{\text{int}} = 0.0132$ )
number of observed reflections ( <i>NO</i> )	11794 [ $F_o^2 \geq 2\sigma(F_o^2)$ ]
structure solution method ( <i>DIRDIF-2008</i> <sup>c</sup> )	Patterson/structure expansion
refinement method	full-matrix least-squares on $F^2$

(SHELXL-97<sup>d</sup>)

absorption correction method	Gaussian integration (face-indexed)
range of transmission factors	0.8319–0.7129
data/restraints/parameters	13260 / 0 / 613
goodness-of-fit ( <i>S</i> ) <sup>e</sup> [all data]	1.021
final <i>R</i> indices <sup>f</sup>	
<i>R</i> <sub>1</sub> [ $F_o^2 \geq 2\sigma(F_o^2)$ ]	0.0280
<i>wR</i> <sub>2</sub> [all data]	0.0754
largest difference peak and hole	1.206 and –0.740 e Å <sup>-3</sup>

<sup>a</sup>Obtained from least-squares refinement of 9423 reflections with  $4.34^\circ < 2\theta < 53.00^\circ$ .

<sup>b</sup>Programs for diffractometer operation, data collection, data reduction and absorption correction were those supplied by Bruker.

<sup>c</sup>Beurskens, P. T.; Beurskens, G.; de Gelder, R.; Smits, J. M. M; Garcia-Granda, S.; Gould, R. O. (2008). The *DIRDIF-2008* program system. Crystallography Laboratory, Radboud University Nijmegen, The Netherlands.

<sup>d</sup>Sheldrick, G. M. *Acta Crystallogr.* **2008**, *A64*, 112–122.

<sup>e</sup> $S = [\sum w(F_o^2 - F_c^2)^2 / (n - p)]^{1/2}$  (*n* = number of data; *p* = number of parameters varied;  $w = [\sigma^2(F_o^2) + (0.0363P)^2 + 1.7852P]^{-1}$  where  $P = [\text{Max}(F_o^2, 0) + 2F_c^2] / 3$ ).

<sup>f</sup> $R_1 = \sum ||F_o| - |F_c|| / \sum |F_o|$ ;  $wR_2 = [\sum w(F_o^2 - F_c^2)^2 / \sum w(F_o^4)]^{1/2}$ .

## A1.2 [CoMe(NPEt<sub>3</sub>)<sub>4</sub>]<sub>4</sub>

### STRUCTURE REPORT

**XCL Code:** JMS1181  
2011

**Date:** 1 September

**Compound:** [Co<sub>4</sub>Me<sub>4</sub>(NPEt<sub>3</sub>)<sub>4</sub>]•0.5C<sub>4</sub>H<sub>8</sub>O<sub>2</sub>

**Formula:** C<sub>30</sub>H<sub>76</sub>Co<sub>4</sub>N<sub>4</sub>OP<sub>4</sub> (C<sub>28</sub>H<sub>72</sub>Co<sub>4</sub>N<sub>4</sub>P<sub>4</sub>•0.5C<sub>4</sub>H<sub>8</sub>O<sub>2</sub>)

**Supervisor:** J. M. Stryker

**Crystallographer:**

M. J. Ferguson

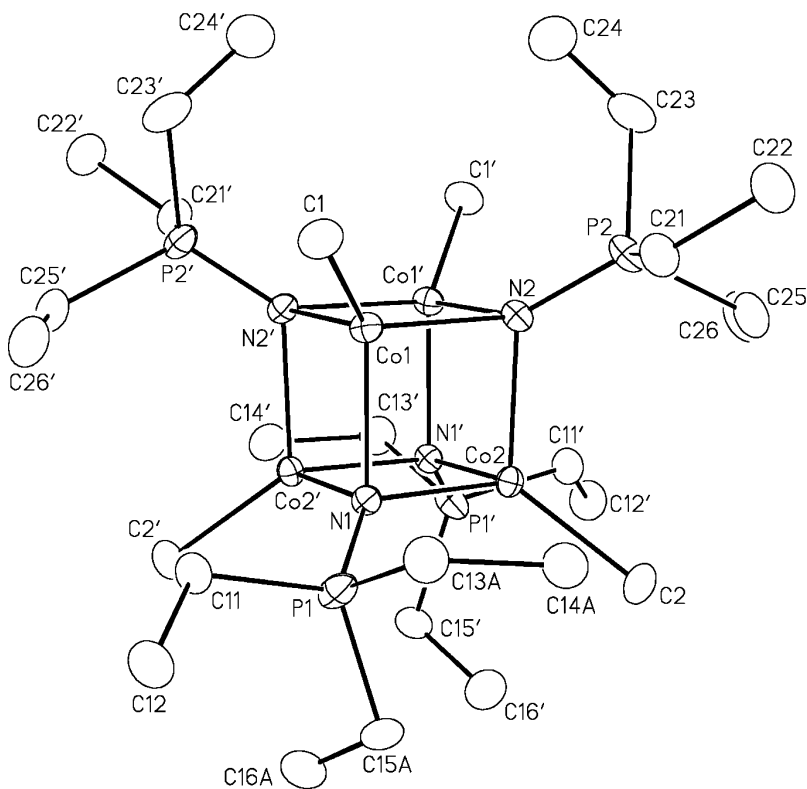




**Table 1.** Crystallographic Experimental Details*A. Crystal Data*

formula	C <sub>30</sub> H <sub>76</sub> Co <sub>4</sub> N <sub>4</sub> OP <sub>4</sub>
formula weight	868.55
crystal dimensions (mm)	0.43 × 0.37 × 0.33
crystal system	monoclinic
space group	C2/c (No. 15)
unit cell parameters <sup>a</sup>	
<i>a</i> (Å)	20.0923 (7)
<i>b</i> (Å)	11.7367 (4)
<i>c</i> (Å)	19.3473 (7)
β (deg)	100.0498 (4)
<i>V</i> (Å <sup>3</sup> )	4492.4 (3)
<i>Z</i>	4
ρ <sub>calcd</sub> (g cm <sup>-3</sup> )	1.284
μ (mm <sup>-1</sup> )	1.619

*B. Data Collection and Refinement Conditions*

diffractometer	Bruker PLATFORM/APEX II CCD <sup>b</sup>
radiation (λ [Å]) (0.71073)	graphite-monochromated Mo Kα
temperature (°C)	-100
scan type	ω scans (0.3°) (20 s exposures)
data collection 2θ limit (deg)	55.00
total data collected 25 ≤ <i>l</i> ≤ 25)	19645 (-25 ≤ <i>h</i> ≤ 26, -15 ≤ <i>k</i> ≤ 15, -
independent reflections	5155 ( <i>R</i> <sub>int</sub> = 0.0114)
number of observed reflections ( <i>NO</i> )	4777 [ <i>F</i> <sub>o</sub> <sup>2</sup> ≥ 2σ( <i>F</i> <sub>o</sub> <sup>2</sup> )]
structure solution method	direct methods ( <i>SHELXS-97</i> <sup>c</sup> )
refinement method ( <i>SHELXL-97</i> <sup>c</sup> )	full-matrix least-squares on <i>F</i> <sup>2</sup>
absorption correction method	Gaussian integration (face-indexed)
range of transmission factors	0.5070–0.4215

data/restraints/parameters	5155 / 9 <sup>d</sup> / 246
goodness-of-fit ( <i>S</i> ) <sup>e</sup> [all data]	1.080
final <i>R</i> indices <sup>f</sup>	
<i>R</i> <sub>1</sub> [ $F_o^2 \geq 2\sigma(F_o^2)$ ]	0.0461
<i>wR</i> <sub>2</sub> [all data]	0.1455
largest difference peak and hole	1.842 and -1.188 e Å <sup>-3</sup>

<sup>a</sup>Obtained from least-squares refinement of 9983 reflections with  $4.74^\circ < 2\theta < 55.00^\circ$ .

<sup>b</sup>Programs for diffractometer operation, data collection, data reduction and absorption correction were those supplied by Bruker.

<sup>c</sup>Sheldrick, G. M. *Acta Crystallogr.* **2008**, A64, 112–122.

<sup>d</sup>The P1–C13A/B and P1–C15A/B distances were restrained to be the same by use of the *SHELXL SADI* instruction. The C13B–C15B distance was restrained to be 1.53(1)Å. The solvent dioxane O1S–C1S and C1S–C2S distances were restrained to be 1.43(2) and 1.50(2) Å, respectively.

<sup>e</sup> $S = [\sum w(F_o^2 - F_c^2)^2 / (n - p)]^{1/2}$  (*n* = number of data; *p* = number of parameters varied;  $w = [\sigma^2(F_o^2) + (0.0821P)^2 + 13.8385P]^{-1}$  where  $P = [\text{Max}(F_o^2, 0) + 2F_c^2]/3$ ).

<sup>f</sup> $R_1 = \sum ||F_o| - |F_c|| / \sum |F_o|$ ;  $wR_2 = [\sum w(F_o^2 - F_c^2)^2 / \sum w(F_o^4)]^{1/2}$ .

**A1.3 [CoMe(NPEt<sub>3</sub>)<sub>4</sub>]PF<sub>6</sub>**

**STRUCTURE REPORT**

**XCL Code:** JMS1205  
2012

**Date:** 17 January

**Compound:** [Co<sub>4</sub>Me<sub>4</sub>(NPEt<sub>3</sub>)<sub>4</sub>][PF<sub>6</sub>]

**Formula:** C<sub>28</sub>H<sub>72</sub>Co<sub>4</sub>F<sub>6</sub>N<sub>4</sub>P<sub>5</sub>

**Supervisor:** J. M. Stryker

**Crystallographer:**

M. J. Ferguson

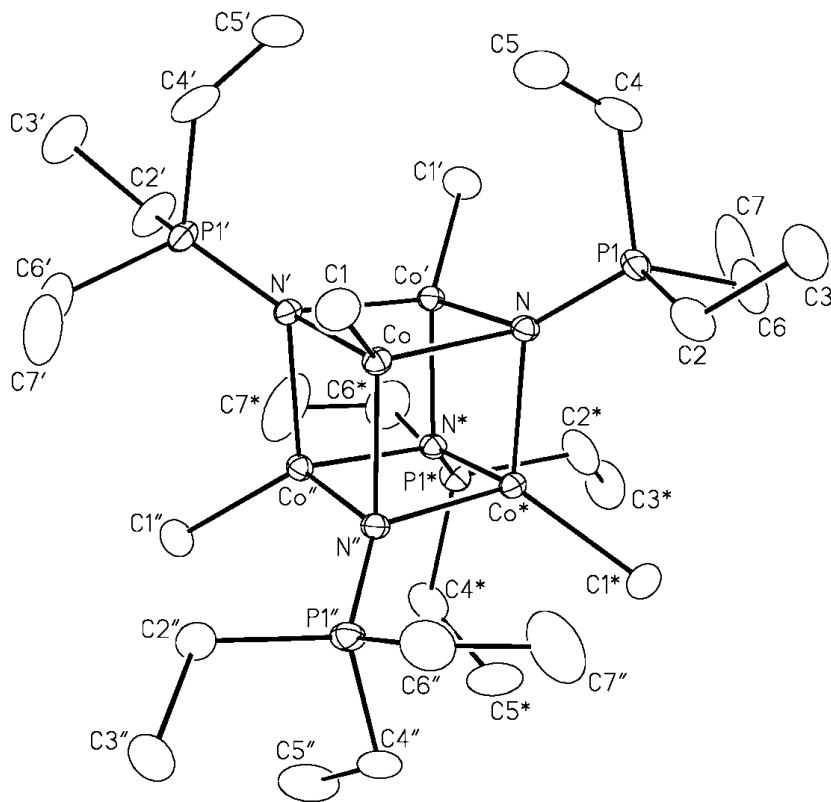


**Figure 1.** Perspective view of the  $[\text{Co}_4\text{Me}_4(\text{NPEt}_3)_4]^+$  ion showing the atom labelling scheme. Non-hydrogen atoms are represented by Gaussian ellipsoids at the 20% probability level. Hydrogen atoms are not shown. Primed (') atoms are related to unprimed ones by eq  $\sqrt[5]{-}$ , eq  $\sqrt[5]{-}$ , z; double-primed (") atoms by y, eq  $\sqrt[5]{-}$ , eq  $\sqrt[5]{-}$ ; Asterisked (\*) atoms by eq  $\sqrt[5]{-}$ , x, eq  $\sqrt[5]{-}$ .

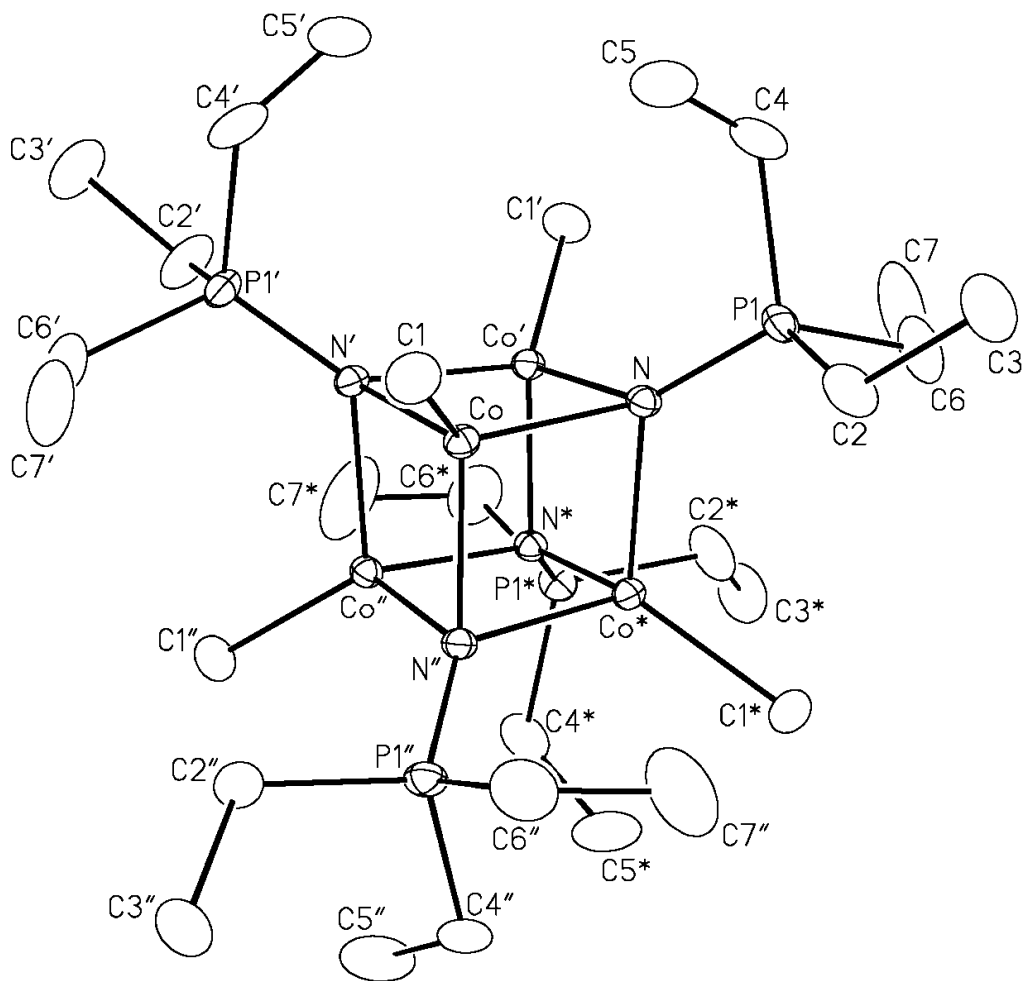


**Table 1.** Crystallographic Experimental Details*A. Crystal Data*

formula	C <sub>28</sub> H <sub>72</sub> Co <sub>4</sub> F <sub>6</sub> N <sub>4</sub> P <sub>5</sub>
formula weight	969.47
crystal dimensions (mm)	0.12 × 0.11 × 0.09
crystal system	tetragonal
space group	$P \overline{4}2_1c$ (No. 114)
unit cell parameters <sup>a</sup>	
<i>a</i> (Å)	11.2452 (3)
<i>c</i> (Å)	17.2258 (4)
<i>V</i> (Å <sup>3</sup> )	2178.28 (10)
<i>Z</i>	2
$\rho_{\text{calcd}}$ (g cm <sup>-3</sup> )	1.478
$\mu$ (mm <sup>-1</sup> )	13.88

*B. Data Collection and Refinement Conditions*

diffractometer	Bruker D8/APEX II CCD <sup>b</sup>
radiation ( $\lambda$ [Å]) (1.54178)	graphite-monochromated Cu K $\alpha$
temperature (°C)	-100
scan type	$\omega$ scans (0.8°) (8 s exposures)
data collection $2\theta$ limit (deg)	135.36
total data collected $20 \leq l \leq 20$ )	13104 ( $-13 \leq h \leq 13, -13 \leq k \leq 13, -$
independent reflections	1944 ( $R_{\text{int}} = 0.0400$ )
number of observed reflections ( <i>NO</i> )	1814 [ $F_o^2 \geq 2\sigma(F_o^2)$ ]
structure solution method	direct methods ( <i>SHELXS-97</i> <sup>c</sup> )
refinement method ( <i>SHELXL-97</i> <sup>c</sup> )	full-matrix least-squares on $F^2$
absorption correction method	Gaussian integration (face-indexed)

range of transmission factors	0.3779–0.2934
data/restraints/parameters	1944 / 0 / 107
Flack absolute structure parameter <sup>d</sup>	0.001(6)
goodness-of-fit ( <i>S</i> ) <sup>e</sup> [all data]	1.065
final <i>R</i> indices <sup>f</sup>	
<i>R</i> <sub>1</sub> [ $F_o^2 \geq 2\sigma(F_o^2)$ ]	0.0368
<i>wR</i> <sub>2</sub> [all data]	0.0999
largest difference peak and hole	0.598 and –0.340 e Å <sup>-3</sup>

<sup>a</sup>Obtained from least-squares refinement of 9110 reflections with  $9.40^\circ < 2\theta < 134.60^\circ$ .

<sup>b</sup>Programs for diffractometer operation, data collection, data reduction and absorption correction were those supplied by Bruker.

<sup>c</sup>Sheldrick, G. M. *Acta Crystallogr.* **2008**, *A64*, 112–122.

<sup>d</sup>Flack, H. D. *Acta Crystallogr.* **1983**, *A39*, 876–881; Flack, H. D.; Bernardinelli, G. *Acta Crystallogr.* **1999**, *A55*, 908–915; Flack, H. D.; Bernardinelli, G. *J. Appl. Cryst.* **2000**, *33*, 1143–1148. The Flack parameter will refine to a value near zero if the structure is in the correct configuration and will refine to a value near one for the inverted configuration.

<sup>e</sup> $S = [\sum w(F_o^2 - F_c^2)^2 / (n - p)]^{1/2}$  ( $n$  = number of data;  $p$  = number of parameters varied;  $w = [\sigma^2(F_o^2) + (0.0663P)^2 + 0.5934P]^{-1}$  where  $P = [\text{Max}(F_o^2, 0) + 2F_c^2]/3$ ).

<sup>f</sup> $R_1 = \sum ||F_o| - |F_c|| / \sum |F_o|$ ;  $wR_2 = [\sum w(F_o^2 - F_c^2)^2 / \sum w(F_o^4)]^{1/2}$ .